Validation of Microwave Imaging Algorithms for Medical Devices

Karadima, Olympia

Awarding institution:
King's College London

Validation of Microwave Imaging Algorithms for Medical Devices

King's College London

Engineering Department

Olympia Karadima

Supervisor: Dr. Panagiotis Kosmas

This dissertation is submitted for the degree of Doctor of Philosophy

Declaration

I hereby declare that except where specific reference is made to the work of others, the contents of this dissertation are original and have not been submitted in whole or in part for consideration for any other degree or qualification in this, or any other university. This dissertation is my own work and contains nothing which is the outcome of work done in collaboration with others, except as specified in the text and Acknowledgements. This dissertation contains fewer than 100,000 words including appendices, bibliography, footnotes, tables and equations and has fewer than 150 figures.

Olympia Karadima

February 1, 2023

Acknowledgements

It takes a village to complete a doctoral dissertation. Coming to the end of this long journey, I would like to take this as an opportunity to express my sincere gratitude to all those who were by my side. My first and greatest thank you must of course go to my supervisor Dr Panos Kosmas for his guidance and thoughtful insights, but also for his encouragement, support, patience and understanding. Thanks must also be given to Dr Maya Thanou for welcoming me to the chemistry lab and providing me with all the support I was needing during my experimental measurements. I would also like to express my sincere gratitude to Dr Raquel Conceição and Dr Francesca Vipiana for the help, encouragement and guidance they offered me during the last 4 years.

I owe a massive thank you to Eleonora, Navid, Pan and Yannis for always being there, in the good and the bad PhD days, helping me in my research, supporting me with their comments and being an excellent companion for a drink after a hard day in the lab. In addition, I would like to thank all the ESR's and supervisors from the EMERALD group. You made this journey unique.

Furthermore, I want to acknowledge my friends from UK and Greece for backing me up in the whole way to the PhD. Georgia, Katerina, Vasilis, Olga thank you for being there from the beginning. Last but not least, I want to express my gratitude to my parents and brother for all of their love, support, and care throughout the years.

Abstract

The use of microwave imaging for medical applications has attracted growing interest in the past decades, inspired by the presence of differences in the dielectric properties of healthy and diseased tissues. The main goal of this research project is focused on incorporating computationally efficient microwave tomography algorithms into medical diagnostic devices.

More specifically, microwave tomography methods for head imaging are challenged by the non-linearity of the problem and the non-uniqueness of the solution. The main objective of this thesis is to tackle these challenges and successfully incorporate a previously developed algorithm combining the distorted Born iterative method with two-step iterative shrinkage thresholding (DBIM-TwIST) into a microwave tomography prototype for the problem of brain stroke detection and differentiation.

To this end, we have constructed simplified and complex multi-layer phantoms that have similar dielectric properties with head tissues by developing tissue-mimicking materials formed by gelatine-oil concentrations. In the first set of experiments, the aim has been to show the potential of two-dimensional (2-D) DBIM-TwIST in determining the type of stroke by estimating its dielectric properties. Our results have demonstrated that the prototype can differentiate between hemorrhagic and ischemic strokes based on the estimation of their dielectric properties. The purpose of the second set of experiments has been to experimentally validate our 2-D and three-dimensional (3-D) DBIM-TwIST algorithms for stroke detection and differentiation using a complex head model, but also to further assess experimentally the performance of the 3-D algorithm for the examined application. For some of the studied scenarios, the 2-D DBIM-TwIST can lead to more accurate reconstructions. However, the 3-D inverse algorithm can provide more accurate results for problems with significant variation along all three dimensions, as can be the case of brain imaging. This has been the first validation study of a MWI algorithm that detects and differentiates two types of strokes, using an anatomically accurate multi-layered head phantom in a wide frequency range.

Contents

List of Abbreviations

EMERALD	ElectroMagnetic imaging for a novel genERation of medicAL Devices
DBIM	Distorted Born Iterative Method
TwIST	Two-step Iterative Shrinkage Thresholding
S-parameters	Scattering Parameters
EM	Electromagnetic
MWI	Microwave Imaging
ESR's	Early-Stage Researchers
CT	Computed Tomography
MRI	Magnetic Resonance Imaging
US	Ultrasound
PET	Positron Emission Tomography
ROI	Region of Interest
2-D	Two-Dimensional
3-D	Three-Dimensional
VNA	Vector Network Analyzer
CSF	Cerebrospinal Fluid

MWT	Microwave Tomography
FDTD	Finite Difference Time Domain
FEM	Finite Element Method
CSI	Contrast Source Inversion
TSVD	Truncated Singular Value Decomposition
FISTA	Fast Iterative Shrinkage/Thresholding Algorithm
SNR	Signal-to-Noise Ratio
SVD	Singular Value Decomposition
PET	Positron Emission Tomography
POLITO	Polytechnic University of Turin
TE	Transverse Electric
GPU	Graphics Processing Unit
ABC	Absorbing Boundary Conditions
PML	Perfectly Matched Layer
CPML	Convolutional Perfectly Matched Layer
CFS	Complex Frequency, Shifted
LIP	Linear Inverse Problem
SOR	Successive Overrelaxation Method
SSOR	Symmetric Successive Overrelaxation Method
KSM	Krylov Subspace Method
GMR	Generalized Minimum Residual
CGLS	Conjugate Gradient method for Least Squares

MINRES	Minimal KSM Residual
IST	Iterative Shrinkage/Thresholding
MWIFH	Microwave Imaging Frequency Hopping
ABS	Acrylonitrile Butadiene Styrene
PDMS	Polydimethylsiloxane
KNNs	K-Nearest Neighbors

List of Figures

List of Tables

Chapter 1

Introduction

1.1 Motivation, Aims, and Objectives

Nowadays, medical imaging technologies play a significant role in tackling the continually growing number of difficulties brought on by ageing populations, since they are essential clinical tools for making an accurate initial diagnosis and monitoring the course of disease over time. In order to supplement and assist existing modalities, a wide range of new imaging techniques are constantly being developed. One of these methods is electromagnetic (EM) imaging, which involves illuminating the area of the body under investigation, with low-power non-ionizing EM waves and using the resulting back-scattered signals to produce images of the interior organs. The research of this PhD involves validating microwave imaging (MWI) algorithms for medical diagnostic devices. Specifically, the research focuses on testing and improving MWI algorithms for detection and monitoring of brain stroke, with numerical simulations, and validating the results with experimental phantoms that simulate the tissues and the dielectric properties of the human head.

The main goal of this research project is focused on incorporating computationally efficient microwave tomography algorithms into medical diagnostic devices. This goal is a critical objective for the European Union project ElectroMagnetic imaging for a novel

genERation of medicAL Devices (EMERALD), which has motivated this research. The algorithms have been primarily based on inverse scattering techniques with the distorted Born iterative method (DBIM). They have been validated and tested first with numerical and experimental prototypes developed by King's College London, and then they have been tailored to specific diagnostic applications developed by other EMERALD groups. The project aimed to achieve the following objectives:

- Incorporate the computationally efficient 2-D and 3-D imaging algorithms into medical diagnostic devices for brain stroke detection and differentiation (Chapter 3 and Chapter 4).
- Refine the imaging algorithm to optimize performance for experimental data (Chapter 3 and Chapter 4).
- Validate the imaging algorithm with the experimental phantoms (Chapter 3 and Chapter 4).
- Incorporate hardware improvements developed within EMERALD (Chapter 3).
- Adapt the in-house MWI algorithm to the hardware systems developed within EMERALD group (Chapter 4).

The major accomplishments expected from this project are first, incorporating state-of-the-art MWT algorithms optimized for specific prototypes and second, the validation of these algorithms with experimental data for specific prototypes and test-beds (phantoms).

1.2 Introduction to Electromagnetic Imaging for a Novel Generation of Medical Devices (EMERALD)

EMERALD is the coherent action of leading European engineering groups involved in EM technology for medical imaging, to create a cohort which aims expediting the transfer of this technology "from research bench to patient bedside."

EMERALD's main objective has been to accelerate the development of clinical prototypes from EM medical imaging research, by offering related PhD's and training to a team of 13 early-stage researchers (ESR's). The EMERALD consortium has been formed by academic institutions, business partners, hospitals, and university medical centers. Secondments in beneficiaries of the EMERALD network have been an important part of the project. Their aim was to enhance the collaboration among the different stakeholders as well as, exchange ideas and improve the knowledge about MWI hardware and software through additional tasks.

Overall, four secondments were scheduled that intended to first define the clinical needs in diagnostic systems and then investigate the optimisation of MWI systems, as well as, assess the performance of robust algorithms in various MWI prototypes. The first secondment took place in Bern's University Hospital in Switzerland from January 2019 to March 2019. The aim of the first secondment was the interaction with medical experts in the diagnosis of cerebrovascular diseases in order to understand the anatomy of the head, brain, and stroke which should then be translated into requirements for the microwave imaging algorithms. Through this secondment it became clear that any MWI prototype, in order to be clinically significant, needs to differentiate the type of the stroke, as soon as possible, even from the ambulance stage. The literature studied through the secondment is presented in Chapter 2. The second secondment took place in Keysight, Austria from November 2019 to December 2019 and is presented in Chapter 3. The third secondment was planned to take place in the University of

Lisbon but due to Covid-19 travel restrictions, it was conducted virtually. As the objectives of the secondment were altered, it is presented in the Appendix C. The last secondment, in the Polytechnic University of Turin (POLITO) was also conducted virtually and is presented in Chapter 4.

1.3 Introduction to Medical Diagnostics

Medical imaging is a principal tool for visualizing the tissues and the structures of the body to detect any abnormality or malignancy [1]. The main imaging techniques which are widely used in acute-care settings include X-rays, computed tomography (CT), magnetic resonance imaging (MRI), ultrasound (US), and positron emission tomography(PET) [2]. Although these methods provide accurate clinical data with a high resolution, they suffer from high operating costs and long examination times. For example, MRI offers the optimal resolution of images, but it is an expensive procedure. X-rays and CT can produce images of high resolution, yet they cannot image soft tissues [3]. Also, they have been accused for side effects like nausea, hair loss, skin and breathing complications on top of increased cancer risk due to the ionizing radiation that is used in this type of imaging [4]. PET scans can produce good images of the soft tissues, but they could lead to the wrong diagnosis of a tumor as sometimes they show areas of high activity like rheumatoid arthritis or tuberculosis. Furthermore, they cannot be used to pregnant women as they require the injection of radioactive tracers [5]. Moreover, the above-mentioned imaging methods and devices are usually not portable, creating delays in the diagnosis window as they require the patient to be admitted to the hospital [2]. Therefore, the use of the above imaging methods is unsuitable for critical conditions when a fast and continuous diagnosis is vital [6]. Furthermore, the increased associated costs can prevent their operation in underserved communities, maintaining and increasing the imbalance of health care access worldwide [7]. These challenges motivate the development of alternative approaches, which aim to be fast, safe, portable, and cost-effective.

1.4 MWI Systems for Medical Diagnostics

Microwave imaging represents an attractive alternative, due to its low-cost, safe (non-ionizing and low-power nature of the employed radiations), non-invasive and portable modalities. Efforts to develop MWI systems for medical diagnostics go back almost fifty years [5],[8],[9],[10],[11]-[26]. Larsen and Jacobi were among the first ones who used microwave radiation to identify different kidney tissues [27],[28]. Consequently, microwaves attracted a lot of attention and since the 1970s, extended research has been conducted on the development of MWI systems for various medical conditions. Initially, research was focused on breast imaging, with Dartmouth College contributing significant work in this area [8],[29]-[31]. Moreover, early detection of breast cancer was studied in [32], [33] and [34], with some advanced set-ups and techniques proposed in [10],[13],[23],[35],[36]. After 50 years of intensive study, the biggest challenge of MWI area is that the technology is a potential imaging modality that is still at the clinical-acceptance stage. However, the situation is quickly shifting, and in June 2019, Micrima Ltd.'s MARIA imaging system was deployed in hospitals in Germany for the purpose of detecting breast tumours [5].

Other implementations of MWI include detection of pulmonary edema, skin cancer, heel bone fracture, cervical myelopathy, leukemia, cerebral edema, lung cancer, heart imaging, joint tissue imaging, thermo-acoustic imaging of subcutaneous vasculature [5]. Within the last years, research has been targeted into diagnosing the brain oedema and monitoring brain stroke as a result of the dielectric contrast between healthy and malignant brain tissues. Specifically for the problem of brain stroke detection and classification, the most advanced systems are the ones proposed by [3], [37], and [38]. Moreover, a recent study by [39] presented images from a novel, portable EM scanner used in patients with either hemorrhagic or ischemic stroke. The presented images are encouraging. However, while such clinical studies are the main target for MWI stroke detection, they cannot be used to fully evaluate the accuracy in estimating the dielectric properties of the stroke and hence the system's ability to differentiate

hemorrhagic from ischemic stroke. From the industrial side, three notable companies have developed imaging prototypes with clinical representation. First, the Strokefinder from Medfield Diagnostics, is an imaging prototype focused on the classification of the type of the stroke. Recently, Strokefinder has placed in the intensive care units of various hospitals in Athens [40]. Secondly, the BrainScanner, from EMTensor and EMVT from EMVision which are in clinical testing, have developed portable devices for continuous brain imaging and stroke detection [41],[42].

Overall, MWI is an auspicious modality that could significantly benefit and improve the field of medical imaging. However, extensive research is required to overcome some important challenges in order to develop effective MWI systems that could be used widely for clinical applications and imaging. Some key challenges are: 1) A robust and adaptive imaging algorithm that will be able to overcome the non-linearity of the inverse problem, as well as, deal with the low dielectric contrast of some tissues 2) Need for efficient and optimised hardware and 3) MWI systems with high dynamic range.

1.5 Contribution and Relevant Publications

The main contribution of the current study is in the area of 2-D and 3-D MWT algorithms. More specifically this thesis focuses on the experimental validation and optimization of MWT algorithms for brain stroke detection and classification, in a wide frequency range. The thesis' key contributions are listed below:

- An extended validation study of the 2-D DBIM-TwIST algorithm for brain stroke detection and classification using simulation, as well as experimental data from a MWT experimental prototype and fabricated gel-based phantoms has hereby been presented (Chapter 3).

  Related papers: O. Karadima, N. Ghavami, I. Sotiriou and P. Kosmas, "Performance assessment of microwave tomography and radar imaging using an anthropomorphic brain phantom," 2020 XXXIIIrd General Assembly and Scientific

Symposium of the International Union of Radio Science, pp. 1-4, 2020.

O. Karadima, M. Rahman, I. Sotiriou, N. Ghavami, P. Lu, S. Ahsan, and P. Kosmas, "Experimental validation of microwave tomography with the dbim-twist algorithm for brain stroke detection and classification," Sensors, vol. 20, no. 3, p. 840, 2020.

- The implementation of the 3-D DBIM-TwIST algorithm has been applied to a 3-D MWI problem. The 3-D algorithm has shown promising results in realistic simulated and experimental scenarios mimicking brain stroke (Chapter 4).

  Related paper: O. Karadima, P. Lu and P. Kosmas, "Comparison of 2-D and 3-D DBIM-TwIST for Brain Stroke Detection and Differentiation," 2021 15th European Conference on Antennas and Propagation (EuCAP), pp. 1-4, 2021.

- Various approximate models as the initial guess have been investigated to assess whether a more accurate forward model could achieve into stronger reconstructed results, using 3-D DBIM-TwIST. (Chapter 4).

  Related paper: O. Karadima, P. Lu, I. Sotiriou and P. Kosmas, "Evaluation of the initial guess for brain stroke detection using microwave tomography," 2021 IEEE International Conference on Antenna Measurements and Applications (CAMA), pp. 1-5, 2021.

- A novel multi-layer anatomically accurate head phantom has been designed and prepared using gelatine-based tissue mimicking materials. The performance of the 2-D and 3-D implementations of the DBIM-TwIST algorithm has been compared in a systematic manner using CST simulated and experimentally measured data. This is the first validation study of a MWI algorithm that detects and differentiates two types of strokes, using an anatomically accurate multi-layered head phantom in a wide frequency range (Chapter 4).

  Related paper: O. Karadima, I. Sotiriou, P. Lu and P. Kosmas, "Validation of the DBIM-TwIST Algorithm for Brain Stroke Detection and Differentiation Us-

ing a Novel Head Phantom," IEEE Open Journal of Antennas and Propagation, vol. 3, pp. 274– 286, 2022.

- The development of a new semi-flexible and rigid composite material as a matching medium for medical microwave diagnostic systems has been presented and discussed (Chapter 3).

  Related paper: A. Moradpour, O. Karadima, I. Alic, M. Ragulskis, F. Kienberger, and P. Kosmas, "Development of a Solid and Flexible Matching Medium for Microwave Medical Diagnostic Systems," Diagnostics, vol. 11, no. 3, p. 550, Mar. 2021.

- The 3-D DBIM-TwIST algorithm has been assessed for an alternative MWI prototype for 3-D brain stroke imaging (Chapter 4).

- A cascade-classifier, in which the location of the stroke is classified ahead of its type, is implemented. The rationale is that the classification of strokes that have been identified in the same location, results in more accurate classification of the type of the stroke (Appendix C).

  Related paper: O. Karadima, R. C. Conceição and P. Kosmas, "Differentiation of brain stroke type by using microwave-based machine learning classification," 2021 International Conference on Electromagnetics in Advanced Applications (ICEAA) (pp. 185-185) 2021.

Additional publications in which the author contributed, are stated as follows:

1. Z. Guo, S. Ahsan, O. Karadima, I. Sotiriou and P. Kosmas, "Resolution Capabilities of the DBIM-TwIST Algorithm in Microwave Imaging," in 13th European Conference on Antennas and Propagation (EuCAP), pp. 1-4, 2019.

2. O. Karadima, E. Razzicchia and P. Kosmas, "Image Improvement Through Metamaterial Technology for Brain Stroke Detection," 2020 14th European Conference on Antennas and Propagation (EuCAP), pp. 1-4, 2020.

3. N. Ghavami, E. Razzicchia, O. Karadima, P. Lu, W. Guo, I. Sotiriou and P. Kosmas, "The Use of Metasurfaces to Enhance Microwave Imaging: Experimental Validation for Tomographic and Radar-Based Algorithms," IEEE Open Journal of Antennas and Propagation, vol. 3, pp. 89-100, 2021.

1.6 Thesis Structure

The remainder of the thesis is structured as follows. Chapter 2 discusses the background theory that is necessary for the development, validation and optimisation of microwave tomography algorithms. Chapter 3 presents the simulation and experimental procedure toward the validation of the 2-D DBIM-TwIST algorithm for brain stroke detection and classification using a brain phantom. Also, it presents the work that has been conducted during the secondment at Keysight that has explored the fabrication of a novel solid material that could enhance antenna performance. Chapter 4 validates the 3-D version of DBIM-TwIST first for simulated realistic scenarios. Then it presents a novel multi-layer head phantom and validates both the 2-D and 3-D versions of the DBIM-TwIST for different stroke scenarios. It also presents the results obtained during the secondment at POLITO in relation to the validation of DBIM-TwIST in an alternative imaging prototype. Conclusion of the thesis and future work are provided in Chapter 5.

Chapter 2

Literature Review and Background Theory Work

2.1 Literature Review

2.1.1 Introduction to Microwave Medical Imaging

MWI technology incorporates the applications and the techniques that use non-ionized EM radiation, within the range of 300 MHz to 300 GHz, with the aim of sensing and imaging a dielectric difference located in an investigation domain of interest [43]. This frequency range includes both microwave and millimeter wave bands, but they can both be grouped under MWI, as they use electromagnetic radiation. MWI has been used in a range of applications such as non-destructive testing and evaluation, concealed weapon detection at security checkpoints, structural health monitoring, detection and identification of objects in marine engineering, archaeology, and industrial design, as well as, through-the-wall imaging. However, for the reasons that are mentioned in the previous chapter, MWI for medical applications has attracted a lot of interest [44]-[46].

The interaction of EM radiation with human tissues has been widely studied in the past and gained a lot of interest due to the prospective advantages it can offer [47]. Many studies investigated and measured the dielectric properties of biological tissues

at microwave frequency range [48]. The outcomes of these studies showed that there is a difference between the dielectric properties of healthy and malignant tissues, due to changes in the water content [49]. For example, the dielectric properties (permittivity and conductivity) of an area in the brain affected by a stroke, differs from the ones of healthy brain tissue [3].

MWI relies on the dielectric contrast between the healthy and diseased tissues [50]. In MWI, the region of interest (ROI) is surrounded by measurement probes that radiate EM signals. The signals are received by the same or a different probe, and the scattered or reflected signals are processed with various techniques to locate, shape and reconstruct an existing dielectric contrast [44]. A two-dimensional (2-D) or a three-dimensional (3-D) dielectric map is formed, which visualizes the permittivity and the conductivity of different tissues or the location of a strong scatterer inside the ROI. The use of non-ionizing radiation, the low cost of MWI systems and the portability, are the main motivations that have established MWI as a promising and non-invasive alternative to the current medical imaging techniques [2],[8],[9].

On the other hand, there are several challenges that MWI systems should address [51]-[10]. The biggest challenge is the insufficient coupling of energy into the human body. Any microwave radiation produced in the air will reflect significantly at the tissue interface due to the considerable electrical differences between air and living tissue. Furthermore, the multi-layer anatomy of the human tissues reflects back the signals and attenuates them, limiting the penetration depth [52]. To overcome this challenge, a coupling medium is used [10] to minimize the reflections and optimize the transmission to the tissue-air interface. In addition, the coupling medium extends the antenna bandwidth and reduces unwanted reflections from the apparatus [53].

Notwithstanding that the coupling medium can reduce the mismatch between the air and different tissues, it can also generate power loss due to spillovers and dissipation in the coupling liquid. Moreover, the use of coupling liquid is not always practical for clinical implementations [52]. To this end, some studies have proposed the integration of the antennas in novel solid and flexible materials with similar dielectric properties

as the coupling liquids [9],[53]. Therefore, the acquisition system could be adjusted according to the size, shape and anatomy of the examined tissues. However, most MWI setups suffer from low dynamic range, as a consequence of the losses of the coupling mediums, the efficiency of the sensors and the sensitive data acquisition process [52]. A high dynamic range is essential to achieve the optimal trade-off between the required resolution and incident power which is needed for medical imaging applications [54].

In order to improve resolution and enable the use of compact antenna elements, higher frequencies must be used. However, this results in less EM field penetration inside the lossy biological tissue. Additionally, increased resolution leads to increased computational time [55]. As a consequence, another problem that needs to be resolved is the choice of the optimal frequency band. The theoretical approach in [56] suggested that a working frequency up to 1.5 GHz can achieve the optimal trade-off between the required resolution and incident power needed for head imaging applications.

The operational frequency range, which heavily depends on the dielectric characteristics of the target and coupling medium, has a significant impact on the antenna selection. An additional difficulty of MWI systems is the size of the antenna elements. Furthermore, the antenna should be easily and accurately simulated in the forward model. Enhancing matching between the array and the head tissues is the primary goal of employing an appropriate immersion medium. However, it also makes it possible to reduce the size of the antenna elements, making its application in head imaging a significant practical problem as smaller antennas do not have a wide frequency range. Realistically, a trade-off must be found between the antenna size, dielectric contrast, penetration depth and spatial resolution requirements [11].

An additional challenge of MWI systems is the non-automated process between the Vector Network Analyzer (VNA) and the computer employing the MWI software. During the data acquisition process, it is critical to promptly gather the scattering parameters (S-parameters) data and minimize any experimental errors, by replacing the VNA with a specialized portable microwave module [57].

2.1.2 Dielectric Spectroscopy

As MWI techniques for medical applications rely on the dielectric contrast between healthy and diseased tissues, the dielectric properties of human tissues have been extensively studied. Dielectric spectroscopy in the past has been characterized by measurement hardware limitations [58]. Nowadays, the experimental methods for dielectric spectroscopy have developed significantly and automatic spectrometers can easily measure the entire spectral range from 10^{-6} to 10^{12} Hz [59],[60]. The most widely used technique to measure the dielectric properties of a tissue or phantom is the open-ended coaxial probe [61]. The coaxial probe method uses a truncated coaxial transmission line that propagates the EM field along its axis. Where the EM field encounters an impedance mismatch between the probe and the sample material, reflections take place. Then, the VNA captures the reflections and calculates the material's dielectric characteristics [53]. In a study conducted by [62], the common swept frequency VNA from the system was replaced by a compact microwave transceiver which uses a new broadband, multi-tone source and broadband receivers to measure the direct S-parameters at multiple tones coincidentally. Before measuring sample materials, a complete calibration of the dielectric characteristics is carried out to prevent systematic inaccuracies [63]. The Debye model is employed to capture the frequency-dependent behaviour of human tissues. The theory of the Debye model will be elaborated in the next section.

Gabriel and Gabriel [64],[65] provided an extensive summary of different measured dielectric properties both in vivo and ex vivo. This work is considered to be the primary source of information on the characteristics of human tissues, and numerous databases were built using this data. There are also many studies that focus on tissues of specific body regions like breast, heart, liver and bone [61]. A large-scale dielectric spectroscopy study was conducted by [66] for the dielectric properties of normal breast tissues. Recent studies by [67] and [68] observed a large degree of heterogeneity between healthy and cancerous breast tissues and across patients. However, [69] found that the dielectric difference between healthy and cancerous breast tissue ranges from 1.1 to

5 over the frequency range of 0.5 to 20 GHz. Amin et. al reviewed the dielectric properties of bones for the monitoring of osteoporosis [70]. Other dielectric studies measured the dielectric properties of liver [71]-[73]. A study by [74] measured the dielectric properties of different parts of the heart, concluding that the properties vary between the different heart parts and as a consequence, heart should not be considered as a homogeneous tissue.

Specifically for head tissues, [75] measured in vivo and in vitro the dielectric properties of white and grey matter as well as the properties of cerebrospinal fluid (CSF) in a frequency range of 50 MHz–20 GHz, finding similar properties with the literature. Schmid et al. conducted an ex vivo study in 20 human brains, less than 10 hours after death [76]. It was reported that grey matter permittivity had a similar value with the reference properties at a frequency range of 800 to 2450 MHz, but the grey matter conductivity at room temperature was found to be slightly higher than the conductivity reported by Gabriel. A more recent study by Semenov examined the dielectric properties of the brain during ischemia. Measurements were conducted in vivo in seven 3-month-old female Yorkshire domestic cross/farm pigs under anaesthesia. Following a craniotomy, occlusion and reperfusion measurements were conducted, when the animal was in stable condition, with a hand-held probe in contact with the surface of the cerebral cortex. The results showed that ischemia properties can vary from -10% up to -25% compared to the dielectric properties of healthy brain tissue [77].

2.1.3 Microwave Imaging Techniques

The proposed techniques for MWI follow two main paths which include microwave tomography (MWT) and microwave radar algorithms. MWT algorithms use the scattered fields to reconstruct the dielectric properties of a region of interest from experimental or numerical 3-D data and identify a target with unknown dielectric properties by solving an inverse scattering EM problem, with representations of the set-ups simulated by finite difference time domain (FDTD) or finite element method (FEM)-based

solvers [78].

However, these methods suffer from the non-linearity and ill-posedness of the inverse problem, which increases the complexity of the solution. Therefore, MWT methods require robust, yet time consuming, algorithms that allow tuning the parameters for each problem, as some form of apriori information is needed [79].

Several solutions have been proposed in the literature that include among others, the contrast source inversion (CSI) approach [80] and the linear inversion with truncated singular value decomposition (TSVD) [9],[81]. In [82], a multi-step learning-by-examples strategy has been presented and validated for brain stroke detection, identification, and localization, using a simplified head phantom made by an octagonal prism filled with the dielectric properties of the average brain and with circular cylinders which mimic the two types of the stroke. The study in [83] presented a novel non-linear S-Parameters inversion method for stroke imaging based on Lebesgue spaces with non-constant exponents. The experimental prototype included a liquid-filled 3-D SAM phantom that mimics the dielectric properties of the average brain in the presence of a stroke-like target. The presented simulation and experimental results at 1 GHz are very promising, but a further assessment of the method using a multi-layered phantom in a wider frequency range is needed.

The increased complexity of microwave brain imaging requires regularization of the problem and often adjusting the algorithm parameters for each case. As a consequence, a distorted Born iterative method with two-step iterative shrinkage thresholding (DBIM-TwIST) has been proposed in [84] where an inverse scattering problem is solved at each iteration.

Past research on DBIM-TwIST focused on the 2-D algorithms as they are easier to model and solve. 3-D algorithms are associated with very high computational costs and are challenging to solve as the ill-posedness of the inverse problem increases significantly with the increase in the number of unknowns. Some 3-D methods for MWT applications in medical imaging have been presented in [12]-[87] but mainly for breast imaging. For the problem of head imaging, [88] and [89] used scattering signals

from 3-D head phantoms applying FDTD and FEM, respectively, while [9] suggested incorporating FEM with TSVD. Recent work by [90] presented a 3-D version of the DBIM, combined with the fast iterative shrinkage/thresholding algorithm (FISTA) for microwave head imaging, with some promising results for realistic cases.

Regarding MWT systems for stroke detection, two different portable prototypes were presented in [9] and [91] for stroke monitoring and detection. Furthermore, [92] presented a container incorporating 10 antennas, that reconstructed targets in various positions using a Gauss-Newton algorithm with Tikhonov regularization. Semenov evaluated the optimal technical and performance characteristics of a MWT device. The projected signal attenuation showed that the key point is to design a device that has good sensitivity, as well as high resolution [93]. Higher resolution can be achieved in higher frequencies, however higher frequencies result in higher attenuation and a small signal-to-noise ratio (SNR). To attain the sensitivity, specificity and, resolution required for medical imaging, it is particularly desirable to achieve a high SNR, ideally between 40-60 dB. Therefore, a frequency range of 0.5-1 GHz could be the optimal in order to achieve the required trade-off between successful detection and good resolution. Moreover, it was found that the smallest target area that can be reconstructed with an inversion method is about 2 cm [93]. However, a more recent study achieved the successful reconstruction of a target mimicking hemorrhagic stroke, with a diameter of 1 cm [91]. In general, a typical stroke size is around 2 cm [94].

In addition, the design of a MWT scanner for brain imaging has been analysed in [56] using a transmission line model to determine suitable frequencies and properties of the coupling medium and using the singular value decomposition (SVD) of the scattering operator in [54] to optimize the antenna array design. The aim of the study presented in [3] was to differentiate the hemorrhagic from the ischemic stroke and monitor the evaluation of the ischemic stroke. Simulations and two experimental setups were used to produce the data. Image reconstructions were achieved both with FEM and FDTD approach. Phantoms were prepared using the dielectric properties reported in [64] and [65]. It was confirmed that the higher contrast of hemorrhagic

stroke improves detection relative to ischemic stroke detection. This paper contributed significantly to the literature as it presented reconstruction results of different phases of the stroke, including penumbra, which is the ischemic layer that is created around the core of the stroke, and the oedema that could be developed.

Alternatively, microwave radar-based techniques solve a less complex problem of discovering a scattering map contingent on the contrast present between the dielectric properties of healthy and malignant tissues. This technique was first designed for military purposes but then applied for detecting malignancies in the human body. It was developed in the late 1990s by Hagness at Wisconsin University, and Benjamin at Bristol University [95]-[99]. Research teams at [100], [101] annd [102] have also contributed into the development of radar-based methods for medical applications. The radar-based Huygens algorithm, initially presented in [103], has shown its potential for use in medical applications [104]. A new hybrid imaging method was proposed at [105], using information from a radar-based algorithm to locate the target and then apply MWT to reconstruct the dielectric properties of the head, gaining promising preliminary results.

Recently, machine learning approaches have also been proposed for brain stroke classification. More specifically, [106] conducted animal experiments using a non-contact microwave-based stroke detection system for classifying the type of the stroke, as well as monitoring the severity and the progress of the stroke by using different metrics. Chalmers university has developed and clinically tested a prototype [37] for detecting the type of stroke. Other studies by [82] and [107]-[109] have shown that machine learning methods for stroke classification are quick and robust and can provide accurate results, howbeit, a large data set is needed to be trained. Moreover, the lack of images could act as a disadvantage for clinical applications.

2.2 Propagation of Electromagnetic Waves

This section discusses the basic EM and microwave theory, while it also introduces the FDTD method, which is used to simulate the propagation of EM waves as a forward solution.

2.2.1 Maxwell's Equations

Maxwell's equations form the foundation of electromagnetism. The entire EM spectrum, from X-rays to radio waves, is governed by this set of equations as described below:

$$\begin{aligned} \frac{\partial \vec{B}}{\partial t} &= -\nabla \times \vec{E} && \text{Faraday's law} \\ \frac{\partial \vec{D}}{\partial t} &= -\nabla \times \vec{H} - \vec{J} && \text{Ampère's law} \\ \nabla \cdot \vec{D} &= \rho && \text{Gauss's Law} \\ \nabla \cdot \vec{B} &= 0 && \text{Gauss's Law for Magnetism} \end{aligned} \tag{2.1}$$

In 2.1, $\vec{D}$ is the electric displacement field, $\vec{B}$ the magnetic displacement field, $\vec{E}$ the electric field, $\vec{H}$ the magnetic field, $\vec{J}$ the current density, ρ is the electric charge density and t denotes time. When a material is linear and isotropic, the following conditions apply:

$$\begin{aligned} \vec{D} &= \varepsilon \vec{E} \\ \vec{B} &= \mu \vec{H} \\ \vec{J} &= \sigma_e \vec{E} \\ \vec{M} &= \sigma_m \vec{H} \end{aligned} \tag{2.2}$$

where ε is the permittivity, μ is the permeability, σ_e is the electrical conductivity, M, the equivalent magnetic current density and σ_m the magnetic conductivity [110].

The substitution of 2.2 to 2.1 results in two partial differential equations that need to be solved. This substitution eliminates the electric and magnetic displacement field, the electric field density and the magnetic field density terms from the Maxwell equations. These partial differential equations are as follows:

$$\begin{aligned} \varepsilon \frac{\partial \vec{E}}{\partial t} &= -\nabla \times \vec{H} - \sigma_c \vec{E} - \vec{J} \\ \mu \frac{\partial \vec{H}}{\partial t} &= -\nabla \times \vec{E} - \sigma_m \vec{H} - \vec{M} \end{aligned} \tag{2.3}$$

A differential form in rectangular coordinates is shown below:

$$\begin{aligned} \mu \frac{\partial H_x}{\partial t} &= \frac{\partial E_y}{\partial z} - \frac{\partial E_z}{\partial y} - \sigma_m H_x - M_x \\ \mu \frac{\partial H_y}{\partial t} &= \frac{\partial E_z}{\partial x} - \frac{\partial E_z}{\partial y} - \sigma_m H_y - M_y \\ \mu \frac{\partial H_z}{\partial t} &= \frac{\partial E_x}{\partial y} - \frac{\partial E_z}{\partial y} - \sigma_m H_z - M_z \\ \varepsilon \frac{\partial E_x}{\partial t} &= \frac{\partial H_z}{\partial y} - \frac{\partial H_y}{\partial z} - \sigma_e E_x - J_x \\ \varepsilon \frac{\partial E_y}{\partial t} &= \frac{\partial H_x}{\partial z} - \frac{\partial H_z}{\partial x} - \sigma_e E_y - J_y \\ \varepsilon \frac{\partial E_z}{\partial t} &= \frac{\partial H_y}{\partial x} - \frac{\partial H_x}{\partial y} - \sigma_e E_z - J_z \end{aligned} \tag{2.4}$$

A common way to deal with differential equations is to approximate them numerically, by the FDTD method.

2.2.2 Finite-Difference Time-Domain Method

For complex EM problems, numerical techniques have been proposed to solve Maxwell's equations including the FEM, the Finite Volume Time Domain Method, the FDTD Method and the Finite Difference Frequency Domain (FDFD) Method. FDTD treats

a non-linear problem naturally, does not require a matrix inversion and can model an inhomogeneous object of arbitrary shape. Moreover, FDTD is a time domain method and as a result, it can obtain multiple frequency results by Fourier transform. For increasing mesh, FDTD appears to be less computationally expensive and easy to implement than FEM. Also, FDTD can be designed in parallel using graphics processing unit (GPU) that can significantly reduce the computational time for 3-D problems. As a result, the FDTD method is among the most popular, flexible, and conceptually simple techniques for simulating non-linear scenarios, hence it is used in this study to simulate the EM field scattered by the region of interest [111].

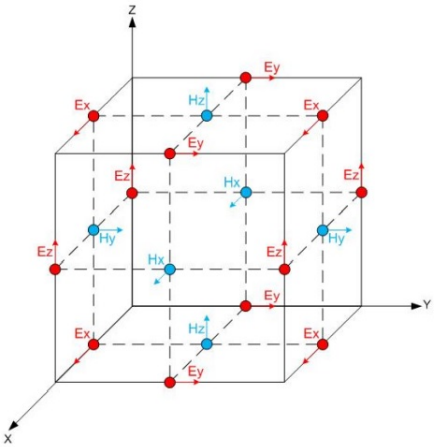

Figure 2.1: The Yee cell which denotes the electric and magnetic field vector components. The components of the electric field (red circle) are computed in the middle of the edges and the components of the magnetic field (blue circle) are centred on the surfaces. (source: fdtd.wikispaces.com)

The FDTD method was first introduced by Kane S. Yee in 1966 [112]. The method approximates the derivatives by finite differences. More specifically, both electric and magnetic fields are discretized in both space and time with central difference approximations, using uniform grids with Δx, Δy and Δz being the spatial dimensions of the grid. Each electric field vector component is located midway between a pair of magnetic field vector components, and conversely. A rectangular unit cell in this configuration is

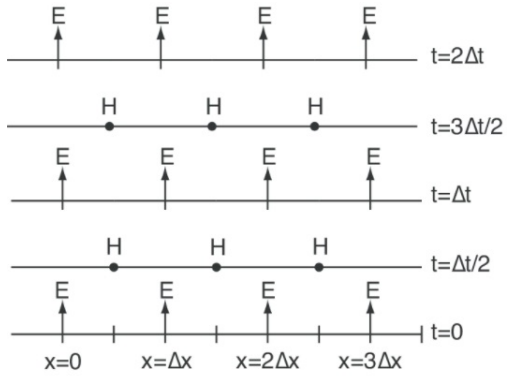

Figure 2.2: Leapfrog' flow of calculations of electric and magnetic fields through both space and time which results into the approximate solution to Maxwell's equations [111].

called Yee Cell and is shown in Fig. 2.1 for the electric field. In each Yee cell, the four electric-field values surround each magnetic-field value and every electric-field value is surrounded by four magnetic-field values.

Fig. 2.2 shows that the resulting finite-difference equations are solved in a leapfrog manner: the electric vector components are solved every (n+1) Δt while the magnetic field vector components in the same spatial volume are solved at the next instant in time (n+$\frac{1}{2}$) Δt . It is noted that $\vec{E}$ and $\vec{H}$ are shifted also in space by half of the discretization Δx. The fields are updated at every time step using the central difference method and the process is repeated until the maximum time step Δt is achieved [111].

To ensure stability, a field component cannot propagate more than one cell size in the time step Δt, according to Courant's criterion which must be satisfied at every mesh cell. This means that the maximum time step must satisfy the following inequality:

$$\Delta t \leq \frac{1}{u\sqrt{\frac{1}{(\Delta x)^2}+\frac{1}{(\Delta y)^2}+\frac{1}{(\Delta z)^2}}} \tag{2.5}$$

In 2.5, u is the velocity of propagation and Δx, Δy and Δz denote the spatial dimensions of the smallest element of the grid of the simulation. Since the fields are computed at different points, it is feasible to calculate separately the electric and the magnetic fields [113]. To implement Yee's algorithm, Maxwell's equations need to be

discretized and the differential equations must be replaced by finite differences. The basic theory to form the 2-D and 3-D FDTD which is used in this study to model the propagation of the EM wave, is presented in the Appendix A.

2.2.3 FDTD Absorbing Boundary Conditions

Electromagnetic field problems are unbounded in space. Hence, boundary conditions are needed to bring the infinite space to a finite computational domain. Without a terminating absorbing boundary, the wave that is radiated from the source will be reflected by this boundary and will propagate towards the source. Consequently, Maxwell equations cannot be applied in the boundary. Hence, absorbing boundary conditions (ABC) are introduced at the outer lattice boundary to simulate open boundary electromagnetic problems so that a solution obtained is an accurate approximation of the real solution that considers unlimited space surrounding it [114].

A different technique to achieve an ABC is to terminate the outer boundary of the space lattice in an absorbing material medium, simulating the effect of an anechoic chamber. Ideally, the absorbing medium should be a few units thick, able to produce zero reflections, highly absorbing, and effective in the near field of a source or a scatterer. Holland in [115], used a conventional lossy dispersionless absorbing medium. However, an absorbing layer like this can be applied only in the presence of normally incident plane waves.

Some of the most common absorbing boundary conditions include Mur's and Liao's implementations [116], [117]. In 1993, a new technique called Perfectly Matched Layer (PML) was presented by Jean-Pierre Berenger [118]. PML is designed to absorb incident waves with minimal reflections, irrespective of the frequency, polarisation and incidence angle. PML boundaries are basically implemented as an absorbing lossy and lossless material that is also impedance matched to the surrounding materials, to minimize reflections. PML implementation can be applied to both 2-D and 3-D FDTD problems. Furthermore, PML can be used as an absorbing boundary for simu-

lation spaces consisting of inhomogeneous, dispersive, anisotropic and non-linear media, which are not feasible analytically derived ABCs.

Fig. 2.3 illustrates PML implementation. The interior space forms the computational domain of a problem in which there is a source of incident waves. The computational domain is enclosed by an absorbing layer consisting of PML media. The outer boundary is terminated on a perfectly conductive surface.

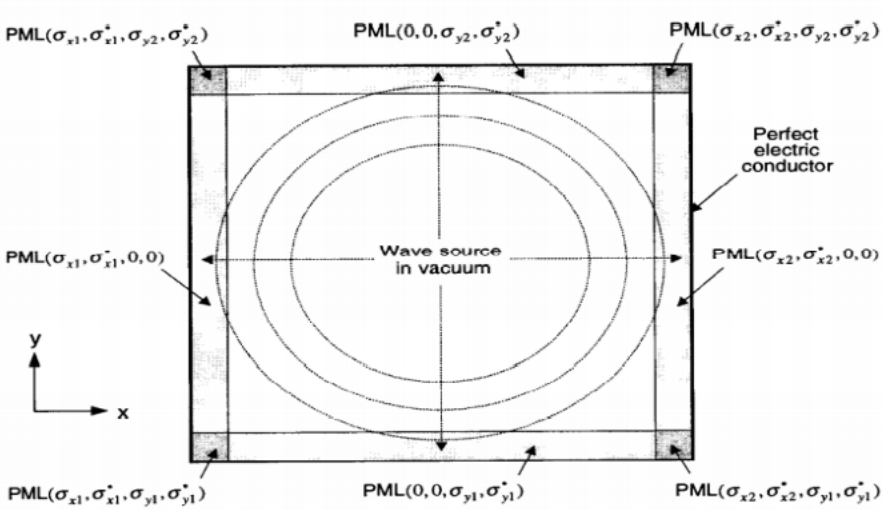

Figure 2.3: Simulation of the FDTD grid structure in free computational space using PML technique [111].

In order to enable the absorption of evanescent waves, the convolutional perfectly matched layer (CPML) was developed by Roden and Gedney in [119] based on a recursive convolution technique. The CPML is based on the stretched-coordinate form of Maxwell's equations using an additional stretching parameter to control late time low-frequency reflection and enhance absorption of grazing waves. When an incident wave arrives at the media-CPML interface, the latter will absorb the incident wave almost completely. To attain the expected effects, the parameters of the CPML are updated iteratively.

In particular, the application of the CPML can be adapted to account for inhomogeneous, lossy, anisotropic, dispersive, or non-linear media. For highly evanescent modes

or low-frequency excitations, the use of the classical complex stretching variable in the split-field PML can lead to large reflection errors. These issues can be overcome with the use of complex frequency, shifted (CFS) PML parameters with the proper scaling. In this thesis, the selection of the complex stretching variable will be as presented by Kuzuoglu and Mittra [120]:

$$s_i = \kappa_i + \frac{\sigma_i}{a_i + j\omega\epsilon}, \qquad \text{i = x, y or z} \tag{2.6}$$

where κ_i the scaling factor, a_i is the frequency-shifted factor and σ_i is the electric conductivity. In this study, the magnetic loss is considered to be 0. Employing the outcomes of [119], the CPML formulation is performed accordingly and is presented at Appendix B.

2.3 Debye Models for Frequency-Dependent Materials

The most commonly used models to describe the dispersive behaviour of human tissues include the Debye model and the Cole-Cole model. This is because a lossy dispersive wave equation is conducted completely by the frequency-dependent conductivity. Although the Cole-Cole model is considered to be the most accurate fitting tool for describing tissue dielectric characteristics, it is insufficient for effective numerical computation of electromagnetic fields. The Debye model is a vastly reliable fitting tool that allows very fast computation in a specific frequency range, in contrary to the Cole-Cole model which is more complex and is used in large classes of actual wideband sources [121].

The Debye model is a method developed by Peter Debye [122] and was originally used in thermodynamics and solid state physics [123]. Its use was extended in bioelectromagnetics, to numerically model a frequency-dispersive biological medium in

time domain [124]. As a lossy dispersive wave equation is conducted completely by the frequency-dependent conductivity, the Debye model is often used to model human tissues. More specifically, the Debye model is applied to capture the frequency-dependent dielectric properties of human tissues [97]. The frequency-dependent relative permittivity in the Debye model is defined as follows:

$$\epsilon_r(\omega) = \epsilon_\infty + \sum_{p=1}^{p} \frac{\Delta\epsilon_p}{1 + j\omega\tau_p} \tag{2.7}$$

where p is the number of Debye poles, $\Delta\epsilon_p$ is the difference of the relative permittivity under the corresponding Debye poles, τ_p is the relaxation time at the p-th Debye pole, ω is the angular frequency [64] and ϵ_∞ is the relative permittivity at the high-frequency limit ($\omega\tau >> 1$), which is also known as optical relative permittivity [122].

If $p = 1$ the single-pole Debye model can be acquired which is written as follows:

$$\epsilon_r(\omega) = \epsilon_\infty + \frac{\epsilon_s - \epsilon_\infty}{1 + j\omega\tau} \tag{2.8}$$

ϵ_s is the relative permittivity at the low-frequency region ($\omega\tau >> 1$).

The real and the imaginary part of the complex relative permittivity can be depicted as follows:

$$\epsilon' = \epsilon_\infty + \frac{\epsilon_s - \epsilon_\infty}{1 + \omega^2\tau^2} \tag{2.9}$$

$$\epsilon'' = \frac{(\epsilon_s - \epsilon_\infty)\omega\tau}{1 + \omega^2\tau^2} \tag{2.10}$$

The total current density J can be expressed as a sum of the conduction current density J_c and the displacement current density J_d as follows:

$$J = J_c + J_d \tag{2.11}$$

Also, according to Ohm's Law and to the first Maxwell equation:

$$\begin{aligned} J_c &= \sigma_s E \\ J_d &= \frac{\partial D}{\partial t} = j\omega\epsilon_0\epsilon E \end{aligned} \tag{2.12}$$

Therefore, by substituting Equation 2.12 into Equation 2.11, the total current density can be expressed considering the electrical conductivity as a complex value:

$$\begin{aligned} D = \epsilon_0\epsilon E + \frac{\sigma_s}{j\omega}E = (\epsilon_0\epsilon + \frac{\sigma_s}{j\omega})E = \epsilon^*\epsilon_0 E \\ \epsilon^* = \epsilon + \frac{\sigma_s}{j\omega\epsilon_0} \end{aligned} \tag{2.13}$$

Consequently, the Debye first-order model can be applied to model the dispersive behaviour of the complex relative permittivity as follows:

$$\epsilon_r(\omega) = \epsilon_r'(\omega) - j\epsilon_r''(\omega) = \epsilon_\infty + \frac{\Delta\epsilon}{1 + j\omega\tau} + \frac{\sigma_s}{j\omega\epsilon_0} \tag{2.14}$$

where the real part $\epsilon_r'(\omega)$ is the frequency-dependent dielectric constant and the imaginary part $j\epsilon_r''(\omega)$ is the frequency-dependent dielectric loss which can be translated into the effective conductivity $\sigma(\omega) = \omega\epsilon_0\epsilon''(\omega)$. ϵ_∞ is the relative permittivity at infinite frequency, $\Delta\epsilon$ is the difference between the zero-frequency relative permittivity ϵ_s and the relative permittivity at infinite frequency ϵ_∞, τ is the relaxation time, ω is the angular frequency, σ_s is the static conductivity and ϵ_0 is the permittivity of free space.

In this study, the dielectric properties of human tissues are calculated using the single-pole Debye model. The frequency range of interest for the examined scenarios is from 0.5 to 2.5 GHz. The estimations of the Debye models for different head tissues are derived by performing curve-fitting on the data that are acquired from dielectric spectroscopy.

2.4 Inverse Scattering Problems

Inverse scattering problems are problems of determining the characteristics of an unknown object according to how it scatters the incoming radiation from field measurements in the accessible region [125]. Fig. 2.4 illustrates the EM scattering problem where the given incident field and EM properties of the background field, determine the EM properties and morphology of the "scattering system" from the measured scattered fields.

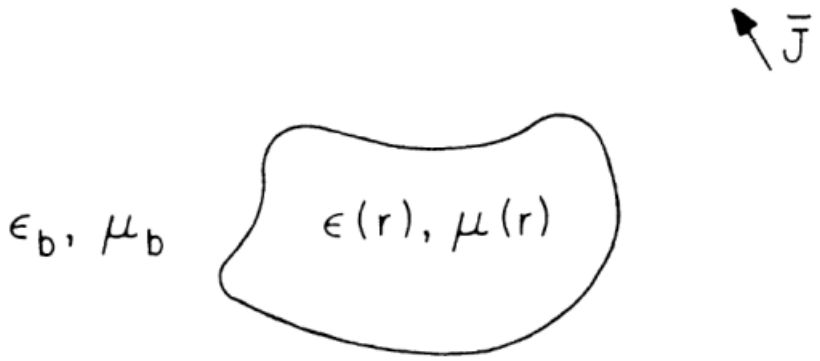

Figure 2.4: A current source radiating in the vicinity of a general inhomogeneity [111].

A popular approach to solve the scattering problem is by using volume integral equations where the unknowns in the problem are expressed in terms of the flowing current volume in the inhomogeneity [126]. The current volume is composed by the conduction current and the displacement current induced by the total electric field. Then, an integral equation is formed from which the total field can be solved [127].

Next, the mathematical formulation of EM scattering is analysed. Considering Maxwell's equations theory, it is assumed that the electric field satisfies the following equation:

$$\nabla \times \mu(\vec{r})^{-1} \nabla \times \vec{E}(\vec{r}) - \omega^2 \epsilon(\vec{r}) \vec{E}(\vec{r}) = \iota\omega \vec{J}(\vec{r}) \tag{2.15}$$

where $\mu(\vec{r})$ and $\epsilon(\vec{r})$ are functions of position inside the inhomogeneous region V. By subtracting the term $\nabla \times \mu_b(\vec{r})^{-1} \nabla \times \vec{E}(\vec{r}) - \omega^2 \epsilon(\vec{r}) \vec{E}(\vec{r})$ from both sides of the

equation, the resulted equation is obtained:

$$\begin{aligned}\nabla \times (\mu(\overrightarrow{r})^{-1} - \mu_b(\overrightarrow{r})^{-1})\nabla \times \overrightarrow{E}(\overrightarrow{r}) - \omega^2(\epsilon(\overrightarrow{r}) - \epsilon_b(\overrightarrow{r}))\overrightarrow{E}(\overrightarrow{r}) \\ = \iota\omega\overrightarrow{J}(\overrightarrow{r}) - \nabla \times \mu_b(\overrightarrow{r})^{-1}\nabla \times \overrightarrow{E}(\overrightarrow{r}) - \omega^2\epsilon(\overrightarrow{r})\overrightarrow{E}(\overrightarrow{r})\end{aligned} \tag{2.16}$$

The dyadic Green's function in the absence of the scatterer is formed as follows:

$$\nabla \times \mu_b(\overrightarrow{r})^{-1}\nabla \times \overrightarrow{G}(\overrightarrow{r}, \overrightarrow{r}') - \omega\epsilon(\overrightarrow{r})\overrightarrow{G}(\overrightarrow{r}, \overrightarrow{r}') = \mu_b(\overrightarrow{r})^{-1}\overrightarrow{I}\delta(\overrightarrow{r} - \overrightarrow{r}') \tag{2.17}$$

By combining Equation 2.16 and Equation 2.17, the integral equation is formulated:

$$\begin{aligned}\overrightarrow{E}(\overrightarrow{r}) = \iota\omega\int_V dr'\overrightarrow{G}(\overrightarrow{r}, \overrightarrow{r}')\cdot\mu_b(\overrightarrow{r})\overrightarrow{J}(\overrightarrow{r}') + \omega^2\int_V dr'\overrightarrow{G}(\overrightarrow{r}, \overrightarrow{r}')\cdot(\epsilon(\overrightarrow{r}) - \epsilon_b(\overrightarrow{r}))\overrightarrow{E}(\overrightarrow{r}') \\ - \int_V dr'\overrightarrow{G}(\overrightarrow{r}, \overrightarrow{r}')\cdot\mu_b(\overrightarrow{r})\nabla' + (\frac{1}{\mu(\overrightarrow{r})} - \frac{1}{\mu_b(\overrightarrow{r})})\nabla' \times \overrightarrow{E}(\overrightarrow{r}')\end{aligned} \tag{2.18}$$

The first term of the Equation 2.18 is considered to be the incident field, therefore (2.18) becomes:

$$\begin{aligned}\overrightarrow{E}(\overrightarrow{r}) = \overrightarrow{E}_{inc}(\overrightarrow{r}) + \omega^2\int_V dr'\overrightarrow{G}(\overrightarrow{r}, \overrightarrow{r}')\cdot(\epsilon(\overrightarrow{r}) - \epsilon_b(\overrightarrow{r}))\overrightarrow{E}(\overrightarrow{r}') \\ - \int_V dr'\overrightarrow{G}(\overrightarrow{r}, \overrightarrow{r}')\cdot\mu_b(\overrightarrow{r})\nabla' + (\frac{1}{\mu(\overrightarrow{r})} - \frac{1}{\mu_b(\overrightarrow{r})})\nabla' \times \overrightarrow{E}(\overrightarrow{r}')\end{aligned} \tag{2.19}$$

By substituting the complex permittivity, the two integrals of the above equation can be combined. Furthermore, by considering non-magnetic materials, $\mu = \mu_b = 1$. Hence, Equation 2.19 is simplified:

$$\overrightarrow{E}(\overrightarrow{r}) = \overrightarrow{E}_{inc}(\overrightarrow{r}) + \int_V dr'\overrightarrow{G}(\overrightarrow{r}, \overrightarrow{r}')\cdot O(\overrightarrow{r}')\overrightarrow{E}(\overrightarrow{r}') \tag{2.20}$$

where $O(\overrightarrow{r}') = \omega^2(\epsilon - \epsilon_b)$ over a finite domain V. In an inverse scattering problem, the only available information includes the data that are outside the scatterer. As a

result, the total field is connected to the object through the volume integral equation 2.20.

The integral in equation 2.20 includes information on the scatterer representing the scattered field $O(\vec{r}) = \kappa^2(\vec{r}) - \kappa_b^2$, where $\kappa^2(\vec{r}) = \omega^2\mu(\vec{r})\epsilon(\vec{r})$ is an inhomogeneous medium over a finite domain V. The scattered field is non-linear in relation to $O(\vec{r})$, as $\vec{E}(\vec{r})$ is a function of $O(\vec{r})$.

Fig. 2.5 illustrates a representation of an inverse scattering experiment. Each antenna r'' transmits a microwave signal while the antennas r in the array measure the scattered field. The solution of the volume integral equation can be solved numerically. In this study we employ the Born approximation which is presented in the next section.

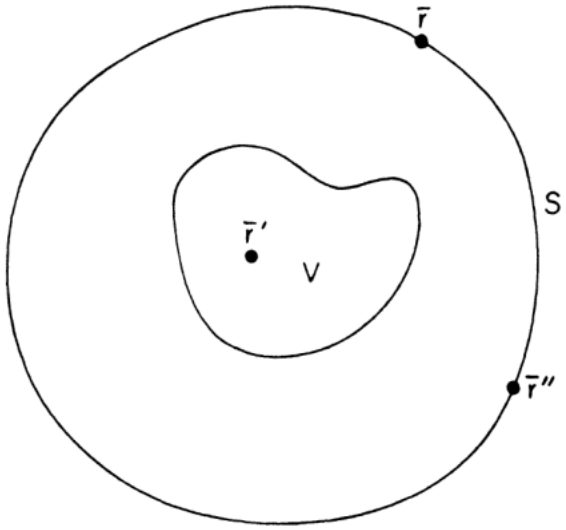

Figure 2.5: An inverse scattering experiment [111].

2.5 Distorted Born Iterative Method

When $O(\vec{r}) = \kappa^2(\vec{r}) - \kappa_b^2$ is small, or when the contrast of the scatterer is poor so the second term on the right of the Equation 2.20 is very small in comparison with the first term, the former is estimated as $\vec{E}(\vec{r}) \approx \vec{E}_{inc}(\vec{r})$. The total field in Equation 2.20 is approximated as follows:

$$\vec{E}(\vec{r}) = \vec{E}_{inc}(\vec{r}) + \int_V dr' \vec{G}(\vec{r}, \vec{r}') \cdot O(\vec{r}') \vec{E}_{inc}(\vec{r}') \tag{2.21}$$

This formulation is known as the first-order Born approximation. Born approximation considers a linear integral equation, however for inverse scattering EM problems the integral equation is non-linear. This is due to the non-linear relationship between the scattered fields and the inhomogeneity as a result of the multiple scatterers. Non-linearity increases as the body grows larger relative to the wavelength or as the contrasts of the inhomogeneity become larger [126]. References [128] and [129] demonstrate that the effect is less noticeable when operating at a lower frequency range. Consequently, a higher contrast inverse problem can be addressed at lower frequencies. A reliable method for resolving the inverse scattering problem includes an optimization approach. However, when the operating frequency is high, the non-linearity increases in the inverse problem and this could lead the algorithm to a local minima.

The frequency hopping method has been suggested by W.C. Chew and J.H. Lin to handle data from multiple-frequency microwave measurements [128]. In this paper it was suggested that the non-linear effect can be reduced by using the image reconstructed from low frequency data as the initial guess to the higher frequency problem. More studies showed that the reconstruction results obtained by using the frequency-hopping method are significantly improved when compared to using high frequency data directly [130],[131]. Furthermore, a frequency-hopping MWI algorithm does not require apriori knowledge of the inhomogeneous body. Our work at [132],[133] also revealed that frequency-hopping can significantly improve the reconstructed results in more challenging scenarios. Since frequency-hopping is a well-established concept in communication and network engineering, from now on we will refer to frequency-hopping MWI technique as microwave imaging frequency hopping (MWIFH). Results with MWIFH approach for the problem of brain stroke detection are presented in the next chapter.

As a result of the non-linearity, consecutive linear approximations are applied to

solve the non-linear equation [127]. Some popular inverse scattering methods include the Gauss-Newton optimization algorithms [134], [135] and the conjugate gradient techniques [136]. This study uses the Gauss-Newton solution of the inverse EM scattering problem that is more commonly known as DBIM [137]. More specifically, the contrast function $O(\vec{r}')$ is the difference between the complex relative permittivity of the background and object. The non-linear Born integral equation that relates the continuous spatial distribution of dielectric properties within V to the scattered electric field is given by:

$$\vec{E}(\vec{r}) = \vec{E}_{inc}(\vec{r}) + \int_V dr' \vec{G}(\vec{r}, \vec{r}', \epsilon_b) \cdot [\kappa^2(\vec{r}') - \kappa_b^2] \vec{E}_{inc}(\vec{r}') \tag{2.22}$$

As the measurement data are available only outside the scatterer in the inverse scattering problem, the only item available is:

$$\vec{E}_{sca}(\vec{r}) = \vec{E}(\vec{r}) - \vec{E}_{inc}(\vec{r}), r \in S \tag{2.23}$$

where $\vec{r} \in S$ and S is the surface outside V. As E_{sca} holds information on the scatterer, equation 2.22 can be composed as follows:

$$\vec{E}_{sca}(\vec{r}) = \int_V dr' \vec{G}(\vec{r}, \vec{r}', \epsilon_b) \cdot [\kappa^2(\vec{r}') - \kappa_b^2] \vec{E}_{inc}(\vec{r}') \tag{2.24}$$

The resulting equation is linear in $\kappa^2(\vec{r}') - \kappa_b^2$. However, multiple data are required to reconstruct $\kappa^2(\vec{r}')$ efficiently. Hence, an iterative method is applied in which the new $\kappa^2(\vec{r})$ is used to estimate κ_b^2.

Next, an updated $\vec{G}(\vec{r}, \vec{r}', \epsilon_b)$ is computed until a convergence is reached, as there are no analytical Green's functions available for the heterogeneous background profiles estimated at each iteration of the DBIM. For a point source at a specific antenna feed point r in V, the Green's function estimates the field received at a given antenna at r_m [12].

The inhomogeneous Green's function $\vec{G}(\vec{r}, \vec{r}', \epsilon_b)$ is related to the internal electric field. As a result of the differential equations controlling the Green's function and electric field, Green's function is acquired as follows:

$$\vec{G}(\vec{r}, \vec{r}', \epsilon_b) \approx \frac{i}{\omega\mu}\vec{E}_a(\vec{r}, \vec{r}', \epsilon_b) \tag{2.25}$$

where $\vec{E}_a(\vec{r}, \vec{r}', \epsilon_b)$ is the total electric field at the receivers, created by a 2-D point source inside V filled by the background medium.

By employing the reciprocity theorem, equation 2.25 can by given as [12]:

$$\vec{G}(\vec{r}, \vec{r}', \epsilon_b) \approx \frac{i}{\omega\mu}\vec{E}_b(\vec{r}', \vec{r}, \epsilon_b) \tag{2.26}$$

The 2-D version of DBIM is a simplified version of the 3-D formulation. For the 3-D EM inverse scattering problem, an $x-y$ horizontal plane is considered. Then, the 3-D inverse scattering problem is approximated, considering that only electric fields at the z-polarized antennas are significant [12]. Therefore, E_{xi} and E_{yi} are assumed to be zero and Equations 2.24 and 2.26 are applied for the z-directed tensor elements of the electric field and the dyadic Green's function, respectively. In principal, 3-D algorithms should include all three E-field components in the integral equation of the scattered field, but previous work [138] has shown that the scalar approximation does not affect the performance significantly. The validity of the scalar approximation has been also recently demonstrated for the head imaging problem by our group in [90].

The integral equation can then be linearized by discretizing Equation 2.24 combined with Equation 2.26 for all Tx-Rx pairs. The linearization of Equation 2.24 results in the following equation:

$$A(\omega)o = b(\omega) \tag{2.27}$$

where A is an $M - by - K$ propagation matrix, with M being the number of transmit-receive pairs in the antenna array and K the number of elements in the discretization

inside the reconstruction domain, while $b(\omega)$ is the $M - by - 1$ vector of the scattered fields recorded at the receivers. The $K - by - 1$ vector o is the unknown dielectric properties contrast function.

Solving the above equation derives into a discrete approximation $\hat{o}$ for the true value of the contrast function o. The approximate contrast function $\hat{o}$ is added iteratively to the background profile. This is then used to calculate the new background electric field and Green's function by employing FDTD simulations. The iterative implementation of this sequence of computations shapes the basis of the DBIM.

The DBIM algorithm starts with an initial guess ϵ_{b0} of the background profile. Hence, at the i-th iteration, the background electric field and the Green's function are calculated for the background profile ϵ_{bi}. The discretised equation is given by:

$$A_i(\omega)o_{i+1} = b_i(\omega) \tag{2.28}$$

The background profile is updated as:

$$\epsilon_{bi+1} = \epsilon_{bi} + \hat{o}_{i+1} \tag{2.29}$$

In this study, the FDTD simulations compute the fields in the entire region of interest, including both the background fields at the antennas and the reconstruction domain V. The complex permittivity values are replaced by the frequency-dependent Debye model and are updated at each DBIM iteration, thus are used to update the contrast function. In DBIM method first we need to linearise the problem by using approximation techniques such as the Born approximation, which results into an ill-posed problem.

2.6 Solution of the Linear Inverse Problem

2.6.1 Description of the Linear Inverse Problem

We assume solving for the n-vector x in the system of linear equations also presented as:

$$Ax = b \tag{2.30}$$

where A is a large $n \times n$ real symmetric matrix. The system is considered as compatible or consistent when the real vector b is in the range of A. When A is non-singular, the system is always compatible and Equation 2.30 has a unique solution. When A is singular and Equation 2.30 has at least one solution, then the singular system becomes consistent or compatible. That means that there will be infinite solutions to the problem. To acquire a unique solution, the minimum-length solution among all solutions x is chosen. On the contrary, if the singular system has no solution, it is considered as inconsistent or incompatible. In this instance, the singular symmetric least-squares problem is solved, and the minimum-length solution is chosen.

$$x = arg\,min\,||Ax - b||_2 \tag{2.31}$$

More specifically, the minimum-length least-squares problem can be described as:

$$min||x||_2\ s.t.\ x \in arg\,min\,||Ax - b||_2 \tag{2.32}$$

In the above equation, when A is linear, a linear inverse problem (LIP) is created. To approach a LIP, a solution $\hat{x}$ is defined as a minimiser of a convex object function $f : X = \mathbb{R}^m$ which is defined as follows:

$$f(x) = \frac{1}{2}||Ax - b||_2 + \lambda\Phi(x) \tag{2.33}$$

In the above equation, $\Phi(x)$ is a regularization function and $\lambda \in [0, +\infty]$ is the weighting parameter of the penalty term. Regularization methods are applied in MWI problems, which are ill-posed. By minimising f in the regularization framework, the ill-conditioness of the problem can be overcome and result into the inversion of A [81].

2.6.2 Direct vs Iterative Methods

Numerical methods for solving linear systems of equations can generally be divided into two classes. Direct methods, such as the Gaussian elimination method, yield the exact solution by carrying out a finite number of computations. These methods are not suitable for very large systems of equations due to rounding errors. Furthermore, forming and factoring a large matrix can be computationally expensive. However, direct methods are generally robust and they help to identify some basic structural properties such as sparsity or symmetry.

Iterative methods solve the system of linear equations by generating a sequence of vectors that are approximate solutions to the system of equations. An initial guess is used to approximate the solution and then the solution is used to enhance the approximation of the problem until a termination criterion is met. The round off errors do not accumulate, as each iteration creates a new approximation to the solution. Therefore, these methods are useful for problems involving very large matrices. In general, iterative methods try to estimate the actual solution as quickly and as accurately as possible, hence the algorithm can be stopped when the sequence of vectors approaches a solution that estimates the actual solution with minimum possible errors. This results into less computational cost. In general, if the iterations of the initial guess converge, iterative methods can be convergent.

There are two main types of iterative methods for linear systems: stationary iterative and non-stationary iterative. Stationary iterative methods solve a linear system by recasting the original system of equations in terms of its error or residual and can

be expressed in the simple form:

$$x^{k+1} = Bx^k + c \tag{2.34}$$

where neither B nor c depend upon the iteration count k. The four main stationary methods are the Jacobi method, Gauss-Seidel method, successive overrelaxation method (SOR), and symmetric successive overrelaxation method (SSOR).

Non-stationary methods include computations that their information change at each iteration. A specific type of non-stationary method is the Krylov subspace method (KSM):

$$\begin{aligned} \phi(x) &= \frac{1}{2}x^T Ax - x^T b \\ \nabla\phi(x) &= Ax - b \end{aligned} \tag{2.35}$$

The goal is to minimise $\phi(x)$ over $K_\kappa(A, b) = \text{span}\{b, Ab, A^2b, ..., A^{k-1}b\}$, with A being symmetric and positive definite. Most popular Krylov subspace methods include the Lanczos, Conjugate gradient, GMRES (generalized minimum residual), CGLS (Conjugate Gradient method for Least Squares), and MINRES (minimal KSM residual) [139].

2.6.3 Description of Iterative Shrinkage/Thresholding (IST) and Two-Step IST (TwIST)

IST Method

Iterative shrinkage/thresholding (IST) algorithms have been studied by a number of groups in different settings. The minimisation of functions given as sums of two convex functions was studied by Combettes and Wajs [140]. Figueiredo and Nowak investigated a function $\Psi(\cdot)$ as the log-likelihood function for a restoration problem with Gaussian noise, applied on an algorithm for EM problems [141]. Bredies, Lorenz and Maass considered the IST algorithm as a generalised conditional gradient algorithm [142].

The IST algorithm aims to find the minimiser in Equation 2.32, which is focused on the finite-dimensional case, where $X = \mathbb{R}^m, \Upsilon = \mathbb{R}^n$ and is formed as follows.

$$x_{t+1} = (1 - \beta)x_t + \beta\Psi_\lambda(x_t + K^t(y - Kx_t)) \tag{2.36}$$

where β is one of the parameters in the algorithm and $\beta > 0$. When $\beta = 1$ Equation 2.36 denotes the original IST algorithm. When $\beta \neq 1$, equation 2.36 indicates the relaxed versions of the IST algorithm. Every iteration of the IST algorithm includes sums, matrix-vector products by K and K^T, and the application of the denoising operation Ψ_λ [143].

TwIST Method

In this thesis, we use a method presented by Young in [144] and further analysed at [84] and [145]. More specifically, Young introduced a method of splitting the matrix into a structure of a two-step iterative equations, which is called the TwIST algorithm.

In MWI the goal is to approximate an unknown image vector x from the observation vector y and is described by the linear equation $Ax = y$. An approach is to determine a solution $\hat{x}$ as a minimiser of a convex objective function convex object function $f : X \to \mathbb{R} = [-\infty, +\infty]$ defined as:

$$f(x) = \frac{1}{2}||y - Ax||_2 + \lambda\Phi(x) \tag{2.37}$$

These ill-posed inverse scattering approaches suffer from non-uniqueness and need regularisation to reach convergence to a significant solution [84]. In the above equation, $\Phi(x)$ is a regularization function for the convex optimisation problem and $\lambda \in [0, +\infty]$ is a weighting parameter.

In the linear system $Ax = y$ with positive definite A, A can be split as $A = C - B$ in a way that C is positive definite and simple to invert. A stationary two-step iterative method (TwIST) for solving b is described as

$$\begin{aligned} x_1 &= x_0 + \beta_0 C^{-1}(b - Ax_0) \\ x_{t+1} &= (1-a)x_{t-1} + ax_t + \beta C^{-1}(b - Ax_t) \end{aligned} \tag{2.38}$$

for $t \geq 1$, x_0 is the initial vector and a, β, β_0 are the parameters of the algorithm.

For large sparse linear problems, the terms C and R of the splitting of vector A are modified as follows:

$$\begin{aligned} C &= I + \lambda D_t \\ R &= I - K^t K \end{aligned} \tag{2.39}$$

By considering $A = \lambda D_t + K^t K$, the two-step $Ax = K^t y$ can be obtained:

$$x_{t+1} = (1-a)x_{t-1} + (a-b)x_t + \beta C^{-1}(x_t + K^t(y - Kx_t)) \tag{2.40}$$

If we consider $a = 1$ and replace the multiplication matrix C^{-1} with the denoising function Ψ_λ, then the two iterative equations are developed as follows:

$$\begin{aligned} x_{t+1} &= (1-a)x_{t-1} + (a-b)x_t + \beta\Gamma_\lambda(x_t) \\ \Gamma_\lambda(x) &= \Psi_\lambda(x + A^t(y - Ax)) \end{aligned} \tag{2.41}$$

where a and β are the TwIST parameters. The term "two-step" is used as the following estimate x_{t+1} depends not only on the current solution x_t but also on the preceding solution x_{t-1}. In this study, the weighting parameter λ is defined as zero.

As mentioned in [145], convergence is possible when $0 < a < 2$ $0 < b < \frac{2a}{\lambda_m}$ where λ_m stands for the largest eigenvalues of the matrix $A^T A$. The optimised values of the parameters a and β can be acquired by the factor of optimal asymptotic convergence below:

$$\begin{aligned} a &= p^2 + 1 \\ \beta &= \frac{2a}{\lambda_1 + \lambda_m} \\ \rho &= \frac{1 - \sqrt{k}}{1 + \sqrt{k}} \end{aligned} \tag{2.42}$$

where λ_1 and λ_m are the smallest and largest eigenvalues of the matrix $A^T A$ respectively, and $k = \frac{\lambda_1}{\lambda_l}$ is the inverse condition number [145].

In MWI inverse scattering problems, the matrix $A_{m \times n}$ is an ill-posed matrix with $m << n$, where m is the number of measurements and n is the number of unknown dielectric values. The eigenvalues of the matrix $A^T A$ range from near to zero to larger than one, creating an unstable iterative process. As a result, the matrix is normalized in order to apply TwIST by appropriately selecting the smallest eigen value. Another crucial component of the TwIST algorithm is the so-called tolerance which controls how many TwIST iterations are performed at each DBIM step.

2.7 Summary

In this chapter we presented the literature review and state of the art of microwave medical imaging, as well as, the basic theory of electromagnetic wave propagation beginning from Maxwell's equations. Then, we introduced the FDTD method based on the Yee Cell theory and the absorbing boundary conditions of the method. Moreover, the Debye model, which is used to express the frequency dependence of the dispersive human tissues, was analysed. Furthermore, the basic theory of the inverse problems was presented and the distorted Born iterative method was analysed as a method that overcomes the non-linearity of an inverse scattering problem by converting the non-linear problem to a linear problem that then can be resolved by iterative methods. Finally, the IST/TwIST iterative methods were introduced and analyzed to overcome the ill-posedness of a linear system.

Chapter 3

Experimental Validation of MWT with a Simplified Phantom

In this chapter, we present an initial simulation and experimental validation of a MWT prototype for brain stroke detection and classification using the DBIM-TwIST algorithm. The experimental validation consists of first preparing and characterizing gel phantoms which mimic the structure and the dielectric properties of a simplified brain model with a hemorrhagic or ischemic stroke target. Then, we measure the S-parameters of the phantoms in our experimental prototype and process the scattered signals from 0.5 to 2.5 GHz using the DBIM-TwIST algorithm to estimate the dielectric properties of the reconstruction domain. We have also validated the algorithm by replicating the experimental scenario on CST. The results show that we are able to detect the stroke target in scenarios where the initial guess of the inverse problem is only an approximation of the true experimental phantom. Moreover, the prototype can differentiate between hemorrhagic and ischemic strokes based on the estimation of their dielectric properties. We also present the reconstruction results from measurements on a 3-D-printed anthropomorphic head model, containing a cylindrical target simulating the bleeding during a hemorrhagic stroke. In the last section, we present the work that has been conducted during the secondment at Keysight and has examined

the preparation of a novel solid material that could improve antenna performance.

3.1 Introduction

As mentioned in the previous chapters, MWT methods are challenged by the high heterogeneity of the human body [55] as well as the increased computational cost that arises from the non-linearity of the problem and the non-uniqueness of the solution [146]. Therefore, DBIM-TwIST solver which has presented in the previous chapter has been developed in [84] and [147] for microwave breast imaging. The algorithm was then incorporated successfully in a prototype tested in experiments with simple cylindrical targets [148]-[150] and showed advantages in comparison with other DBIM linear solvers like CGLS or IST [84],[147],[150].

Taking into account the challenges of MWT systems and the medical requirements for brain stroke detection and differentiation, this chapter validates experimentally DBIM-TwIST and the prototype for stroke imaging, using brain tissue and stroke mimicking phantoms. To this end, we present reconstruction results across a wide frequency range, which demonstrate the potential of differentiating between stroke types based on a quantitative estimation of their dielectric properties. Moreover, we show the method's robustness to differences in the dielectric properties of the background medium in our inverse phantoms relative to the phantom used in the experiment. We, therefore, believe that these experimental results provide further evidence of MWT's potential to detect strokes based on microwave images produced by a carefully designed system and algorithm.

This chapter mainly demonstrates reconstruction results for hemorrhagic and ischaemic mimicking targets, and for phantoms with different dielectric properties than the initial guess used in the inversion.

3.2 Methodology

3.2.1 Phantoms Preparation and Characterization

Experimental testing of MWT systems is critical in order to assess their potential for clinical applications. To this end, phantoms that mimic the dielectric and structural properties of the human head and brain provide efficient, easy to fabricate, and low-cost testbeds for experimental validation prior to clinical trials. Gelatine emulsions made of oil, water and gelatine are popular recipes for preparing such phantoms, as they are cheap and easy to alter, but can suffer from dehydration. McDermott et al. have proposed an alternative method of constructing solid phantoms made of ceramic and carbon powder, in which solid phantoms were fabricated with polyurethane, graphite, carbon black and isopropanol, to mimic the dielectric properties of the brain and the average properties of the layers surrounding the brain [151]. Solid phantoms are electrically and mechanically stable as well as reusable, but are more difficult to fabricate, time consuming, more expensive than the liquid phantoms, and not easy to modify for additional adjustments in properties or geometry. In [152], an alternative method of 3-D printed moulds filled with fluid TX100 salted water mixtures that can mimic the dielectric properties of head tissues was proposed. Those phantoms are cheap, easy to alter, reusable and stable. They require, however, plastic mould materials which can cause disturbances in the scattered signals [153].

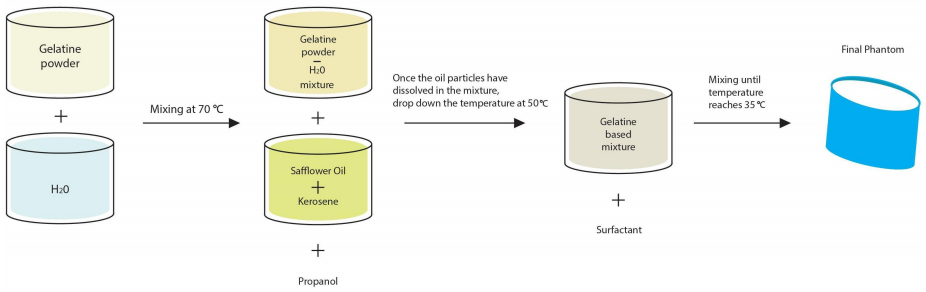

Figure 3.1: Schematic representation of the phantoms' preparation process.

As the aim of this chapter is to validate DBIM-TwIST in more realistic, yet sim-

plified cases for brain stroke detection and classification, we have constructed simple phantoms based on the materials and processes proposed in [154] for breast phantoms. Using different gelatine-oil concentrations compared to those for breast tissues, we have fabricated tissue-mimicking materials with specific dielectric properties that mimic average brain tissue, CSF, blood and ischaemia. The process is illustrated in Fig. 3.1. First, a water-gelatine mixture was prepared and mixed at 70°C, until the gelatine particles were fully dissolved into water and the mixture is transparent. Propanol was added to deal with the creation of air bubbles on the surface. Once heated to 70°C, we added a 50% kerosene-safflower oil solution into the water-gelatine mixture and stirred at the same temperature, until the emulsion had an opaque white colour and the oil particles were fully dissolved. We kept stirring the mixture until the temperature dropped to 50°C, when we added the surfactant. Finally, when the prepared mixture reached 35°C, we poured it into the mould (170 × 130 mm), and let it set overnight before we conducted any measurements.

Table 3.1 presents the concentrations of the materials used for the phantoms mimicking different brain tissues used in our experiments. We fabricated four tissue-mimicking phantoms, using as reference the properties reported in [64]. The in-vivo measurements in [77] reported that properties of an ischaemic vessel in the brain can vary from -10% up to -25% relative to the dielectric properties of healthy brain tissue at 1 GHz. As this was the first study that validated experimentally a MWT algorithm for ischemic stroke in a wide frequency range, we chose to prepare ischaemic phantoms with the maximum reported difference of -25% relative to the properties of the brain phantom. We point out that a smaller contrast between the ischemic target and the brain is challenging and would require a robust algorithm. Further validation to assess which is the smaller difference that a MWT algorithm can detect successfully is needed, however this was outside of the scope of this study.

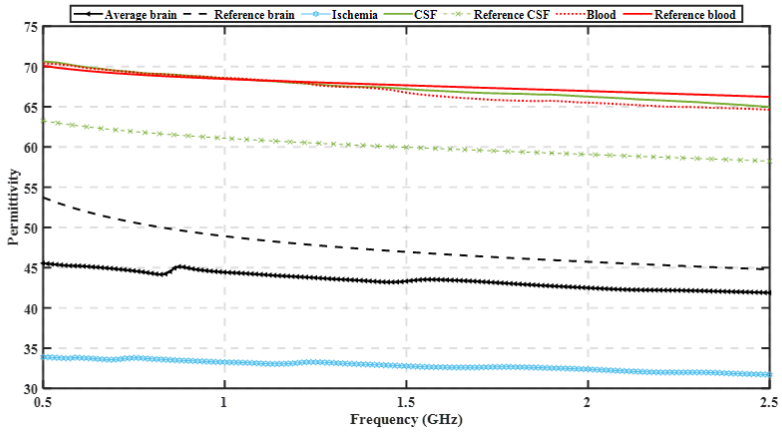

(a) Measured permittivity of the prepared tissue mimicking phantoms relative to their reference values.

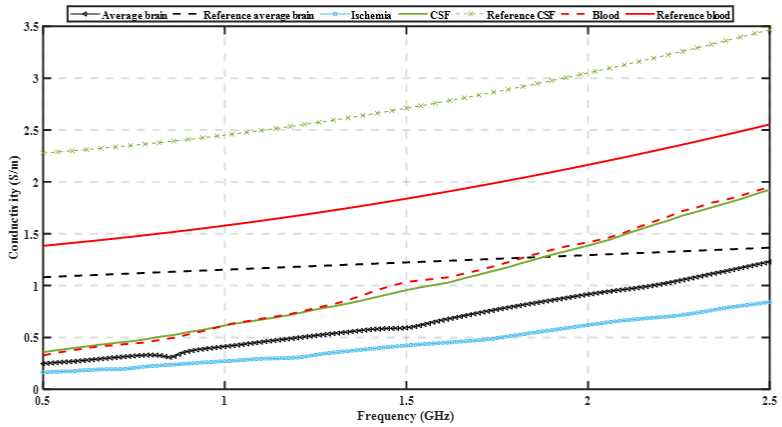

(b) Measured conductivity of the prepared tissue mimicking phantoms relative to their reference values.

Figure 3.2: Dielectric properties of the fabricated tissue mimicking phantoms relative to reference values taken from [65] (to the authors' knowledge, there is no literature regarding the dielectric properties of ischaemia in a wide frequency range). Same type of tissues are presented with the same colour.

For the experimental testbeds it is assumed that, due to similar dielectric properties of CSF and blood, the same gelatine mixture can be used to mimic the two different tissues. Fig. 3.2 presents the measured dielectric properties of the prepared phantoms

for brain, CSF, blood and ischaemia, respectively. The measurements were conducted using Keysight's dielectric spectroscopy kit, over a 0.5–2.5 GHz frequency range at different points of the phantoms. The plots in Fig. 3.2 show very good agreement with reference data for the dielectric constant, but quite lower conductivity values for our phantoms. Specifically for the average brain and CSF phantom, the measurements values differ from the reference data at a scale of 10-15%, but for the purpose of this experiment this is acceptable as the dielectric difference between the average brain and the two types of the stroke is within limits. Furthermore, as MWT relies mostly on contrast in dielectric constant, the discrepancies in conductivity are not critical for this initial investigation.

Table 3.1: Concentrations of materials used for 100 ml of tissue mimicking phantoms.

Phantom type	**Water**	**Powder**	**Kerosene**	**Oil**	**Propanol**	**Surfactant**
Average brain	60 ml	11 gr	13 gr	13 gr	2.5 ml	1.5 ml
CSF/Blood	80 ml	16 gr	-	-	4 ml	-
Ischemia	50 ml	8.5 gr	20 gr	20 gr	1.5 ml	1.5 ml

After preparation, phantoms were placed in elliptical plastic acrylonitrile butadiene styrene (ABS) moulds which aim to mimic the brain's shape and multi-layer structure, as shown in Fig. 3.3. We first poured the CSF phantom in the outer layer of 5 mm thickness. After this was solidified, we extracted the inner mould and filled the remaining cavity with the brain phantom. For a one-layer model without the CSF, we simply extracted the inner mould and poured the phantom in the outer mould directly. We used an additional cylindrical mould to create a hole (diameter = 30 mm) in the phantom, which can be filled with the phantom mimicking either blood or ischaemia, emulating the two cases of brain stroke termed as h-stroke for hemorrhagic and i-stroke for ischaemic, respectively.

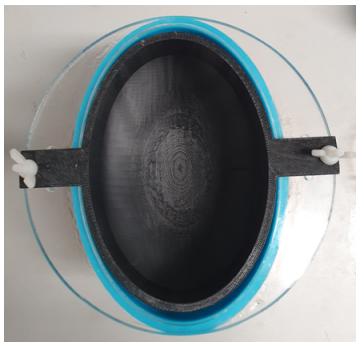

(a)

(b)

(c)

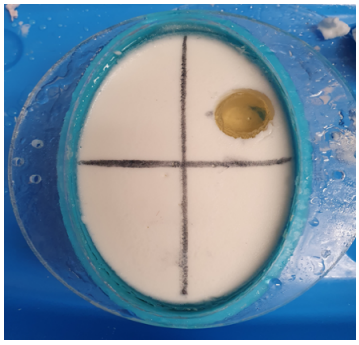

(d)

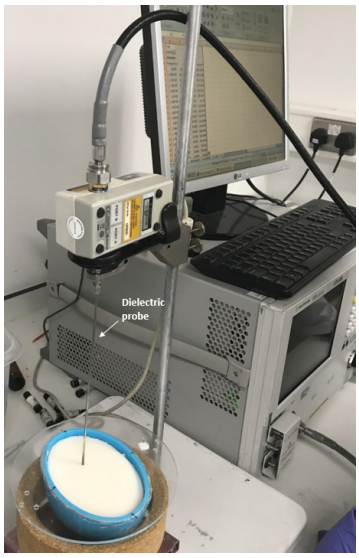

(e)

Figure 3.3: Summary of the head model construction: **(a)** Elliptical 3-D printed mould to form the CSF and average brain layers; **(b)** The two-layer model after CSF and average brain phantoms are poured into the moulds (the CSF is a thin, transparent layer just inside the blue mould); **(c)** Creating a hole in the phantom to insert the cylindrical blood-mimicking target; **(d)** Final two-layer phantom with a target of blood-mimicking phantom; **(e)** Setup with Keysight's slim form probe to measure the dielectric properties of the phantoms.

To further investigate the changes in the dielectric properties over time, we prepared two additional brain phantoms and measured their real and imaginary part of

permittivity on day 1 and day 6 after their preparation. Table 3.2 shows that, over a period of 6 days, the dielectric properties increased 10–15% compared to their initial values. This was expected as the water particles have dispersed over time resulting in higher dielectric properties. Consequently, the phantoms are not reusable, as they maintain their dielectric properties for a short period of time and can be used for experiments that will take place on day 1. However, the variation of phantoms' dielectric properties over time is beneficial for cases in which a small variation is needed for further evaluation of the algorithm, for example, the cases examined in Section 3.3.3.

Table 3.2: Dielectric properties of brain phantoms over time at 1 GHz.

Measured property	**Day 1**	**Day 6**
ϵ' sample 1	44.5	51.2
ϵ' sample 2	46.2	51.6
ϵ'' sample 1	0.43	0.51
ϵ'' sample 2	0.42	0.48

3.2.2 Setup and Data Acquisition Process

Figure 3.5b presents the experimental setup, which was used for conducting the measurements. It consists of a 300 mm diameter cylindrical tank surrounded by an absorber (ECCOSORB MCS) and enclosed with a metallic shield to decrease surface waves propagating into the perimeter of the tank. The tank was filled with a 90% glycerol-water mixture to improve impedance matching with the phantom and widen the antenna operating frequency range [148]. An eight-antenna elliptical array was immersed inside the tank, and the length of the ellipsoid's axes was 153 mm and 112 mm. From a theoretical point of view, in the 2-D scalar case, the choice of the number of antennas is defined as:

$$M = 2\beta\alpha \tag{3.1}$$

where α is the radius of the reconstruction domain and β is the wave-number [155]. Taking into account our first working frequency of 0.5 GHz, M is approximately equal to 15. However, due to the increase of antenna coupling and space constraints as well as, our previous experimental work which has shown good results using eight antennas in our MWT prototype, we chose eight antennas to simplify the experiment and the data acquisition process [148]. However, the feasibility study [56], recommended that the optimal number of antennas in a MWI prototype is 24. Nevertheless, the work at [156] presented promising results using a MWT prototype with 24 dipole antennas.

The experiments presented in this study use spear-shaped patch monopole antennas which operate efficiently in the range of 0.5–2.0 GHz [157] and their design is shown in Fig. 3.4. This range satisfies the recommendation by the theoretical approach in [56], which suggests that a working frequency up to 1.5 GHz can achieve the optimal trade-off between the required resolution and incident power needed for head imaging applications. The spear-shaped antennas were installed through vertical and horizontal rulers that enabled us to adjust their height and the array dimensions.

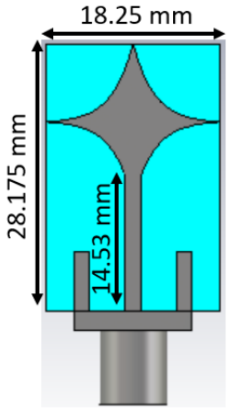

Figure 3.4: The spear-shaped antenna used in our experiments and its dimensions [131],[156].

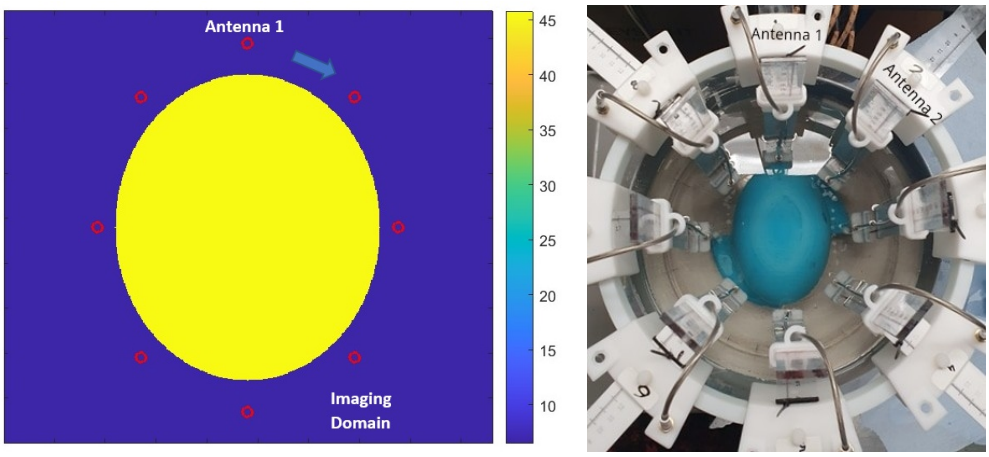

Figure 3.5: **(a)** Schematic of the simplified "initial guess" model for the inversion (the ellipsoid's axes are 153 mm and 112 mm long); **(b)** The hardware system prototype.

Phantoms were placed at the bottom of the tank, and measurements of the S-parameters of the scattered signals were conducted in a frequency range of 0.5–2.5 GHz using an eight-port vector VNA from Keysight. The eight spear-shaped antennas acted both as transmitters and receivers, creating an 8×8 scattering matrix which was fed into DBIM-TwIST. The linear integral equation was discretized iteratively for the entire 8x8 transmit-receive pairs. Overall, two sets of measurements were performed for every imaging scenario. The first set of measurements was performed for the phantom without a target (NT scenario), and then the process was repeated for the phantom which included the 30 mm diameter h-stroke or i-stroke target (WT scenario). The target was placed either in the upper-right or the upper-left section of the phantom between antennas 1 and 8 or between antennas 1 and 2. These locations were selected to ensure the algorithm's efficiency and to validate successfully that it can reconstruct targets in multiple locations, as well as it does not reconstruct a ghost target in the middle of the area of interest. Following this process, the S-parameters for NT and WT scenarios were processed by the DBIM-TwIST algorithm [84].

3.2.3 Simulation model

The presented system and model were first simulated using CST Microwave Studio to assess the performance of DBIM-TwIST prior the experiments. Fig 3.6 presents the simulated prototype that is composed of a tank with a diameter of 300 mm and filled with 90% glycerol-water mixture. Within the tank we placed an ellipsoid with the shape of our experimental phantom, filled with the dielectric properties of average brain tissue assigned from the CST's library. The list of the dispersive dielectric properties is shown at Table 3.3. The phantom was surrounded by 8 spear-shaped antennas [157] in an elliptical arrangement with the same dimensions as the experimental setup. A cylindrical target (diameter d = 30 mm and height h = 30 mm), which simulates either the hemorrhagic or the ischemic stroke, was placed at the same position as the experiment for each scenario. For this examined scenario we conducted four simulations to acquire the scattered field data: one without the target (NT), one with hemorrhagic (h-stroke), one with ischemic (25% i-stroke) stroke and one where the target had 50% lower dielectric constant than the average brain phantom (50% i-stroke).

Table 3.3: Debye parameters of the examined tissues. The Debye parameters of the average brain and of the h-stroke have been assigned by curve fitting from CST data. Debye parameters of the 90% glycerol water and of the i-stroke have been obtained from the experimental dielectric measurements.

Material type	ϵ_∞	$\Delta\epsilon$	σ_s
90% glycerol water	6.56	16.86	0.3232
Average brain	45.8	0.1244	0.7595
H-stroke	59.23	6.142	1.374
I-stroke	25	10	0.01

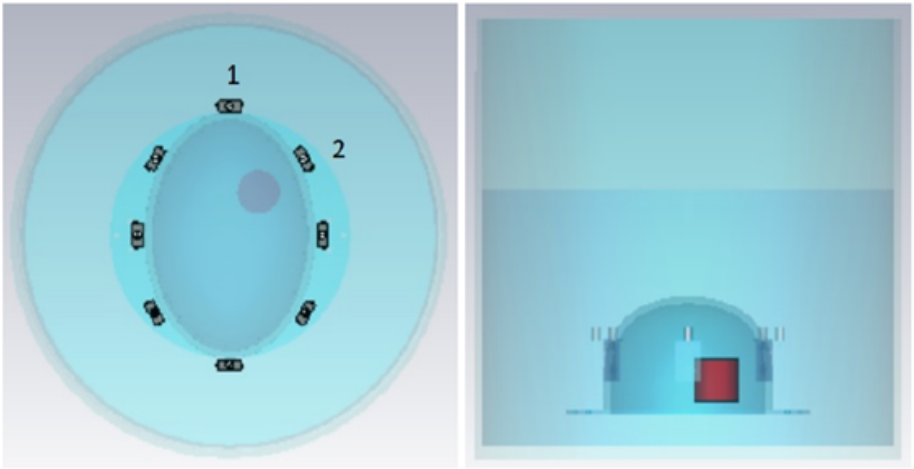

Figure 3.6: The simulation system prototype in CST, which uses an ellipsoid head phantom. The ellipsoid's dimensions are approximately 170 × 130.

3.2.4 Implementation of the DBIM-TwIST Algorithm

To reconstruct the dielectric properties of the phantoms, we have applied our formerly developed DBIM-TwIST algorithm which has been presented in detail in our Background chapter. The background properties of the forward model are updated at each DBIM iteration with the current solution until the residual error is minimised. The algorithm solves the linear problem with the TwIST method [145], which splits the matrix into a two-step iterative equation. The background properties are calculated and updated at each DBIM iteration with the TwIST solution until the residual error is minimised, and this yields the reconstruction of the dielectric properties of the imaging domain.

In a realistic scenario we will not know the exact dielectric properties of the head, but its dimensions can be available with ad hoc measurements. As it was shown in [84], it is possible to successfully reconstruct an image by knowing only the shape of the model. Therefore, the initial model ("starting guess") for the algorithm which is shown in Figure 3.5a, consists of a simplified 2-D representation of the experimental setup, which includes the tank filled with 90% glycerol-water mixture and an ellipsoid

(153 × 112 mm) that mimics the average brain tissue, whose Debye parameters are shown at Table 3.3. The dimensions of the ellipsoid represent the actual size of the phantom's axial slice at the height where the antennas were located. The algorithm simplifies the system's spear-shaped antennas with line sources, which are placed at the same locations as the experiment. The reconstruction domain contains only the brain ellipsoid inside the antenna array. The evaluation of the impact of prior information that is needed for the forward model is explored further in the next chapter.

To calibrate the simulated initial model, we used a NT reference measurement [149]. The experimental data will include some noise from the coupling from cable movement, environmental noise, and machine noise. To lessen the impact of the measurement error, a denoising technique must be applied to the experimental data. Furthermore, we should calibrate the measured and simulated data due to the disparity between the simulations in the MWT algorithm and the realistic experimental measurements. Also, we should apply a calibration method to minimise the difference between the FDTD forward data and the data from the experimental measurement or the realistic CST model, as our forward model uses point sources as antennas. This calibration method relies on the signal difference between the experimental and the forward NT scenarios, to calibrate the signals received from the WT experiment. The difference between the data obtained by running FDTD forward solver for an empty tank and the no-target experiment or simulated scenario is calculated and then we can calculate the calibrated data by adding this difference to the simulation or experimental WT measurement.

We note that an exact NT reference measurement will not be available in a realistic clinical scenario such as stroke detection. Aside from an "empty tank" measurement which could always be used as a reference, one could also use a reference signal measured from an "average homogeneous head phantom" taken from a set of phantoms with different properties, following the approach used for imaging numerical breast phantoms in [84], for example. This approach, however, would still provide the algorithm with very different signals from the true NT signals in stroke detection, as the brain structure is much more complex than any "homogeneous average brain" phan-

tom, and a more complex, inhomogeneous reference phantom may be better suited for data calibration. We also note that our DBIM-TwIST approach has been shown to be capable of reconstructing accurately complex inhomogeneities using simulation data from complex numerical breast phantoms [84], but the problem of detecting the stroke inside the complex yet unknown brain structure may be more challenging. We partially examine this issue in Section 3.3, by using a NT scenario from a "day 1 phantom" and a target scenario from a "day 6 phantom" with almost 20% higher dielectric properties.

As mentioned in the Background chapter, to take into account the materials' dispersive dielectric properties, we have employed a first-order Debye model for the average brain phantom and the 90% glycerol-water mixture:

$$\epsilon_s(\omega) = \epsilon_\infty + \frac{\Delta\epsilon}{1 + j\omega\tau} + j\frac{\sigma_s}{\omega\epsilon_0} \tag{3.2}$$

where ϵ_∞, $\Delta\epsilon$ and σ_s are the parameters of the single pole Debye model provided in Table 3.4. We have used the parameters of Table 3.4 together with a forward solver based on the FDTD method to calculate the scattered and background fields, and then applied DBIM-TwIST to reconstruct the dielectric properties inside the imaging domain with a grid voxel size of 2 mm. The complex permittivity values are replaced by the frequency-dependent Debye model of Equation (3.2) and are updated at each DBIM iteration, thus are used to update the contrast function. The reconstructed results present estimated real and imaginary parts of permittivity which are calculated from the updated Debye models at each frequency [12]. Moreover, we have performed the same number of 15 DBIM-TwIST iterations at each frequency for both single and multiple frequency reconstructions attempted in this study. The running time for each DBIM iteration was approximately 8 seconds using Matlab R2019b run on an Intel i7 processor with 16 GB RAM memory, leading to an execution time of 2.5 minutes for 15 iterations of DBIM at each frequency. By means of an example, the total execution time for the case of the h-stroke with one layer and MWIFH between 0.5 and 1.5 GHz and while using Matlab, was 24 minutes. We note that this is the worst-case scenario as in a realistic prototype the execution time will be significantly less with the use of

micro-controllers and field-programmable gate arrays (FPGAs).

Table 3.4: Debye parameters of materials after curve fitting to measured dielectric properties.

Material type	ϵ_∞	$\Delta\epsilon$	σ_s
90% glycerol-water	6.56	16.86	0.3232
Average brain	30	10	0.147

3.3 Reconstructed Results

First, we have assessed numerically the performance of DBIM-TwIST by replicating the experimental scenario on CST. Then, in the first set of experiments, our aim is to show our method's potential to determine the type of stroke from estimating its dielectric properties. To this end, we have examined two phantoms of average brain tissue in which we inserted a target emulating h- and i-stroke, respectively. In the second set of experiments, our aim is to test detection performance in cases where the inverse experimental model is slightly different compared to our forward model. To this end, we have examined two additional phantoms with h-stroke targets. The first one is a two-layer phantom including a thin CSF-mimicking layer, and the second one is a brain phantom which we let set for 6 days before conducting the WT measurements so that its properties are different in comparison with the first day when the NT measurements were taken.

3.3.1 Initial Numerical Results

Figs. 3.7 - 3.9 present the reconstructed real and imaginary parts of the complex permittivity for the phantom inside the prototype of Fig. 3.6 containing h-stroke and i-stroke targets as well as a target which has 50% lower dielectric constant than the average brain phantom as an extreme case (50% i-stroke). Single-frequency reconstruc-

tions in the range 0.7–1.5 GHz are presented in Figs. 3.7 and 3.8, while results from the MWIFH approach are shown in Fig. 3.9.

These results reveal that we can successfully detect the target within the area of interest for the real part of permittivity of the examined cases by using DBIM-TwIST, but we cannot detect the targets for the imaginary part of permittivity. However, there is a direct distinction in the estimation of the dielectric properties for all the three targets when reconstructing the real part of permittivity. Moreover, the reconstruction results show further improvement when using the MWIFH approach which supports the initial results presented at [131] and [132]. Namely, for the single frequency results of Fig. 3.7 the estimated value of real permittivity ϵ' at 1.2 GHz is 44.87, 21.04 and 18.914 for for h-stroke, 25% i-stroke and 50% i-stroke, respectively. MWIFH results of Fig. 3.9 estimate the value of real permittivity ϵ' at 1.5 GHz as ϵ'=44.38, ϵ'=32.44 and ϵ'=28.12 for for h-stroke, 25% i-stroke and 50% i-stroke, respectively. The real permittivity of h-stroke, 25% i-stroke and 50% i-stroke in the simulation model within the frequency range of 0.7-1.5 GHz, is roughly 65, 33 and 22 respectively, which shows that the reconstructed permittivity of the targets is acceptable estimation of the real target values.

3.3.2 Detection and Classification of Stroke Targets

Figs. 3.10 - 3.12 present the reconstructed real and imaginary parts of the complex permittivity for the phantom inside the prototype of Fig. 3.5b containing h-stroke and i-stroke targets as well as a target which has 50% lower dielectric constant than the average brain phantom as an extreme case. Images illustrate the whole tank, however, the reconstruction domain contains only the brain ellipsoid inside the antenna array. Representative single-frequency reconstructions in the range 0.7–1.5 GHz are shown in Figs. 3.10 and 3.11, while results from MWIFH approach in the same range are shown in Fig. 3.12. These images suggest that the dielectric constant (real part) of 25% i-stroke is detectable at low frequencies albeit with more artifacts in the images, whilst the h-

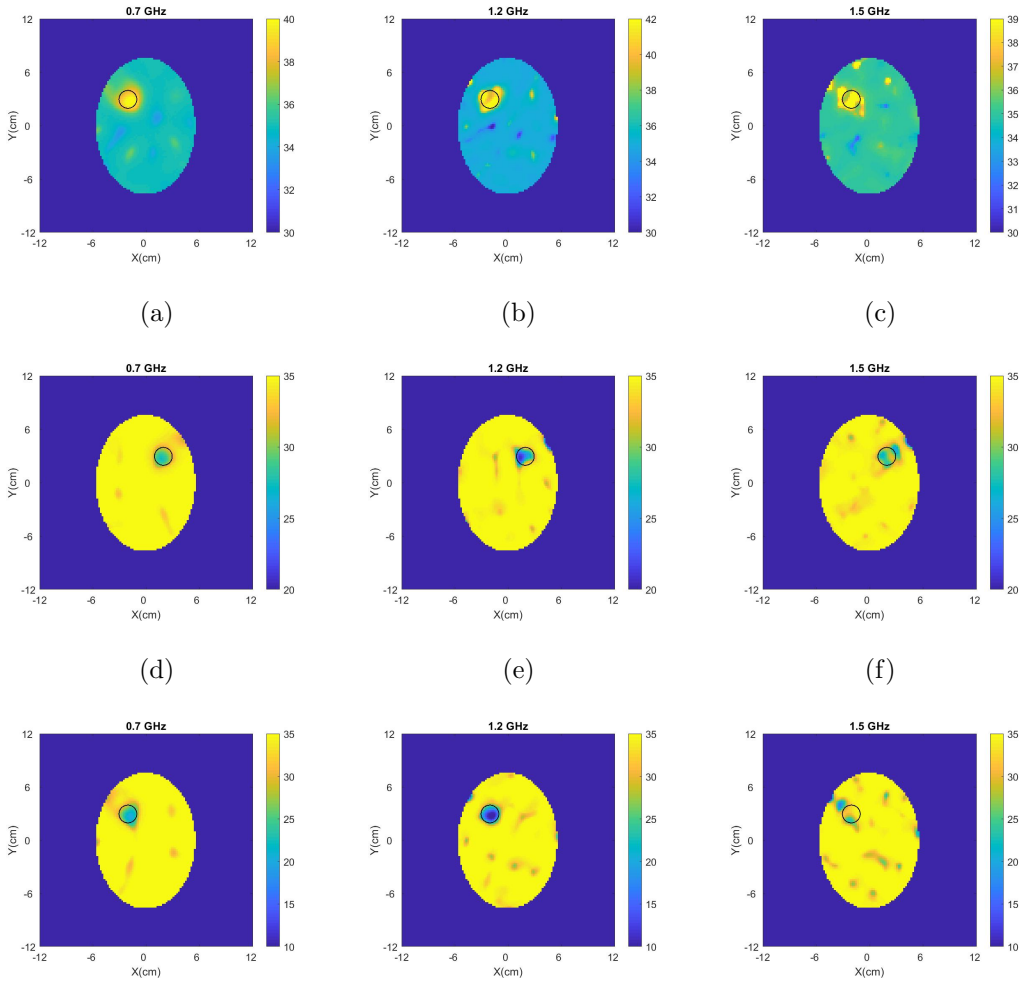

Figure 3.7: Simulation results from single frequency reconstructions of the real part of the complex permittivity for: **(a–c)** h-stroke, **(d–f)** 25% i-stroke and **(g–i)** 50% i-stroke.

stroke and the 50% i-stroke, is clearly visible in frequencies above 1.1 GHz for both real and imaginary parts. As the dielectric contrast between the constructed 25% i-stroke and brain phantoms is lower than that of h-stroke and 50% i-stroke, detecting the 25% i-stroke target is more challenging than the other cases, with unsuccessful results for the imaginary part of the complex permittivity. The most encouraging observation from these figures, however, is that there is a clear distinction in the estimation of

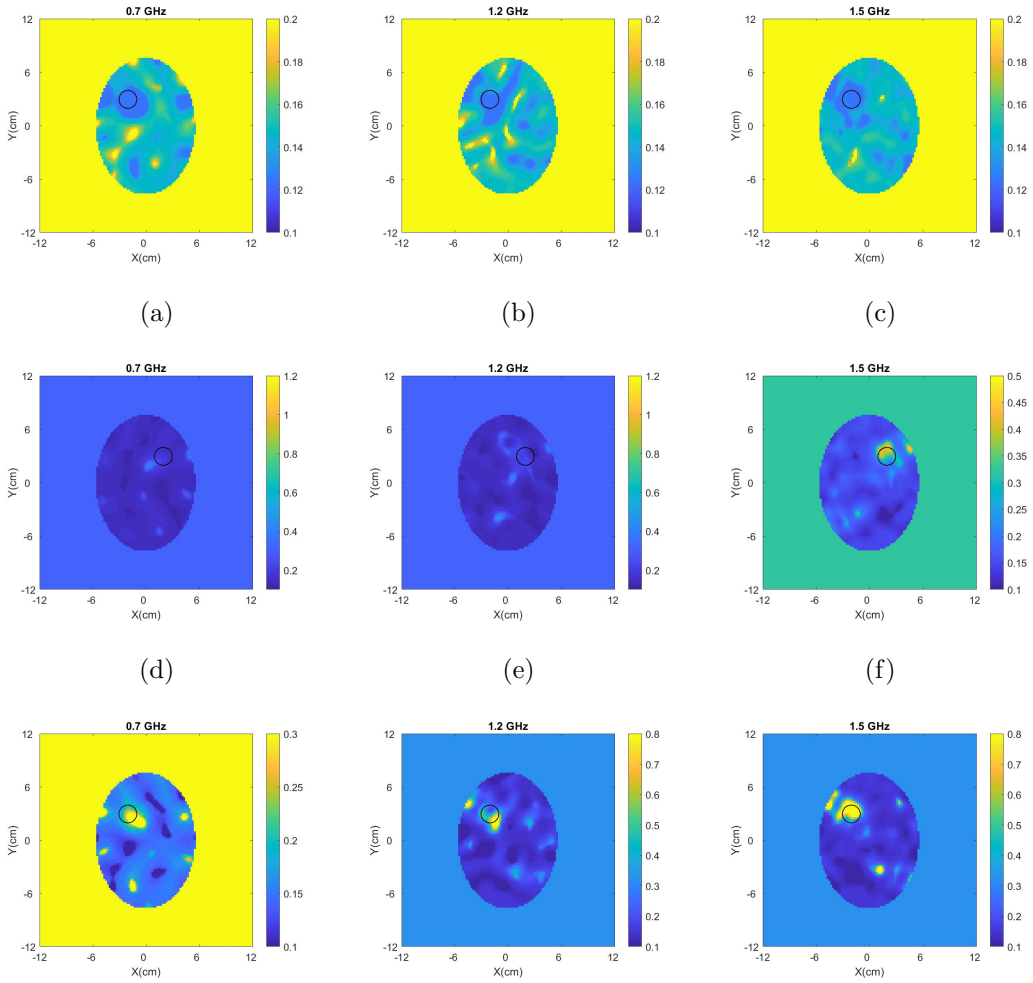

Figure 3.8: Simulation results from single frequency reconstructions of the imaginary part of the complex permittivity for: **(a–c)** h-stroke, **(d–f)** 25% i-stroke and **(g–i)** 50% i-stroke.

the dielectric properties for all the three targets as well as, clear improvement when using MWIFH: the MWIFH results of Fig. 3.12 estimate the value of real permittivity ϵ' at 1.5 GHz as ϵ'=33.8, ϵ'=20.9 and ϵ'=56.25 for 25% i-stroke, 50% i-stroke and h-stroke, respectively. The real permittivity of h-stroke, 25% i-stroke and 50% i-stroke in the experimental model within the frequency range of 0.7-1.5 GHz, is roughly 67, 33 and 22 respectively, which shows that the reconstructed permittivity of the targets

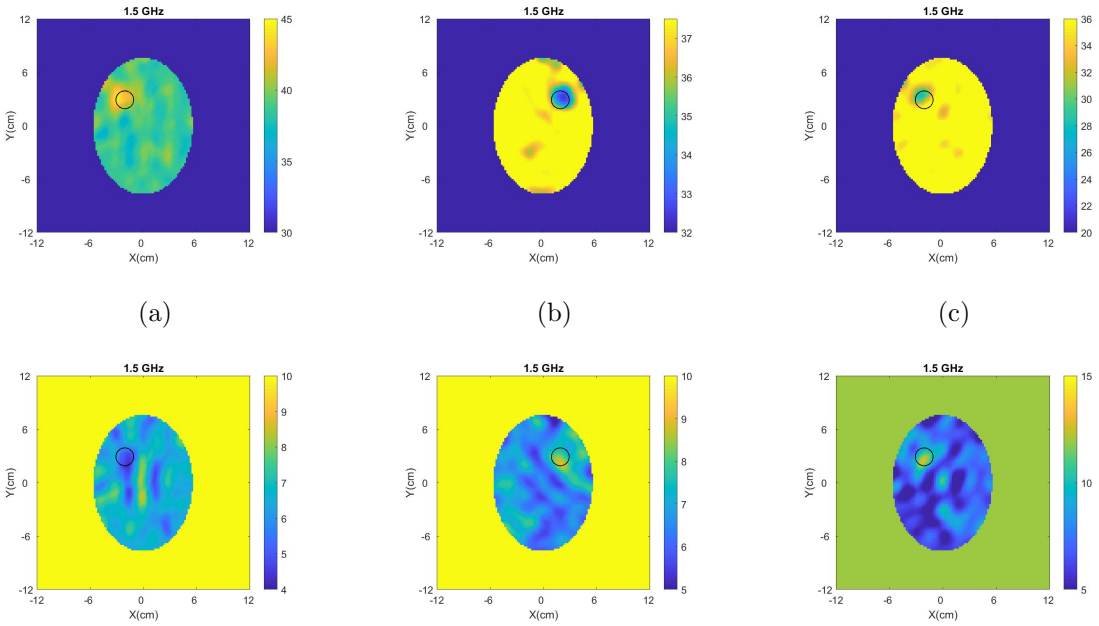

Figure 3.9: Reconstructed: **(a–c)** real and, **(d–f)** imaginary part of the complex permittivity for simulation h-stroke (left), simulation 25% i-stroke (middle) and simulation 50% i-stroke (right). The complex permittivity was calculated at 1.5 GHz using MWIFH approach in a frequency range of 0.7–1.5 GHz.

is acceptable estimation of the real target values.

3.3.3 Stroke Target Detection for Brain Phantoms with Unknown Properties

To move towards more realistic imaging scenarios where the brain's distribution of tissues will be more complex and their dielectric properties unknown, we have evaluated experimentally the robustness of DBIM-TwIST when the structure and dielectric properties of the brain phantom are slightly different from the "initial guess" of Fig. 3.5a.

To examine the effect of differences in the dielectric properties of the average brain phantom where the target is inserted, we prepared a phantom and conducted NT mea-

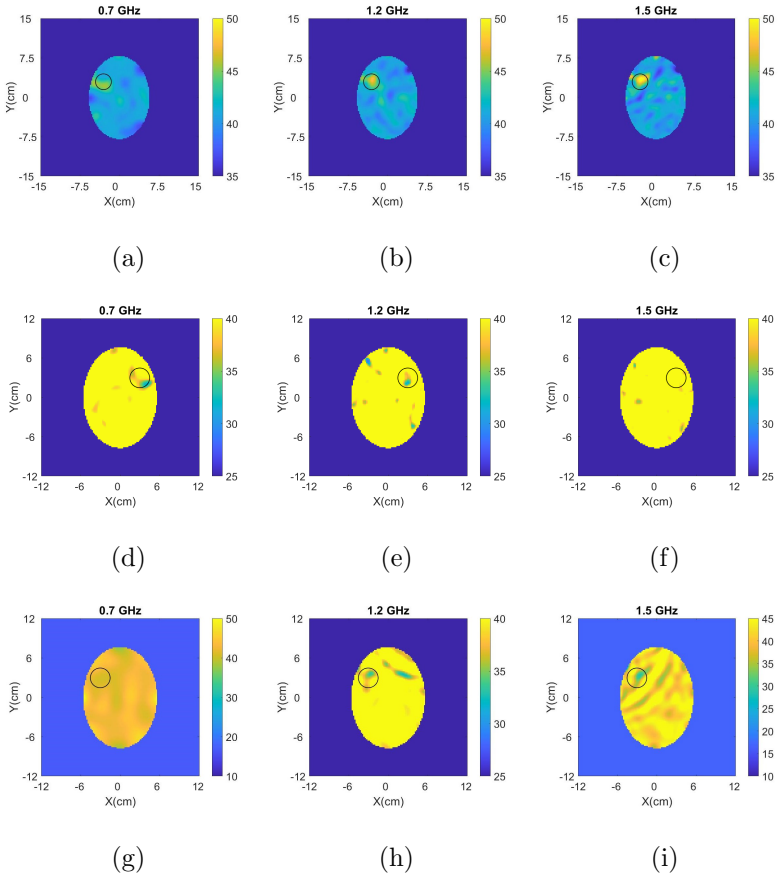

Figure 3.10: Results from single frequency reconstructions of the real part of the complex permittivity for: **(a–c)** h-stroke, **(d–f)** 25% i-stroke and **(g–i)** 50% i-stroke.

surements after the phantom had set, and then kept it for a week, in which we recorded the change of its dielectric properties over time. We then acquired WT measurements for h-stroke on day 6, to ensure a change in the phantom's dielectric properties from the NT measurements on day 1. In addition to this test, we also performed experiments with a two-layer phantom (CSF and average brain). To this end, we added a CSF layer of 5 mm thickness using the process described in Fig. 3.3, and with dielectric properties plotted in Fig. 3.2.

Fig. 3.13 presents the reconstructed images of the real and imaginary parts of complex permittivity using the data obtained by the measurements at days 1 and 6 after the preparation of the brain phantom, as well as the reconstructed images of the two-layer

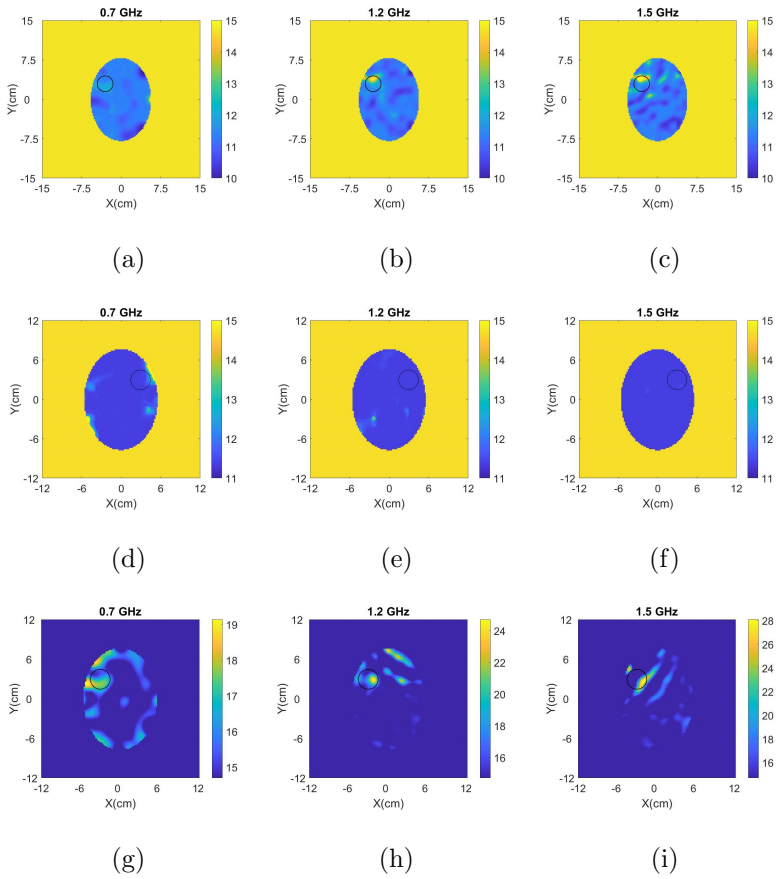

Figure 3.11: Results from single frequency reconstructions of the imaginary part of the complex permittivity for: **(a–c)** h-stroke, **(d–f)** 25% i-stroke and **(g–i)** 50% i-stroke.

phantom including the CSF layer. These reconstructions were produced by MWIFH in the range of 1.1–2.0 GHz. The values of the reconstructed real and imaginary parts for the h-stroke target at 2 GHz are $\epsilon' = 49.28$, $\epsilon'' = 12.19$ for the one-layer phantom, and $\epsilon' = 62.38$, $\epsilon'' = 8.48$ for the two-layer phantom, respectively. As in the previous cases, the real permittivity of h-stroke, in the experimental model, is roughly 67 at 2 GHz. With the exception of the imaginary part for the two-layer phantom, these images provide a clear indication of where the h-stroke is located and estimate its dielectric constant with satisfactory accuracy. These reconstructions confirm that the algorithm is sufficiently robust to detect and localize the target successfully in cases with "mild" uncertainties in the true background medium in the experiment and its "initial guess"

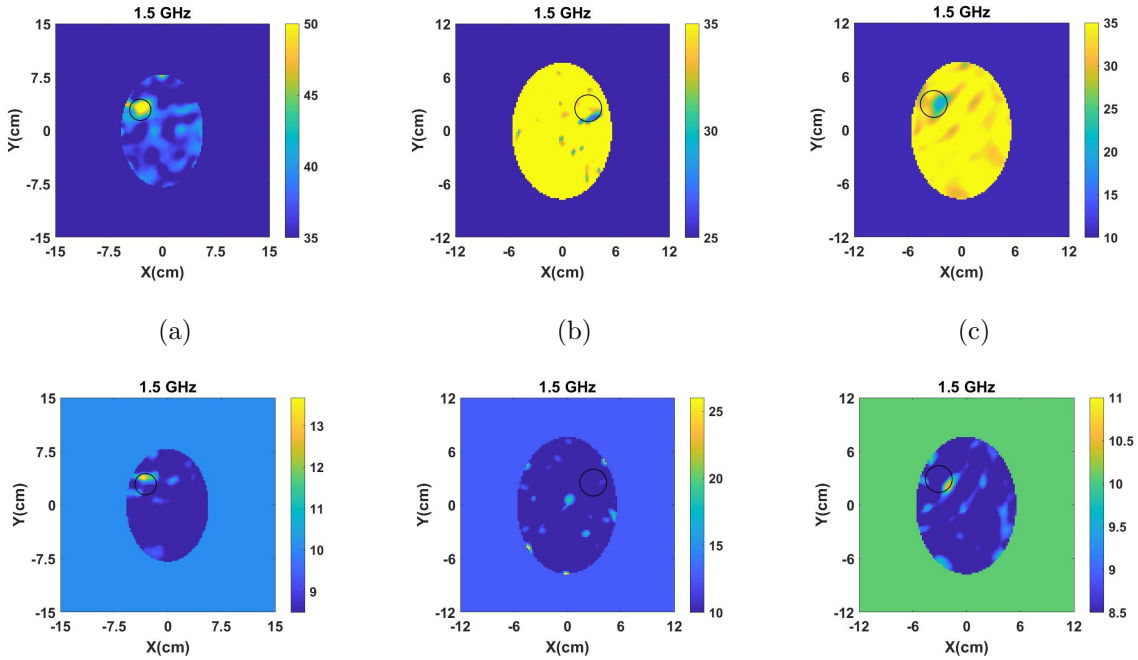

Figure 3.12: Reconstructed: **(a–c)** real and, **(d–f)** imaginary part of the complex permittivity for h-stroke (left), 25% i-stroke (middle) and 50% i-stroke (right). The complex permittivity was calculated at 1.5 GHz using MWIFH approach in a frequency range of 0.7–1.5 GHz.

in the imaging algorithm.

3.4 Reconstructed Results Using an Anthropomorphic Brain Phantom

This section presents the reconstruction results using a 3-D-printed anthropomorphic head model. To perform the measurements, the head model was immersed inside our imaging tank and the image reconstructions have been obtained through the 2-D DBIM-TwIST algorithm.

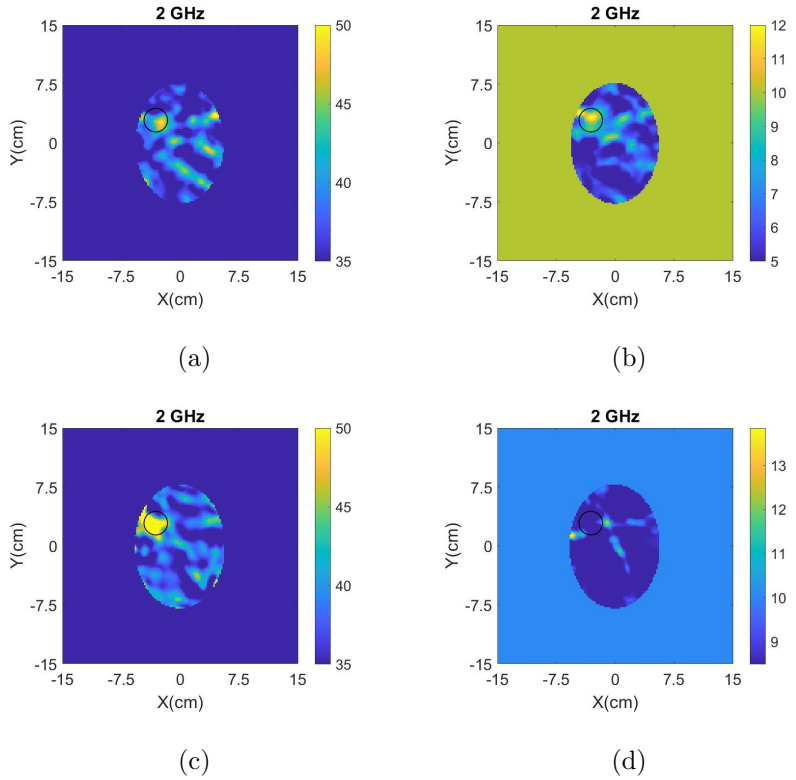

Figure 3.13: **(a)** Reconstructed real and **(b)** imaginary part of the complex permittivity for the phantom inside the tank of Figure 3.5b, when NT and "h-stroke target" measurements were conducted at day 1 and day 6 after the preparation of phantom, respectively. **(c)** Reconstructed real and **(d)** imaginary part of the complex permittivity for a two-layer phantom with an "h-stroke target" and a CSF layer which is unknown to the imaging algorithm. The complex permittivity was calculated at 2 GHz using MWIFH approach in 1.1–2 GHz.

3.4.1 Experimental Configuration

The setup included the same cylindrical tank that was presented in Subsection 3.2.2. The transmitter and receiver spear-shaped antennas were placed in an elliptical ring inside the acrylic tank and were connected to the multiport Keysight M9019A Vector Network Analyzer (Fig. 3.14). We prepared gelatin-oil mixtures derived from the phantom preparation technique which has been fully analyzed in Section 3.2. Overall,

we prepared mixtures for average brain and blood. Tables 3.5 and 3.6 show the concentrations of materials used for each solution and their measured dielectric properties (at 1 GHz), respectively.

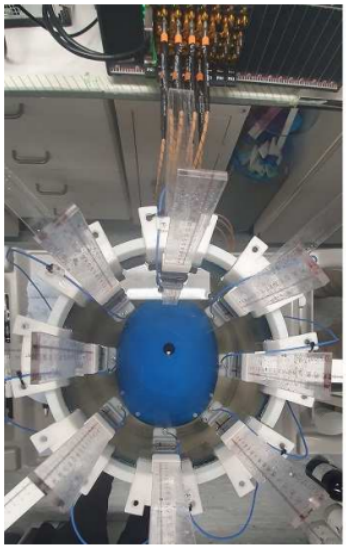

Figure 3.14: Measurement hardware and setup.

Table 3.5: Quantities of materials used for 100 ml of human tissue mimicking phantoms.

	Average brain	**Blood**
Water	60 ml	80 ml
Gelatin powder	11 gr	16 gr
Kerosene	13 ml	-
Safflower oil	13 ml	-
Propanol	2.5 ml	1.5 ml
Surfactant	4 ml	-

After preparation, the average brain solution was poured into a 3-D printed anthropomorphic head mould of Fig. 3.15 (a), by slowly pouring it inside, through the hole on the top of the mould. We conducted two sets of measurements, one with one layer of average brain (NT case) and one with an additional target with blood's dielectric properties (WT case). To place the target, after performing the NT measurements we created a slice in the upper part of the mould, by using a thin string and detaching

Table 3.6: Dielectric properties of tissue mimicking phantoms at 1 GHz.

	ϵ'	ϵ''
Average brain	41.1	0.35
Blood	62.3	0.56

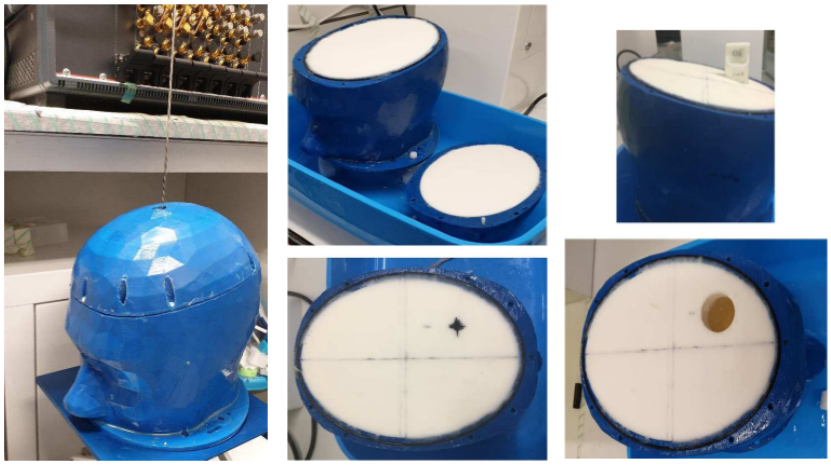

(a) (b) (c)

Figure 3.15: Anthropomorphic head model and the preparation stages of the phantom layers.

this part (Fig. 3.15 (b)). Then we used a cylindrical mould to extract a part of the brain and create a cylindrical cavity (diameter = 30 mm) which was filled with the blood target mixture. The target was eccentrically placed 40 mm horizontally and 25 mm vertically from the center of the phantom (Fig. 3.15 (c)). Lastly, the upper head section was re-attached, and WT measurements were performed.

3.4.2 Reconstructed Results

Figs. 3.16 (a), (b) and (c) depict the reconstructed real permittivity for the head model, for three different single frequencies of 0.7, 0.9 and 1.2 GHz, respectively. The dimensions of the reconstruction domain is 202 $\times$ 158 mm for the plastic layer and 170 $\times$ 127 mm for the average brain layer. This corresponds to the dimensions of

the phantom's axial slice at the height where the spear-shaped antennas are placed. These results show that DBIM-TwIST is capable of detecting the blood mimicking target in its approximate position when we use a more realistic phantom, through the subtraction between the head with and without the target.

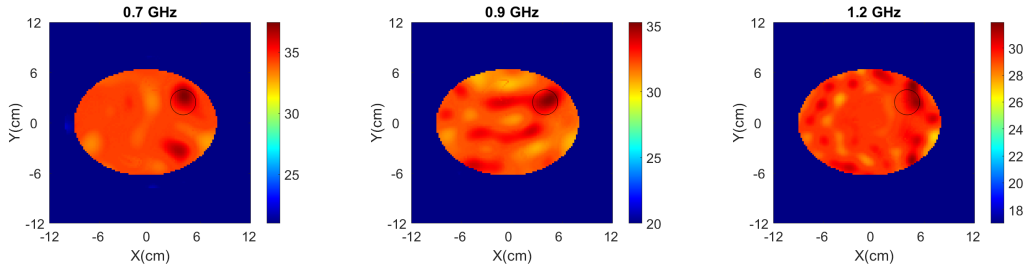

(a) (b) (c)

Figure 3.16: Single frequency reconstructions of the real permittivity for (a) 0.7, (b) 0.9, and (c) 1.2 GHz.

3.5 Fabrication and Dielectric Measurements of a Solid Matching Medium for Microwave Imaging Systems

As mentioned in the Introduction, secondments in beneficiaries of the EMERALD network have been a major part of the project. The second secondment took place in Keysight, Austria from November 2019 to December 2019. The initial objective of this secondment was to understand how the measurement setup affects the data acquisition process and quality. Therefore, at the beginning, work was focused on understanding how the VNA calibration works, data structures and how errors are calculated using Ecal and Keysight's calibration algorithms.

(a) (b) (c)

Figure 3.17: Dielectric probe measurements: (a) Performance probe, (b) Slim probe, (c) High-temperature probe.

An additional task of this secondment was the fabrication and dielectric measurements of high-permittivity materials that could be used to reduce the signal loss due to mismatches of the head's different layers. To this end, mixtures of polydimethylsiloxane (PDMS) with ceramic powders (ZnO or $BaTiO_3$) were prepared. First PDMS was mixed with the ceramic powder using a driller until the mixture was homogeneous, and then the mixture was placed in a vacuum chamber for the degassing step. The samples were placed into a heating plate for the setting phase and the dielectric measurements were conducted with three different probes: performance, slim and high-temperature, respectively (Fig. 3.17) on the next day. Fig. 3.18 shows the permittivity measurements for different concentrations and types of PDMS - ceramic powder mixtures. It is noticed that the addition of ceramic powder increases the permittivity of the PDMS but not to the level that would be useful for MWI applications. Moreover, it was observed that a higher percentage of ceramic powder increases the elasticity of the PDMS samples. The work that was initiated in this secondment was further examined by the group in Keysight and experimental results were presented in the joint paper published

in the special issue of Diagnostics [53].

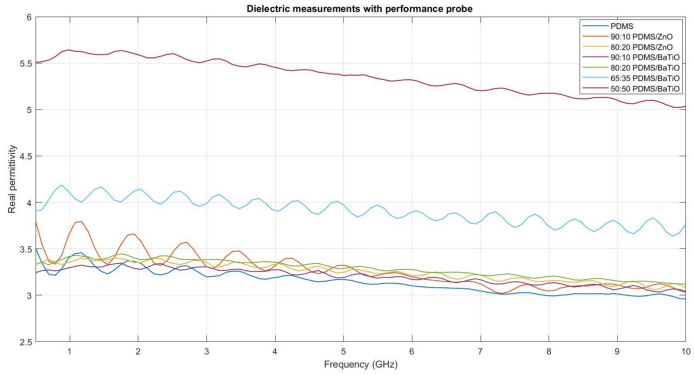

(a)

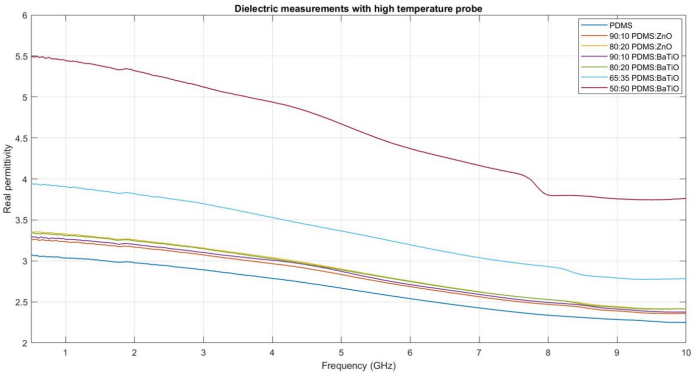

(b)

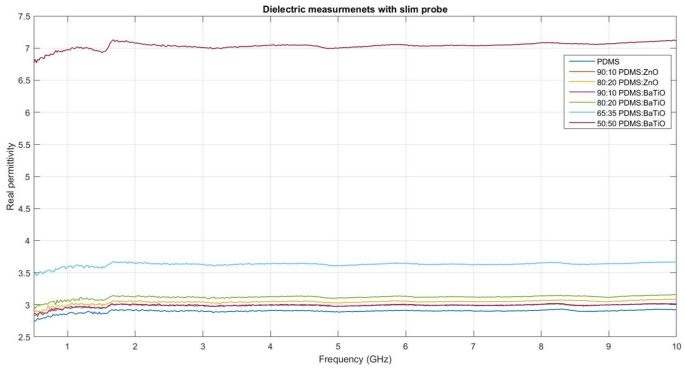

(c)

Figure 3.18: Permittivity measurements for 7 samples.

3.6 Conclusion

In this chapter, we have presented an initial experimental assessment of a microwave tomography prototype based on the DBIM-TwIST algorithm for brain stroke detection and classification. This MWT system was able to differentiate the real permittivity between targets that mimic hemorrhagic and ischaemic stroke, based on the difference in their estimated dielectric properties. However, it wasn't able to successfully detect and differentiate the imaginary part of permittivity between targets, for the examined cases. This is expected, as the dielectric difference between the head tissues is larger for permittivity than conductivity. As MWT is dependent mainly on the difference in permittivity, these differences are not crucial for this examination. These results also have benefited from reconstructions in multiple frequencies based on the use of our in-house developed spear-shaped antennas which operate in a wide range from 0.5 GHz to 2.5 GHz. Additionally, the system was able to reconstruct the target inside a brain phantom even when its structure or dielectric properties are different from the "initial guess" used in the inversion, as well as in the presence of a more realistic phantom structure. Moreover, the flexible tuning of the DBIM-TwIST parameters allows an easy adaptation of the algorithm to the inverse problem at hand. We note that, as with most non-linear inverse methods, the DBIM-TwIST parameters must be tuned based on considerations that relate to both the imaging problem and the experimental prototype. Furthermore, experimental measurement errors may result in certain frequencies providing more accurate reconstructions than others. As a result, the maximum frequency is not the same in every examined case. In this thesis, we chose to present the maximum frequency in which each scenario converges successfully. We note that at every case, the minimum and the maximum frequency are within the antenna operational bandwidth [157]. We note that the experimental phantoms in this chapter are oversimplified in relation to the true head and brain anatomy. However, this simplification was necessary to show that our system and algorithm have the potential to detect and differentiate between the two different stroke types based on

a quantitative estimation of their dielectric properties. The imaging performance of the algorithm and prototype depends strongly on the complexity of the brain, and hence, the experimental phantom that represents it. The skin and skull, for example, introduce strong scattering layers, and the distribution of the CSF can be complex and can obscure the signal from the target. Therefore, in the next chapter, we present an anatomically complex head model and evaluate the performance of DBIM-TwIST for the problem of brain stroke detection. Finally, in this chapter, we have presented the work that has been done during the secondment at Keysight that has examined the preparation of a novel solid material that could improve antenna performance.

Chapter 4

Experimental Validation of 3-D MWT for a Complex Head Phantom

4.1 Introduction

In this section we aim to validate the 3-D DBIM-TwIST algorithm for the problem of brain stroke detection and differentiation, using an anatomically accurate, multi-layer head phantom. To this end, we have developed an anatomically complex head phantom which mimics various brain tissues and also includes a target mimicking hemorrhagic or ischemic stroke. We simulated the model and setup using CST Microwave Studio and then used our experimental imaging setup to collect numerical and measured data, respectively. We then used our DBIM-TwIST algorithm to reconstruct the dielectric properties of the imaging domain for both simulated and measured data. Results from our CST simulations showed that we are able to locate and reconstruct the permittivity of different stroke targets using an approximate initial guess. Our experimental results demonstrated the potential and challenges for successful detection and differentiation of the stroke targets.

4.2 Evaluation of the Impact of Prior Information (Initial Guess)

In MWT, the arisen EM problem is non-linear and ill-posed, therefore a robust algorithm is essential. As some apriori information is needed, MWT algorithms should allow the tuning of the parameters depending on each examined scenario [79]. Specifically for brain imaging, the high dielectric contrast between the different head layers adds an additional challenge to the successful detection and differentiation of brain stroke, using MWT [55]. Therefore, before we validate DBIM-TwIST for more challenging scenarios, there is a need to explore what apriori knowledge is required to achieve a successful differentiation of the types of stroke for a complex scenario. In this section, we investigate whether an improved approximate model as the initial guess could result in stronger reconstructed results, using 3-D DBIM-TwIST and an anatomically accurate head phantom.

4.2.1 Zubal model and Numerical Configuration

The proposed system and model were simulated using CST Microwave Studio. Fig. 4.1 shows the simulated prototype that is composed of a tank with a diameter of 300 mm and filled with 90% glycerol water mixture. Within the tank we placed a six-layer brain model with the shape of the axial slice of the original MRI-derived Zubal head phantom that emulated our experimental phantom [158]. In each layer we allocated the dielectric properties of the equivalent head tissues that were assigned from CST's library. The dispersive dielectric properties of the Zubal head phantom as well as the matching medium's are shown in Table 4.1. The phantom was surrounded by 16 spear-shaped antennas [159] in two arrays and in an elliptical arrangement with major and minor axes equal to 205 mm and 148 mm respectively. A cylindrical target (diameter d = 20.3 mm and height h = 100 mm), which mimics either the hemorrhagic or the ischemic stroke, was placed at the left of the phantom, inside the white matter area.

For each scenario we conducted three simulations to acquire the scattered field data: one without the target (NT), one with hemorrhagic (h-stroke) and one with ischemic (i-stroke) stroke, respectively. We increased the complexity of the Zubal phantom by adding one layer at each time and allocating the dielectric properties of the average brain to the rest of the tissues. Our final six-layer phantom which includes skin, fat, bone, CSF, grey matter, white matter and the stroke-like target are presented at Fig. 4.1. Overall, we examined five scenarios of different complexities, resulting in a total of 15 CST simulations.

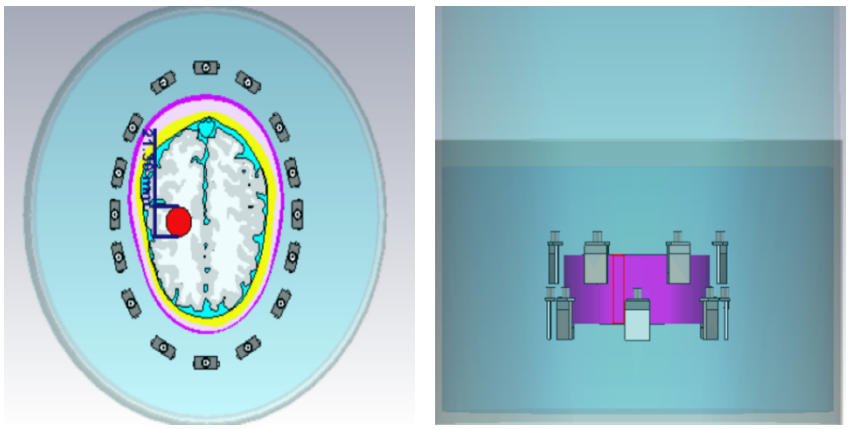

(a) (b)

Figure 4.1: The simulation system prototype in CST, which uses a numerical head model based on the Zubal head phantom. The head model's dimensions are approximately 170 × 130 × 100 mm. Left: X-Y slice, Right: X-Z slice.

4.2.2 Implementation of the 3-D DBIM-TwIST algorithm

The DBIM method which solves the non-linear EM inverse scattering problem by forming iteratively, a system of scattering equations under the Born approximation for every transmit-receive pair, was presented in the previous chapters. For the 3-D DBIM, the electric field and the dyadic Green's function have been calculated by taking into account an $x - y$ horizontal plane, considering that only electric fields at

Table 4.1: Debye parameters of the forward model. The Debye parameters for the head tissues have been assigned by curve fitting from CST data. Debye parameters of the 90% glycerol water and of the i-stroke have been obtained from experimental dielectric measurements that have been presented in [158].

Material type	ϵ_∞	$\Delta\epsilon$	σ_s
90% glycerol water	6.56	16.86	0.3232
Average brain	45.8	0.1244	0.7595
Skin	41.17	11.15	0.6672
Fat	5.331	0.6564	0.037
Bone	11.59	1.932	0.0788
CSF	67.71	5.46	0.21
Grey matter	49.63	11.66	0.7
White matter	36.67	8.6	0.39
H-stroke	59.23	6.142	1.374
I-stroke	25	10	0.01

the z-polarized antennas are important [12], [90]. To capture the frequency-dependent behaviour of the human tissues, we implemented the single-pole Debye model for the complex permittivity which was also presented in Chapter 2 and 3.

For each case, we examined two forward models. The first one consisted of a simplified representation of the simulation setup, which includes the tank filled with the matching medium and an ellipsoid that mimics the average brain tissue. The latter included a multi-layer ellipsoid that represents a simplified version of the multi-layer phantom. By means of an example, Fig. 4.2 presents the forward models for the

three and six-layer Zubal phantom, as well as the forward model filled only with the average brain dielectric properties. In each layer of the forward model we assigned the Debye parameters of the equivalent head tissue which are presented in Table 4.1. The algorithm considered the system's spear-shaped antennas as line sources, which were placed at the same locations as the simulation. To calibrate the simulated model, we used the NT reference measurement.

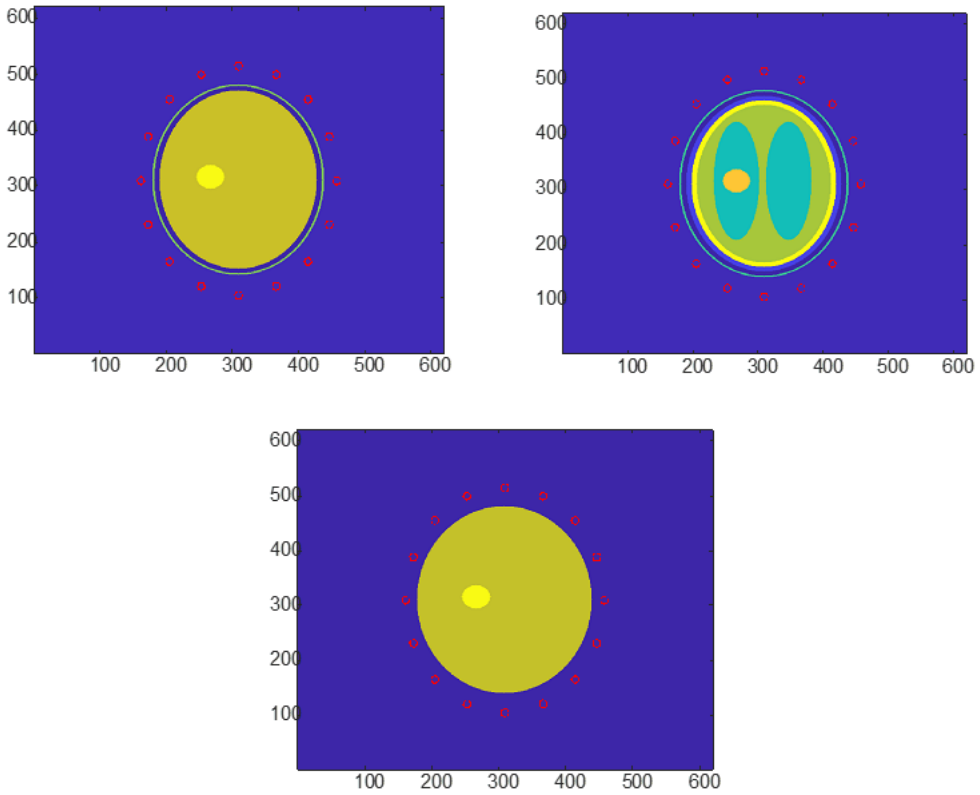

Figure 4.2: Top left: Top view of the forward model for the three-layer Zubal head phantom (skin, fat, bone); Top right: Top view of the forward model for the six-layer Zubal head phantom (skin, fat, bone, CSF, grey matter and white matter); Bottom: Top view of the forward model filled with the average brain. The dimensions of the outer layer of the forward model are 170 $\times$ 130 $\times$ 100 mm.

For the examined scenarios, we measured the S-parameters from 0.5 to 1.5 GHz and we fed the scattered signals into the algorithm. The computation time for the

forward solver for each antenna was approximately 17 seconds. The execution time for each antenna was 80 seconds resulting in a total execution time of 7.1 hours for 20 iterations at each frequency. In this study, we employed the Nvidia GPU Tesla K20c to accelerate the 3-D FDTD implementation with CUDA which was developed by our group [90], and Matlab MEX functions to integrate the GPU code with our DBIM code in Matlab. The implementation was based on Matlab R2020b, CUDA 8.0 and VS 2015.

4.2.3 Results

We present the reconstruction results using the 3-D version of DBIM-TwIST algorithm, for the region surrounded by the antenna array shown in Fig. 4.1. In addition, we define the relative error of ϵ_∞ in the target area, between the inverse and the forward model as:

$$\text{er} = \frac{||\epsilon_\infty \text{original} - \epsilon_\infty \text{reconstructed}||^2}{||\epsilon_\infty \text{original}||^2} \tag{4.1}$$

ϵ_∞ is the concatenated vector representing the spatial variation of ϵ_∞ inside the reconstruction domain. The error metrics are calculated at each DBIM iteration and can be used to compare the quality of the reconstructed images as well as choose the optimal number of iterations. For the examined cases, we chose 20 iterations as our previous experiments has shown that it is a good trade-off between the quality of the images and the total computational time.

Figs. 4.3-4.7 demonstrate the reconstructed results at the horizontal cross-section at the level Z=60 mm achieved with 3-D DBIM-TwIST for 1 GHz, for the case of h- and i-stroke respectively, for both types of forward models. The size of the 3-D domain is 100 mm $\times$ 100 mm $\times$ 100 mm with a resolution of 2 mm. Figs. 4.3-4.6 reveal that we achieve similar reconstructed images while using the multi-layer initial model for both stroke targets. We also note that the reconstructed values of the targets, are closer to their real values when using the homogeneous forward model. However, in Fig. 4.7

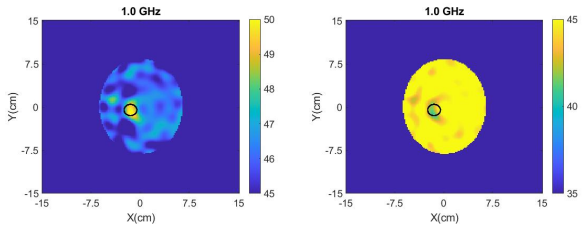

(a) (b)

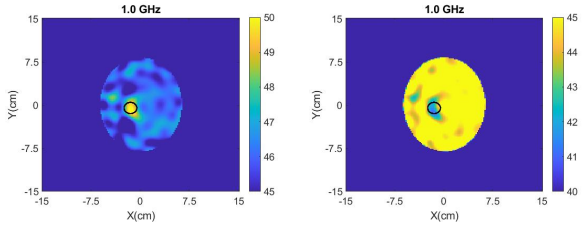

(c) (d)

Figure 4.3: Reconstructed results of the real part of the complex permittivity for the Zubal model including the skin and average brain layers, for the cases of hemorrhagic and ischemic stroke respectively. Top: Homogeneous forward model; Bottom: Forward model that includes the skin and average brain layers.

we observe that the quality of the reconstructed h-stroke is better when we apply a homogeneous initial model, while for the case of i-stroke, we achieve fewer artifacts when using a multi-layer forward model.

Fig. 4.8 plots the e_r of ϵ_∞ in the target area, as a function of DBIM iterations. We observe that in most cases the values between the homogeneous and the multi-layer forward model are similar both for hemorrhagic and ischemic stroke. However, we also note that for the six-layer Zubal model, h-stroke's e_r for the multi-layer forward model is higher than the equivalent value for the homogeneous forward model, while we notice the opposite for the i-stroke. The plots of Fig. 4.8 further validate what we observed from the reconstructed images.

Overall, the results indicate that for most scenarios, the use of a homogeneous forward model produces slightly better reconstructed images than the multi-layer forward

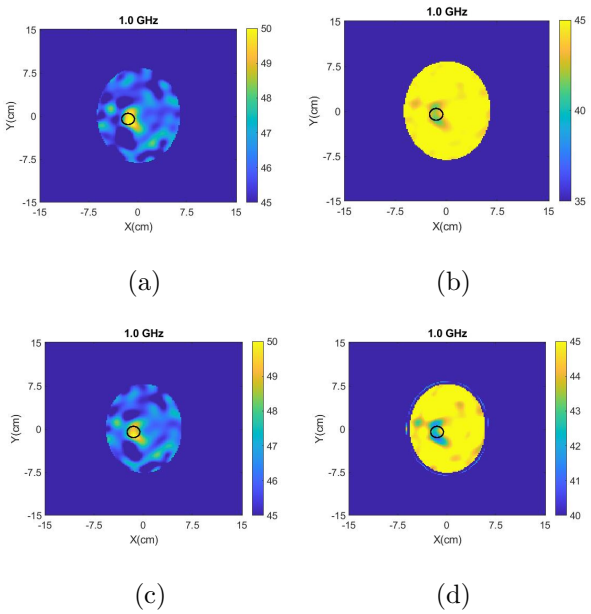

Figure 4.4: Reconstructed results of the real part of the complex permittivity for the Zubal model including the skin, fat and average brain layers, for the cases of hemorrhagic and ischemic stroke respectively. Top: Homogeneous forward model; Bottom: Forward model that includes the skin, fat and average brain layers.

model. However, for the case of Zubal head phantom in the presence of all head tissues, we observe that we achieve better results while applying an improved forward model, for the case of ischemic stroke where the dielectric contrast between the target and the background tissue is less than the equivalent dielectric difference in the presence of hemorrhagic stroke. We note that for the DBIM-TwIST there is no "best parameter" that improves the quality of the reconstructed images. One of the advantages of this method lies on its adaptive parameters that can be adjusted according to each scenario.

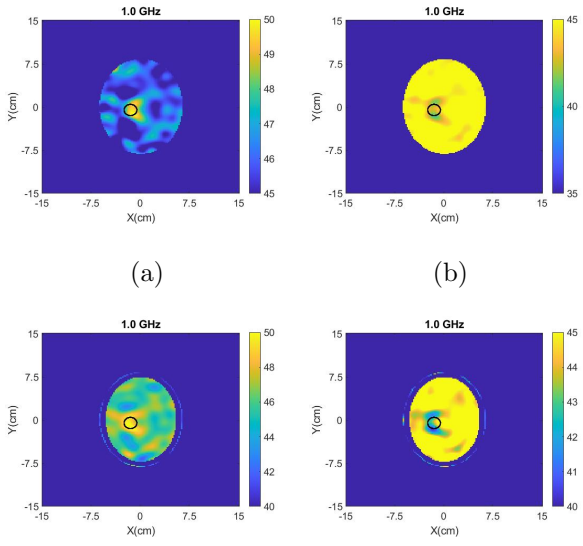

Figure 4.5: Reconstructed results of the real part of the complex permittivity for the Zubal model including the skin, fat, bone and average brain layers, for the cases of hemorrhagic and ischemic stroke respectively. Top: Homogeneous forward model; Bottom: Forward model that includes the skin, fat, bone and average brain layers.

4.3 Comparison of 2-D and 3-D DBIM-TwIST for a 3-D Head Imaging Problem

In this section we present an initial validation and assessment of the 3-D algorithm for the case of a simplified homogeneous elliptical brain phantom in the presence of a small stroke-like target, surrounded by a 3-D antenna array arranged in two cylindrical rings. We also compare the capabilities of the 2-D and 3-D versions of the algorithm to confirm the hypothesis that 3-D DBIM-TwIST can result in more accurate reconstructions for 3-D inverse problems.

Fig. 4.9 illustrates the brain phantom immersed in our imaging setup presented at [159]. The phantom is surrounded by 16 spear-shaped antennas in two different arrays, which form two offset rings of 8 elements each. To mimic the h-stroke or

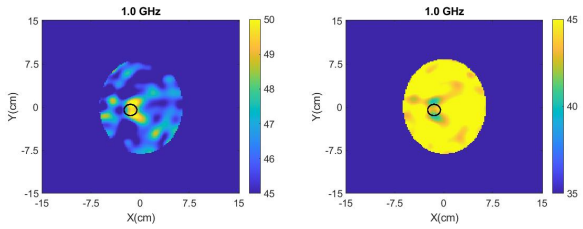

(a) (b)

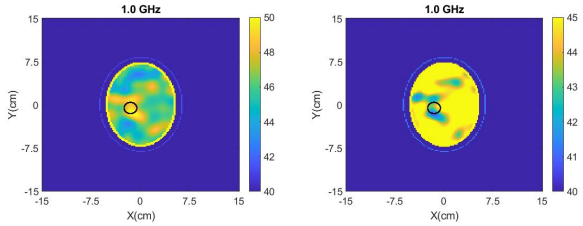

(c) (d)

Figure 4.6: Reconstructed results of the real part of the complex permittivity for the Zubal model including the skin, fat, bone, CSF and average brain layers, for the cases of hemorrhagic and ischemic stroke respectively. Top: Homogeneous forward model; Bottom: Forward model that includes the skin, fat, bone, CSF and average brain layers.

the i-stroke, we have examined the same configuration in the presence of a 20 mm diameter and 20 mm height target, located between the two heights of the antennas. The Debye parameters of the target and of the average brain have been assigned by curve fitting from CST data [159]. As explained before, the inverse model used in our imaging algorithm considers a 2-D (112 $\times$ 153 mm), or a 3-D (112 $\times$ 153 $\times$ 100 mm) ellipsoid, for the two versions of the algorithm respectively. The algorithm considers point sources which form an elliptical array and are located at the same height in 3-D case as the antennas in the CST simulation.

Figs. 4.10- 4.13 present the reconstructed permittivity and conductivity at 1 Ghz for the phantom of Fig. 4.9 for h- and i-stroke respectively, using both 2-D and 3-D versions of the DBIM-TwIST. More specifically, Fig. 4.10 shows the 2-D reconstructed

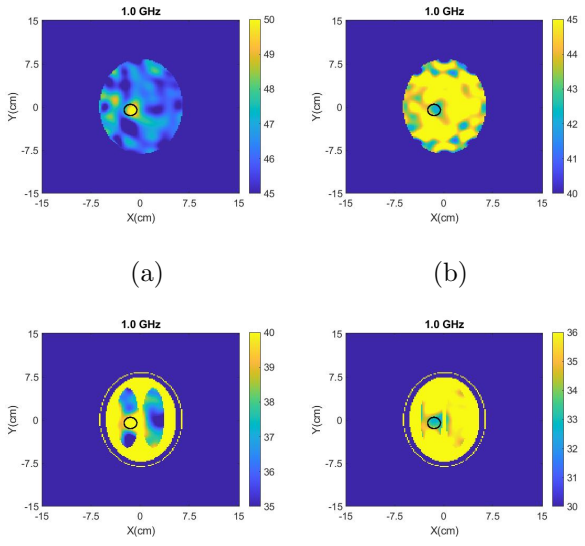

Figure 4.7: Reconstructed results of the real part of the complex permittivity for the Zubal model including all the head layers, for the cases of hemorrhagic and ischemic stroke respectively. Top: Homogeneous forward model; Bottom: Forward model that includes all the head layers.

permittivity and conductivity using either the top or the bottom array of antennas in our forward model. The results vary between the two rows due to the different gap size between each array of antennas and the matching medium-air interface. Figs. 4.11-4.13 demonstrate the sagittal, axial and coronal planes at Y-Z, X-Z and X-Y slices from the 3-D reconstructions, respectively.

We observe that both versions of the algorithm can successfully locate and detect the dielectric permittivity of the target. However, the 3-D algorithm achieves more accurate results for both cases of stroke, as it combines information from the S-parameters collected from both rings of antennas. Importantly, the 3-D DBIM-TwIST leads to a clear improvement in estimating the target's conductivity relative to 2-D reconstruction based on either ring. Having established the benefits of 3-D imaging, our subsequent results focus on validating the 3-D DBIM-TwIST experimentally, as well as comparing

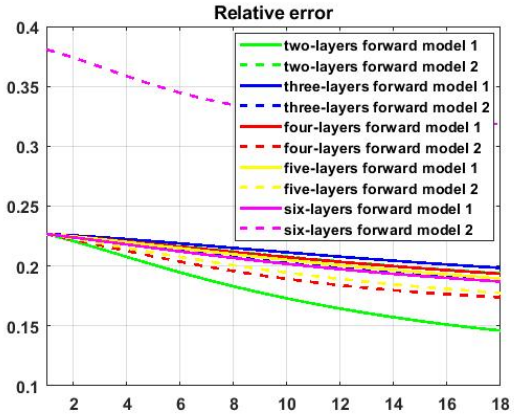

(a)

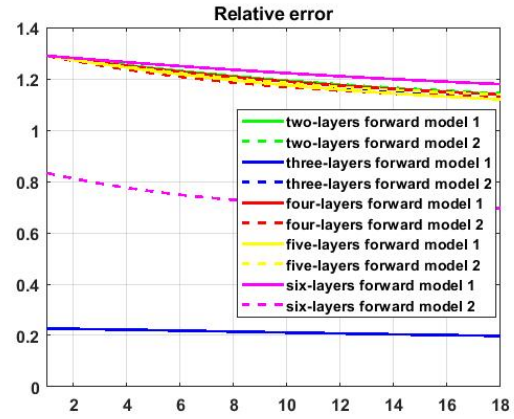

(b)

Figure 4.8: Top: Relative error of the ϵ_∞ in the target area for h-stroke at 1 GHz; Bottom: Relative error of the ϵ_∞ in the target area for i-stroke at 1 GHz.

its performance with the 2-D version of the algorithm. The experimental setup and respective CST model, however, do not include two antenna rings due to the smaller size of the experimental phantom. In this respect, the setup in these results resembles a 2-D configuration, but the 3-D results are still relevant as they are derived from the 3-D algorithm which reconstructs a fully 3-D region.

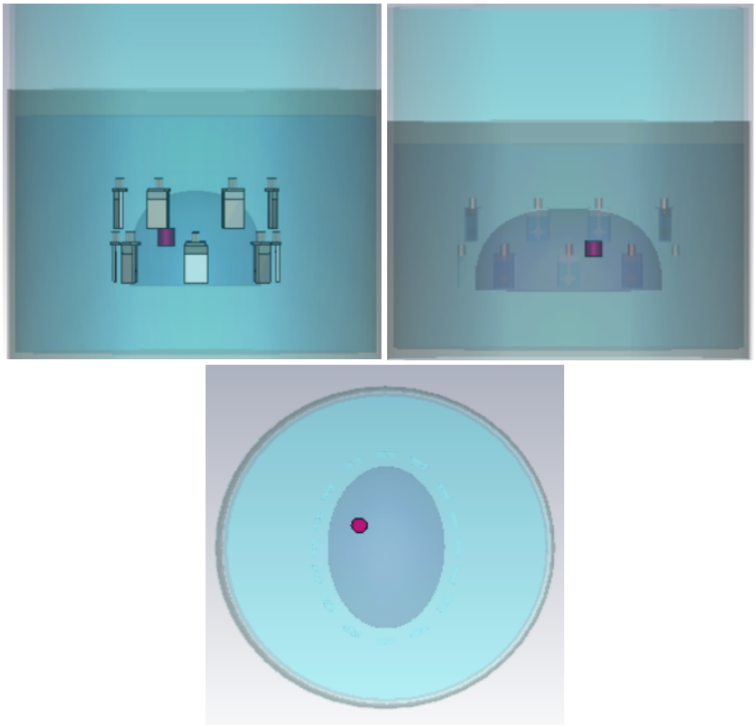

Figure 4.9: CST model of a simplified brain phantom surrounded by 16 antennas in 2 elliptical arrays; Top left: X-Z slice; Top right: Y-Z slice; Bottom: X-Y slice.

4.4 Experimental Methodology

4.4.1 Head Phantom Construction

We derived our Zubal phantom from a 2-D axial $x-y$ slice taken from the original MRI-derived Zubal head phantom [158], which was then extended by a few cm along the z axis. We imported this 3-D model in CAD software to simplify its structure so that it is easy to fabricate and work with, without sacrificing much of its complexity (Fig. 4.14(a) and Fig. 4.14(b)). The CAD model was designed by Ioannis Sotiriou, a member of our research group at King's College London. For our simulation, we imported the CAD model on CST which from now on we will refer to as the "Zubal model". The simulated phantom and setup are shown in Fig. 4.14(c) and Fig. 4.14(d). We filled each layer of the phantom with the dielectric properties of different head tissues having created an

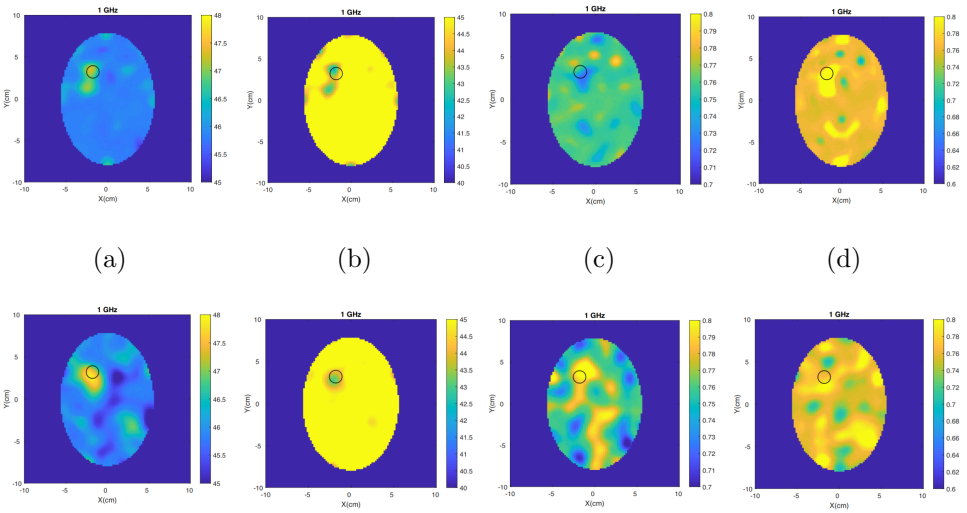

(a) (b) (c) (d)

(e) (f) (g) (h)

Figure 4.10: First row (a) and (b): Reconstructed permittivity for the phantom of Fig. 4.9, for h- and i-stroke using 2-D DBIM-TwIST and the bottom array of antennas; First row (c) and (d): Reconstructed conductivity for the phantom of Fig. 4.9, for h- and i-stroke using 2-D DBIM-TwIST and the bottom array of antennas; Second row (e) and (f): Reconstructed permittivity for the phantom of Fig. 4.9, for h- and i-stroke using 2-D DBIM-TwIST and the top array of antennas; Second row (g) and (h): Reconstructed conductivity for the phantom of Fig. 4.9 for h- and i-stroke using 2-D DBIM-TwIS and the top array of antennas.

anatomically accurate 5-material head model. We placed a cylindrical target at the top right, inside the white matter area, with radius $\rho = 12.5$ mm and height h = 100 mm. The phantom was immersed in our imaging setup presented in [159], which includes eight spear-shaped antennas placed in an elliptical array configuration with major and minor axes equal to 205 mm and 148 mm, respectively.

To validate the algorithm experimentally, we prepared a novel gelatine-based head phantom in accordance with the anatomy and dimensions of the Zubal model. The mould form was designed and 3-D printed by Ioannis Sotiriou and consists of six compartments which create the sequence of the tissue-mimicking materials needed for

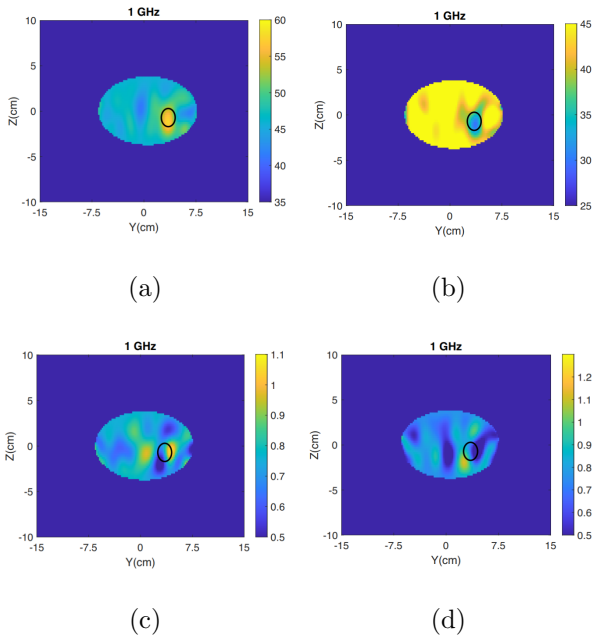

Figure 4.11: First row: Y-Z slice of 3-D reconstructed permittivity for the phantom of Fig. 4.9 for h- and i-stroke; Second row: Y-Z slice of 3-D reconstructed conductivity for the phantom of Fig. 4.9 for h- and i-stroke.

our assembly. The moulds were fabricated using a Zortrax M200 FDM 3-D printer in a complementary manner using two moulds shown in Fig. 4.15(a) and Fig. 4.15(b). This methodology for the creation of the phantom allows a more accurate validation as it avoids the presence of 3-D printed infill patterns that irregularly encapsulate fluids. The adverse effect of the presence of plastic in phantoms which use it as support was demonstrated in [160].

Having prepared the tissue-mimicking gels, we poured them into the desired compartments in Fig. 4.15(a) and Fig. 4.15(b), and we allowed them to dry for at least 8 hours depending on their concentration. To extract the gels from the moulds we initially submerged the moulds in warm water so the outer layers could slide out easier, whilst we were applying small amount of air pressure at the lower part of the mould (Fig. 4.16). Once the gels were extracted, we stacked the materials within each other and wrapped the assembly using a thin plastic film to prevent it from drying. The final

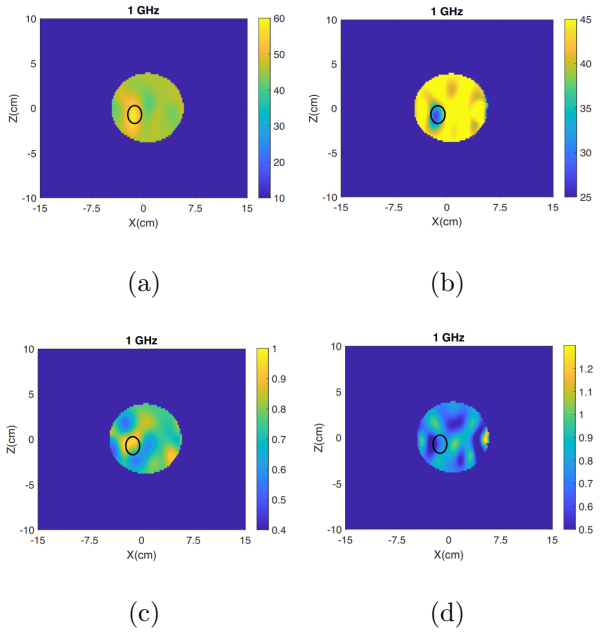

Figure 4.12: First row: X-Z slice of 3-D reconstructed permittivity for the phantom of Fig. 4.9 for h- and i-stroke; Second row: X-Z slice of 3-D reconstructed conductivity for the phantom of Fig. 4.9 for h- and i-stroke.

Zubal model is presented in Fig. 4.15(c).

We prepared the tissue-mimicking materials for skin, bone, CSF, grey matter, white matter, blood and ischemia by following the process presented in the previous chapter and the equivalent paper [159]. Table 4.2 shows the concentrations of the materials used for preparing each layer of the phantom.

Fig. 4.17 displays the measured dielectric properties of the prepared phantoms for skin, bone, grey matter, white matter and ischemia, respectively. We note that the figure does not report the measured properties of CSF/h-stroke, as the material was not set at the time of the dielectric measurements. The preparation of CSF/h-stroke does not require the addition of oil, which is the most challenging step in the preparation process and can lead to variations in the final dielectric properties of the phantoms. Preparing phantoms that mimic the dielectric properties of CSF or h-stroke requires only dissolving the gelatine within the water. Therefore, we can safely assume that we

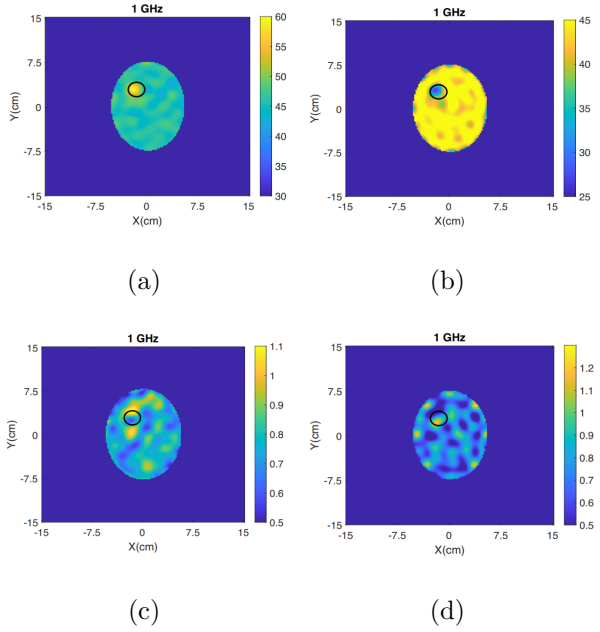

Figure 4.13: First row: X-Y slice of 3-D reconstructed permittivity for the phantom of Fig. 4.9 for h- and i-stroke; Second row: X-Y slice of 3-D reconstructed conductivity for the phantom of Fig. 4.9 for h- and i-stroke.

Table 4.2: Concentrations of materials used for 100 ml of tissue-mimicking phantoms. For each tissue-mimicking phantom we also use 1 ml of propanol and 1 ml of surfactant.

	Water	**Gelatine powder**	**Kerosene + Safflower oil**
Skin	73 ml	13 gr	15 ml
Bone	45 ml	5 gr	50 ml
CSF/h-stroke	80 ml	17 gr	-
Grey matter	75 ml	12 gr	13 ml
White matter	70 ml	10 gr	20 ml
i-stroke	55 ml	10 gr	35 ml

can achieve the properties reported at [159]. For the CSF/h-stroke fabricated phantom of [159] the permittivity at 1 GHz is 68, while the conductivity is 0.3 S/m and 1.2 S/m for h-stroke and CSF respectively. The measurements were performed using Keysight's

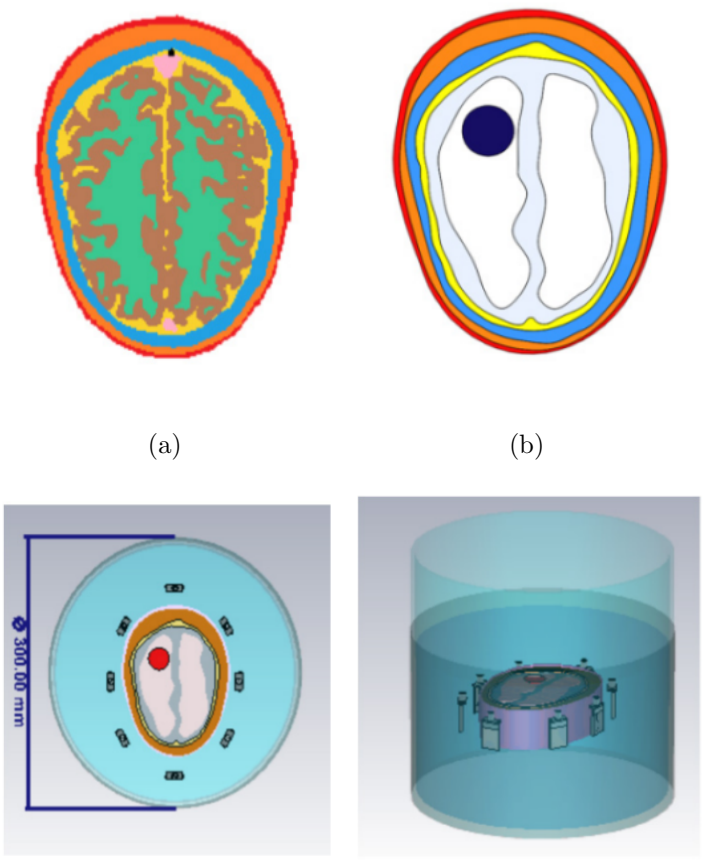

Figure 4.14: (a) The Zubal head model section; (b) Simplified CAD model for fabrication; (c) Top view of the Zubal model on CST; (d) Side view of the Zubal model on CST. The phantom includes the following head layers: Skin, bone, CSF, grey matter, white matter and the target.

dielectric spectroscopy kit, over a 0.5-1.5 GHz frequency range at different points. The plots reveal a very good agreement with the reference permittivity taken from CST (Fig. 4.17(a)), but lower conductivity values for skin and grey matter phantoms (Fig. 4.17(b)). As there is no literature regarding the dielectric properties of ischemia in a wide frequency range, we made the assumption that the ischemic properties are 25% less than the dielectric properties of healthy brain tissue [77].

(a) (b)

(c)

Figure 4.15: Top view of the moulds constructing the Zubal head phantom from gelatine-based tissue-mimicking materials: (a) First mould (bone, grey matter, and target); (b) Second mould (skin, CSF and white matter); (c) Final phantom with five tissues and target.

4.4.2 Imaging methodology

The Zubal model was positioned in the middle of the 300 mm diameter cylinder tank, as shown in Fig. 4.18(a). It was surrounded by eight spear-shaped antennas [148] in an elliptical array, and the imaging tank was filled with 90% glycerol water. The

Figure 4.16: Demoulding process.

experimental system, the choice of a number of antennas, as well as the choice of the matching medium have been extensively reported in our previous chapter. The setup was surrounded by vacuum and the measurements were performed in the frequency range of 0.5 to 1.5 GHz. For every studied case, two scenarios were examined. First, we considered a scenario without a target (NT), where the target area was filled with the dielectric properties of the white matter. For the WT scenario we filled the equivalent target territory (radius ρ = 12.5 mm and height h = 100 mm) with the dielectric properties either of blood or of ischemia. For each scenario and for M frequency points, the eight antenna-array captured the MWT data, resulting in an $8\times$ 8 $\times$ M scattering matrix, which was then fed and processed by our algorithm. A flowchart of the method is presented at Fig. 4.18(b).

Our forward model consisted of both a 2-D and 3-D depiction of the set-up for the two versions of the DBIM-TwIST respectively. It included the tank filled with the dielectric properties of 90% glycerol water and an ellipsoid that represented the Zubal model filled with the dielectric properties of the average brain. The axes of the 2-D ellipsoid were 153 mm and 112 mm long and they represented the actual size of the

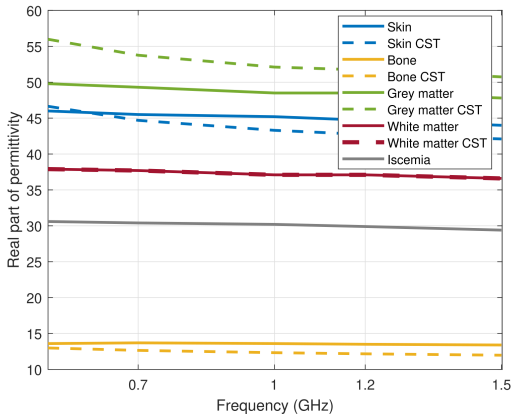

(a)

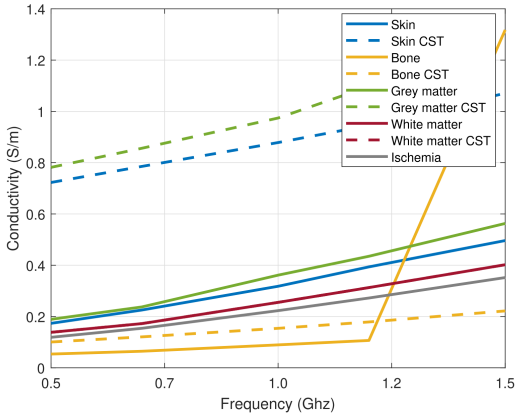

(b)

Figure 4.17: Measured dielectric properties of the produced tissue-mimicking materials against reference values taken from CST: (a) permittivity, and (b) conductivity. Note that there appears to be a measurement error for the bone phantom above 1.2 GHz.

phantom's axial slice at the height where the antennas were located. The dimensions of the 3-D ellipsoid were 170 $\times$ 130 $\times$ 100 mm long.

As the forward models are simplified versions of the experiment, they are not identical and hence there are differences between the real and the FDTD simulated models. The algorithm simulated the setup's antennas with line sources placed at the same location as their feeding point. To minimize the mismatch between the simulation or

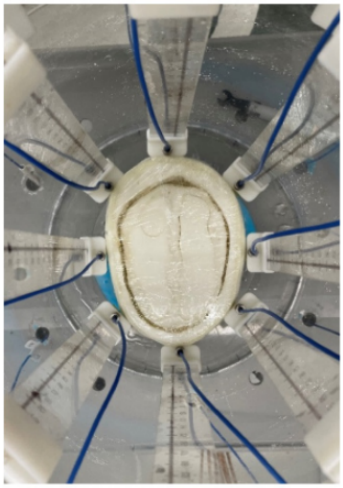

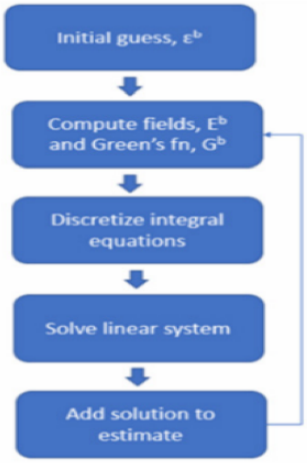

(a) (b)

Figure 4.18: (a): The imaging tank with the immersed Zubal model. (b): Flowchart of the DBIM method.

the experiment and the forward model, we calibrated our forward model by employing a NT scenario, as presented in the previous chapter and the equivalent publication ([159]). We calculated the signal difference between the inverse and the forward NT cases and we used this difference to calibrate the scattered data taken from the WT scenario.

Table 4.3: Debye parameters of the forward model.

Material type	ϵ_∞	$\Delta\epsilon$	σ_s
90% glycerol water	6.56	16.86	0.3232
Average brain	45.8	0.1244	0.7595

To model the frequency-dependent behaviour of the human tissues, we applied the single-pole Debye model for the complex permittivity ϵ_b [159]. Table 4.3 presents the Debye parameters of the "initial guess" model that were used with the FDTD

forward solver to calculate the 2-D (transverse magnetic wave) and 3-D (full wave) fields. The calculation of full wave fields is the main difference between the 2-D and the 3-D version of the algorithm. The Debye parameters are calculated and updated at each iteration until we reach a fixed number of iterations or the difference between the "measured" and calculated electric fields is minimised. We employ DBIM-TwIST to reconstruct the Debye parameters with a 2 mm resolution grid. We have observed that the reconstructed results do not improve significantly when we apply more than 20 iterations, and hence we chose to perform 20 DBIM iterations for both 2-D and 3-D versions of DBIM-TwIST. This number is a trade-off between the accuracy and the total execution time.

For the 3-D code, we employed the Nvidia GPU Tesla K20c to accelerate the 3-D FDTD execution with CUDA, and Matlab MEX functions to incorporate the GPU code with the DBIM code in Matlab. The environment was based on Matlab R2020b, CUDA 8.0 and VS 2015. The implementation of DBIM-TwIST with a GPU-based FDTD forward solver was extensively described in [90]. By the means of an example, using the 3-D DBIM-TwIST, for the case of the Zubal model with h-stroke, the elapsed time for each antenna was 81 seconds, meaning that the running time for each iteration was roughly 11 minutes when using 8 spear-shaped antennas. For the 2-D code we do not need GPU acceleration for the forward solver. The running time for each iteration, when using 8 spear-shaped antennas, was 12 seconds using Matlab R2020b on an Intel i7 processor with 16 GB RAM memory. We note that the purpose of this thesis was to validate and compare the imaging performance of DBIM-TwIST and not the efficiency of the two versions of the algorithm in terms of time, space and system settings. Therefore, when we compare the 2-D and 3-D results we focus on the validity and accuracy of the reconstruction images in comparison to our simulation or experimental model.

4.5 Results With the Zubal Phantom

This section presents reconstruction results from our Zubal model in the presence of a hemorrhagic and an ischemic stroke. Our aim was to assess our imaging system's ability to determine the type of stroke by estimating its dielectric properties using the 2-D and 3-D DBIM-TwIST algorithm. We have examined both CST-calculated and experimental data, and we have compared our 2-D and 3-D results. As previous work in MWT has shown that thermal noise does not affect reconstruction quality as much as the mismatch between the true experiment and the inverse model, we did not include thermal noise in the CST data, to focus on the effect of the model mismatch errors [84], [161]. The measured data that were used for these reconstructions, were not obtained from the FDTD solver and they were different from the background data which were calculated with FDTD. As a result, there was no "inverse crime". We note that thermal noise can affect the equipment noise floor and as a result the SNR. However, in experimental MWI systems the low SNR levels associates more to errors because of coupling due to cable movement, environmental factors and machine noise [84]. To compare the quality of the reconstructed images we calculated the relative errors of the permittivity and conductivity in the target area at each iteration, as in 4.1.

4.5.1 Reconstructions with CST Data

Two CST simulations were conducted to acquire the scattered field data, with and without the target. The dielectric properties of each tissue were imported from the CST library. Specifically for the ischemic target, as there are no frequency-dependent reported values in the literature, we used our measured dielectric properties reported in [159].

Fig. 4.19 and Fig. 4.20 present the reconstructed permittivity and conductivity at four frequencies for the Zubal model of Fig. 4.14 inside our prototype, in the presence of h-stroke and i-stroke targets. More specifically, Fig. 4.19 shows the reconstructed

permittivity and conductivity for the 2-D version of DBIM-TwIST, while Fig. 4.20 shows the equivalent reconstructed dielectric properties for the 3-D version. Overall, more accurate results are produced for the lower frequencies of 0.9 and 1 GHz, and artifacts increase significantly for frequencies above 1 GHz. This can be attributed to the increased non-linearity of the EM inverse scattering problem in higher frequencies, where multiple scattering effects become stronger.

We also observe that there is a clear distinction in the estimation of the permittivity for the two targets for both versions of the code. For 2-D DBIM-TwIST, the results of Fig. 4.19 estimate the value of permittivity ϵ' at 1 GHz as ϵ'=50.31 and ϵ'=43.15 for hemorrhagic and ischemic stroke, respectively. For the 3-D DBIM-TwIST, Fig. 4.20 shows that the equivalent values of permittivity are ϵ'=61.58 and ϵ'=28.52, respectively. The permittivity of hemorrhagic and ischemic stroke in the experiments is roughly 60 and 25, respectively. Therefore, we observe that 3-D DBIM-TwIST estimates more accurately the reconstructed values for the target area. The equivalent reconstructions of Fig. 4.19 reveal that we are not able to successfully detect the target from the conductivity reconstructions. The quality of conductivity reconstructions improves using the 3-D DBIM-TwIST algorithm, for which the reconstructed conductivity values are significantly different for the two stroke-type targets.

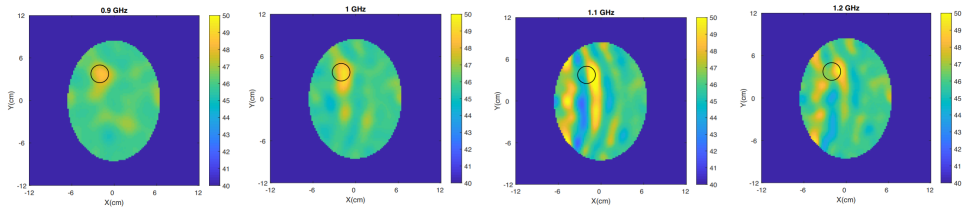

(a) (b) (c) (d)

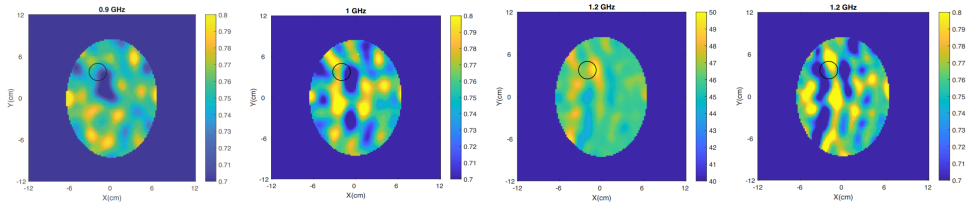

(e) (f) (g) (h)

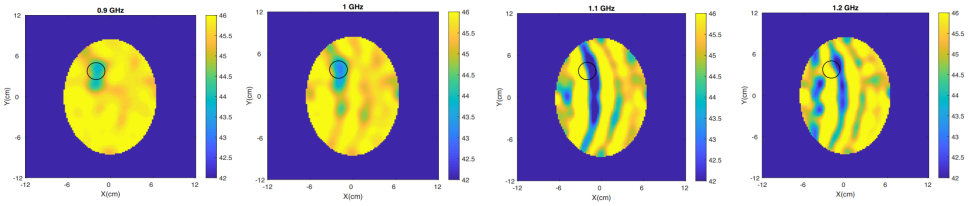

(i) (j) (k) (l)

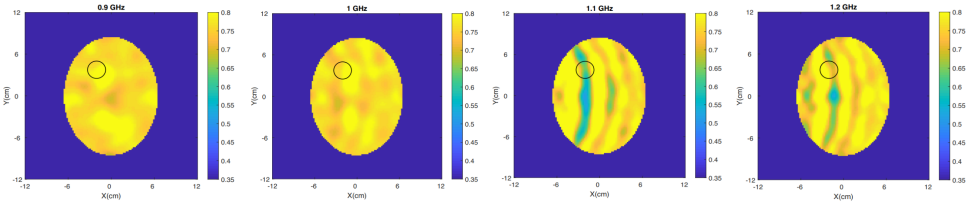

(m) (n) (o) (p)

Figure 4.19: First row: CST reconstructed results of the permittivity for h-stroke using 2-D DBIM-TwIST; Second row: CST reconstructed results of the conductivity for h-stroke using 2-D DBIM-TwIST; Third row: CST reconstructed results of the permittivity for i-stroke using 2-D DBIM-TwIST; Fourth row: CST reconstructed results of the conductivity for i-stroke using 2-D DBIM-TwIST.

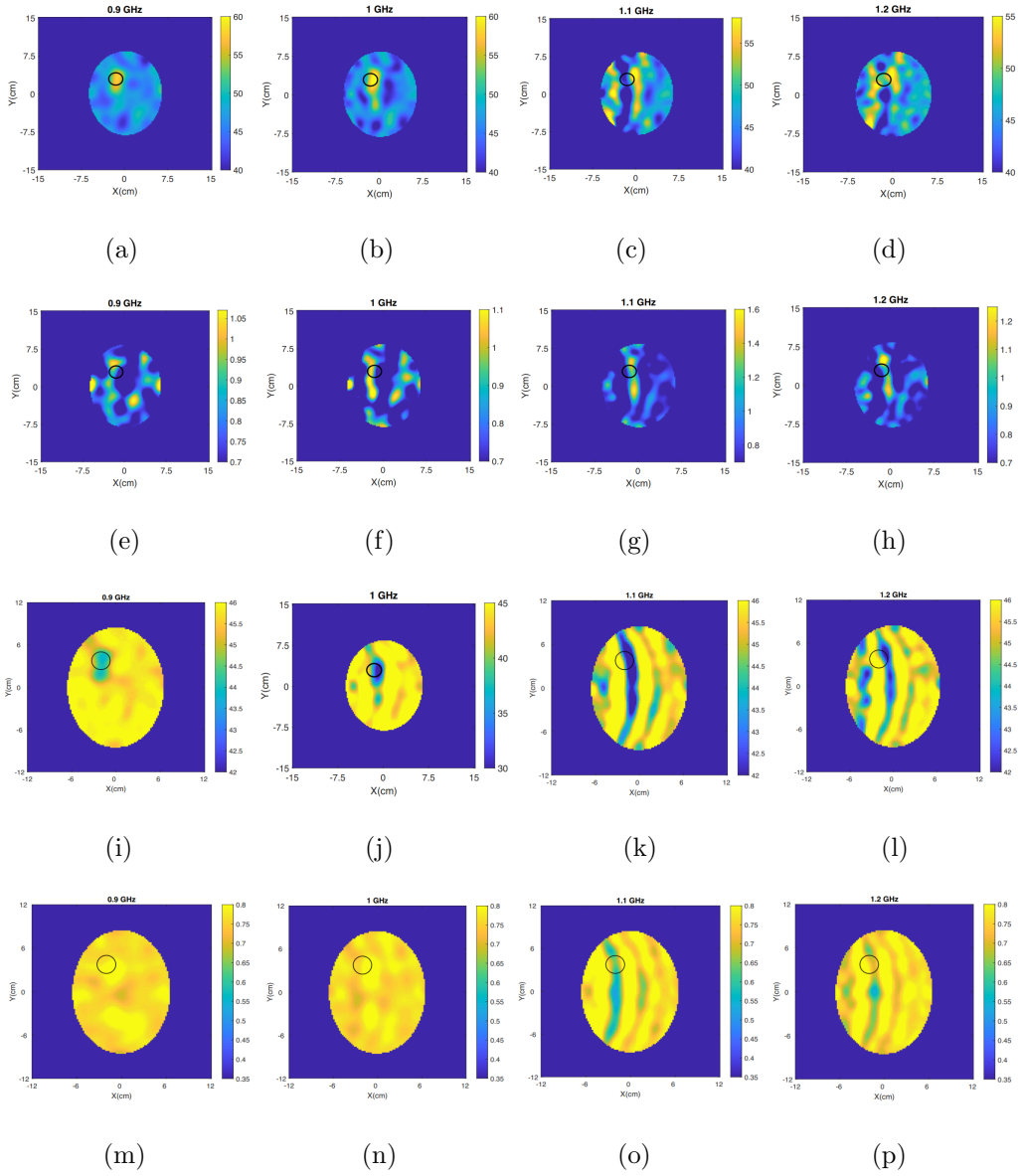

Figure 4.20: First row: CST reconstructed results of the permittivity for h-stroke using 3-D DBIM-TwIST; Second row: CST reconstructed results of the conductivity for h-stroke using 3-D DBIM-TwIST; Third row: CST reconstructed results of the permittivity for i-stroke using 3-D DBIM-TwIST; Fourth row: CST reconstructed results of the conductivity for i-stroke using 3-D DBIM-TwIST.

4.5.2 Reconstructions with Experimental Data

Fig. 4.21 and Fig. 4.22 present complex permittivity reconstructions in the presence of the hemorrhagic or ischemic stroke target, using measured data and the 2-D and 3-D DBIM-TwIST, respectively. These images suggest that we are able to detect and estimate the dielectric properties of h-stroke for both versions of the algorithm. The 3-D DBIM-TwIST reconstructions of the permittivity have more artifacts that could be misleading regarding the target location in the absence of apriori information. Interestingly, the 3-D version of the algorithm leads to conductivity reconstructions with less artifacts than the equivalent permittivity results for the h-stroke case at lower frequencies. Permittivity values at 1 GHz are ϵ'=51.6 and ϵ'=61.57, for the 2-D and 3-D DBIM-TwIST respectively while The permittivity of hemorrhagic target in the experiments is roughly 68. That reveals an agreement between the real and the reconstructed values of the hemorrhagic stroke. However, we observe artifacts in the reconstruction images for reconstructions with the ischemic stroke. More specifically and as shown in Figs. 4.21(i)- 4.21(l) and Figs. 4.22(i)- 4.22(l), we are able to detect an area with values lower than the average brain, which is close to the target area. There is an offset, however, between the location of the real and the detected target. The results in Figs. 4.21(m)- 4.21(p) and Figs. 4.22(m)- 4.21(p) for the conductivity reconstructions reveal similar tendencies.

The dielectric difference observed between the i-stroke and the white matter is less than the dielectric difference between the h-stroke and the white matter, resulting in a more complex brain structure. In addition, differences between our experimental model and the FDTD forward model, in combination with different software environments, result in a significant model mismatch. Overall, both 2-D and 3-D algorithms have detected accurately the h-stroke, although we observe more artifacts for the 3-D version. Overall, experimental measurement errors lead to less accurate reconstructions than their CST equivalent. In general, the results are frequency dependent, and more artifacts are observed in higher frequencies.

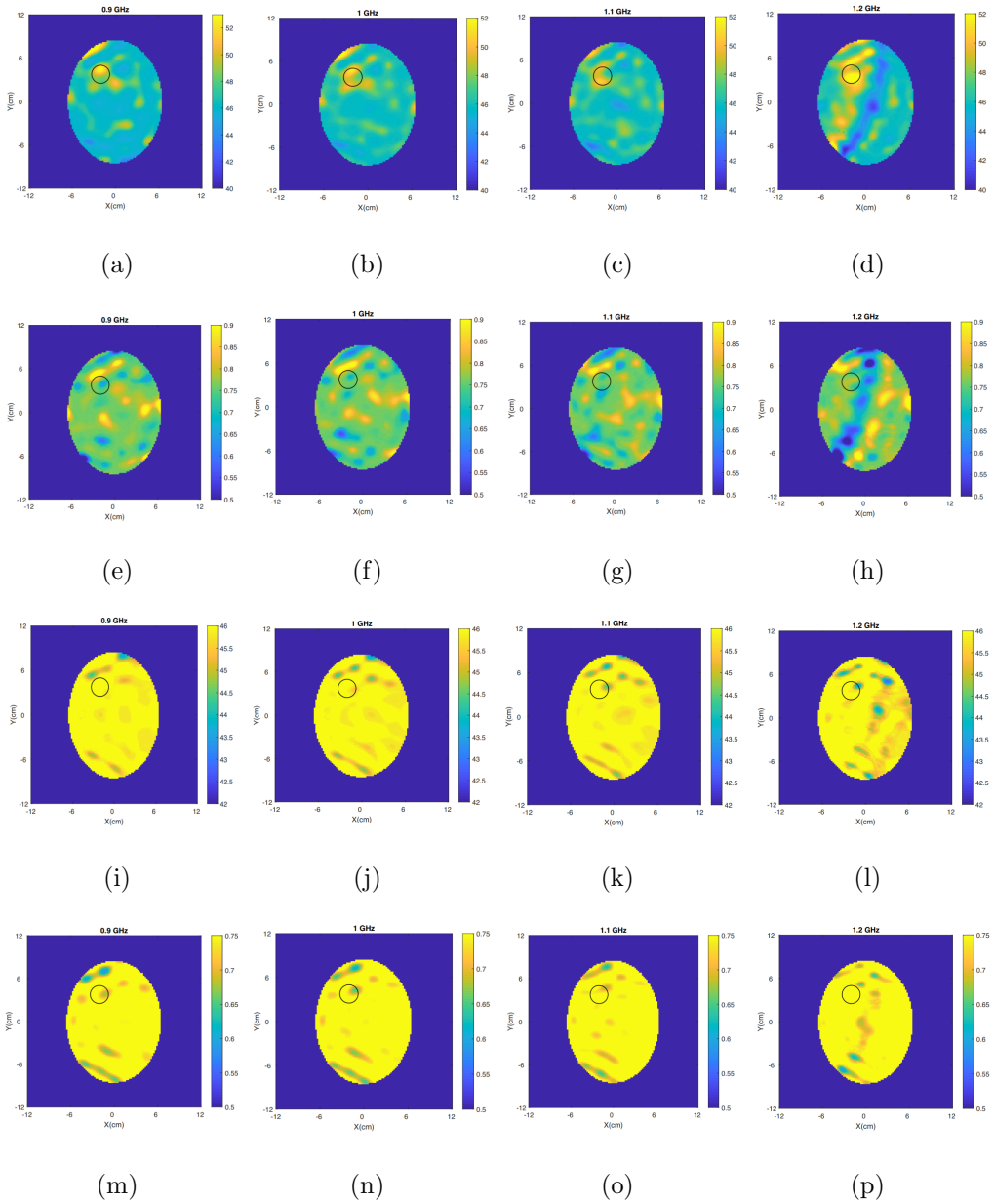

Figure 4.21: First row: Experimental reconstructed results of the permittivity for h-stroke using 2-D DBIM-TwIST; Second row: Experimental reconstructed results of the conductivity for h-stroke using 2-D DBIM-TwIST; Third row: Experimental reconstructed results of the permittivity for i-stroke using 2-D DBIM-TwIST; Fourth row: Experimental reconstructed results of the conductivity for i-stroke using 2-D DBIM-TwIST.

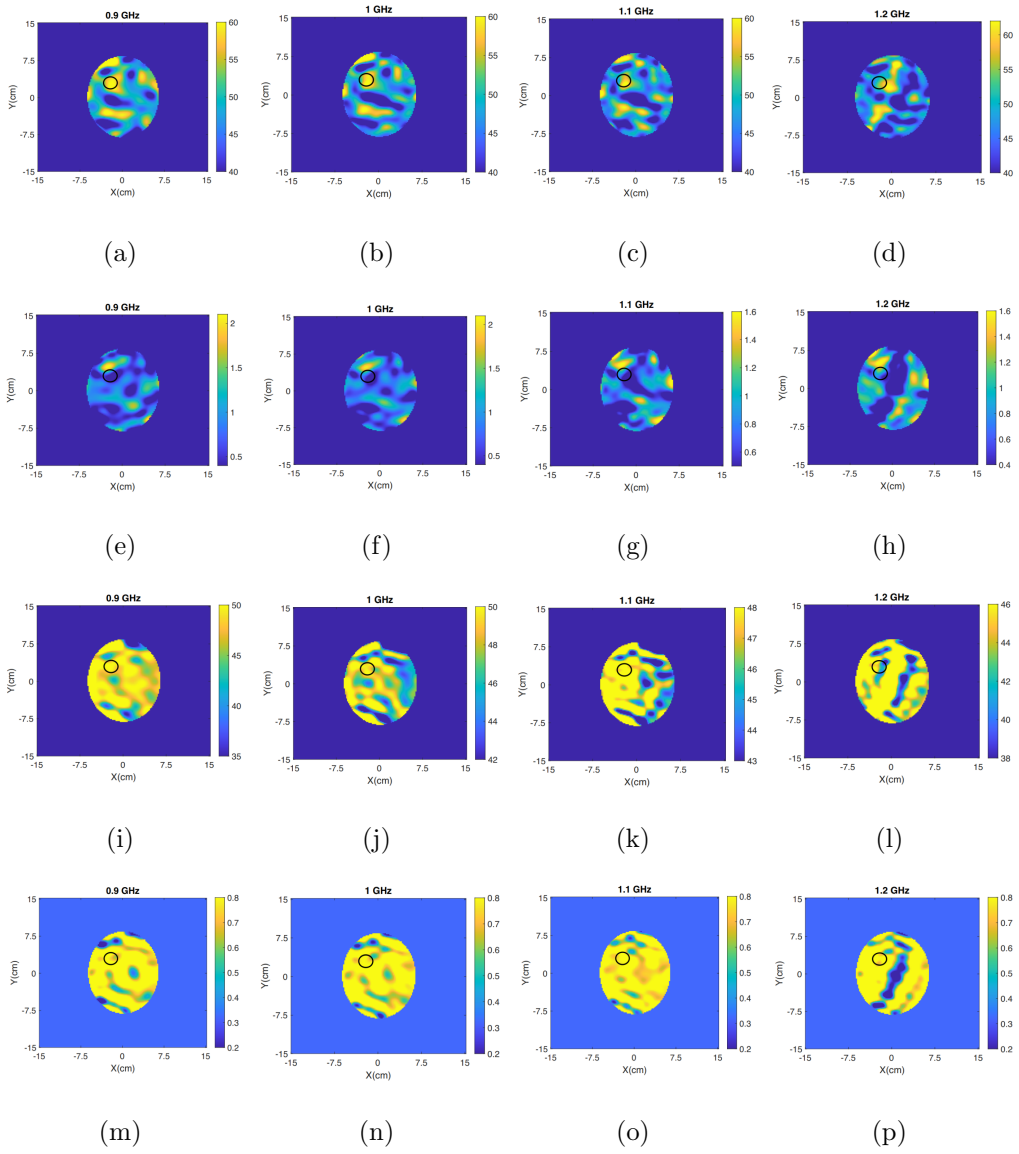

Figure 4.22: First row: Experimental reconstructed results of the permittivity for h-stroke using 3-D DBIM-TwIST; Second row: Experimental reconstructed results of the conductivity for h-stroke using 3-D DBIM-TwIST; Third row: Experimental reconstructed results of the permittivity for i-stroke using 3-D DBIM-TwIST; Fourth row: Experimental reconstructed results of the conductivity for i-stroke using 3-D DBIM-TwIST.

The error metrics calculated by Equation (4.1) can be used to evaluate the accuracy

of the reconstruction. These errors are summarized in Tables 4.4- 4.7. We observe that relative errors fall below 1 for all cases except for the conductivity errors of the 2-D i-stroke cases, as well as the 3-D i-stroke scenarios, where image artifacts are dominant. The high conductivity errors for the 2-D experimental i-stroke suggest that the estimation of the target is not accurate. This is due to an offset between the real and the reconstructed target area for the experimental i-stroke reconstructions. The lowest values are observed for the cases of 2-D and 3-D h-stroke with CST data, at 1 and 0.9 GHz, respectively. Comparing all the images, these are the scenarios with the best estimated reconstructed target and the weakest artifacts.

Table 4.4: Relative errors of the permittivity in the target area for the 2-D examined scenarios.

	0.9 GHz	**1 GHz**	**1.1 GHz**	**1.2 GHz**
CST h-stroke	0.2051	0.1877	0.2259	0.2121
CST i-stroke	0.7853	0.7595	0.7843	0.8303
Exp h-stroke	0.1951	0.1929	0.1944	0.1460
Exp i-stroke	0.8613	0.8524	0.8465	0.8414

Table 4.5: Relative errors of the conductivity in the target area for the 2-D examined scenarios.

	0.9 GHz	**1 GHz**	**1.1 GHz**	**1.2 GHz**
CST h-stroke	0.4717	0.4586	0.4195	0.477
CST i-stroke	1.68	1.66	1.33	1.601
Exp h-stroke	0.4644	0.4687	0.4750	0.4595
Exp i-stroke	1.4939	1.4937	1.5228	1.624

Table 4.6: Relative errors of the permittivity in the target area for the 3-D examined scenarios.

	0.9 GHz	**1 GHz**	**1.1 GHz**	**1.2 GHz**
CST h-stroke	0.1236	0.1271	0.244	0.1906
CST i-stroke	0.9714	1.0099	1.3393	1.2201
Exp h-stroke	0.096	0.1081	0.1241	0.1277
Exp i-stroke	1.4114	1.3885	1.3826	1.29

Table 4.7: Relative errors of the conductivity in the target area for the 3-D examined scenarios.

	0.9 GHz	**1 GHz**	**1.1 GHz**	**1.2 GHz**
CST h-stroke	0.4524	0.438	0.373	0.4482
CST i-stroke	2.2492	1.7673	1.7737	3.09
Exp h-stroke	0.6892	0.6587	0.6166	0.4834
Exp i-stroke	2.7054	2.7975	3.1453	3.1617

4.6 Initial Validation of 3-D DBIM-TwIST to an Alternative Microwave Medical Diagnostic System

The fourth secondment in the Polytechnic University of Turin (POLITO) was conducted virtually due to the travel restrictions imposed as a response to the pandemic. The objective of the secondment was to adapt DBIM-TwIST to the EM device of POLITO for cerebrovascular disease imaging.

Consequently, we performed simulations using the POLITO phantom and system presented in [162],[156] and shown in Fig. 4.23. The phantom consisted of a realistic geometrical model extracted from MRI data with the dielectric properties of average

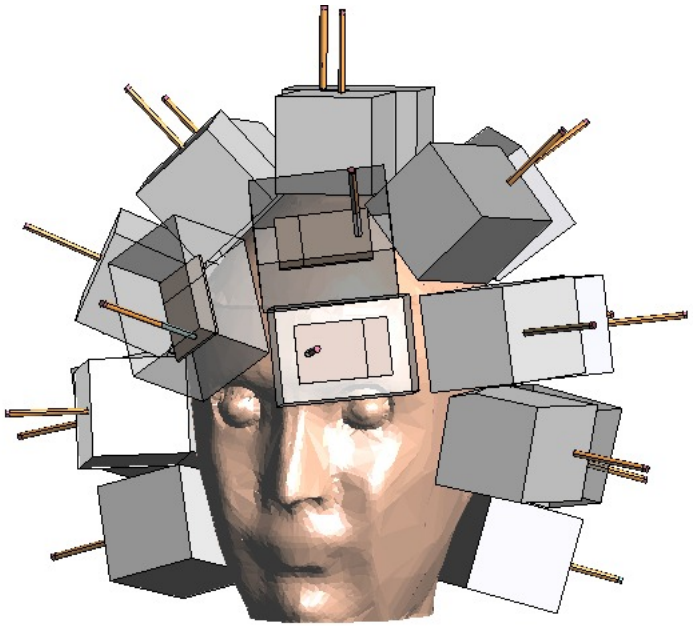

Figure 4.23: The POLITO phantom surrounded by 24 antennas immersed in G35 bricks.

brain at 1 GHz (E_r= 45.4, σ = 0.77 S/m). The stroke was modeled by inserting into the phantom, a cylinder with a diameter of 30 mm which was filled with the dielectric properties of the hemorrhagic stroke (E_r= 63.41, σ = 1.576 S/m). The phantom was surrounded by a 3-D configuration of 24 monopole antennas embedded into a semi-solid dielectric brick made by a mixture of urethane rubber and graphite powder [163]. The scattering matrices (WT and NT scenario) were calculated by POLITO's in-house full-wave software, based on the FEM, resulting into two 24×24 matrices of S-parameters.

To evaluate the performance of DBIM-TwIST for a different imaging prototype, we reconstructed the data acquired by the NT and WT simulations for hemorrhagic stroke. We used the FDTD method as the forward solver to obtain the 3-D fields. The background model which is shown in Fig. 4.24, contained a 3-D Matlab mask extracted by the CAD file of the phantom, with the dielectric properties of average brain (E_r= 45.3, σ = 0.7 S/m) and was surrounded by point sources located at the same position as in the simulation. We applied DBIM-TwIST algorithm for single frequency at 1 GHz.

The number of the voxels in the reconstruction domain was 67300 for 3-D version of the algorithm and the computation time for the 3-D forward solver for each antenna was approximately 17 seconds.

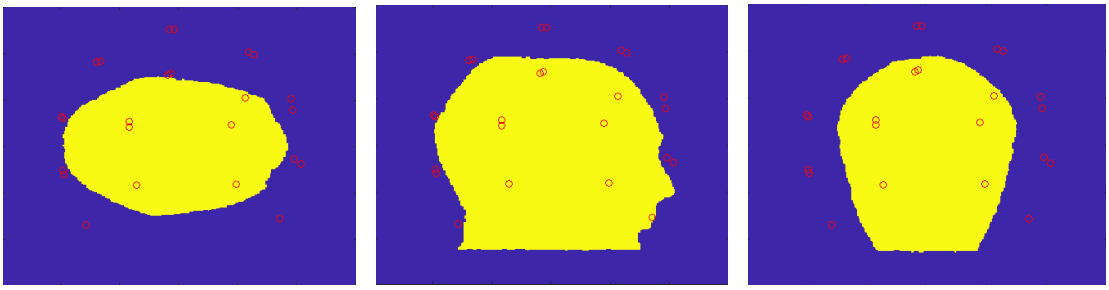

(a) (b) (c)

Figure 4.24: The sagittal, axial and coronal planes at Y-Z, X-Z and X-Y slices of the forward model.

As the main objective of the secondment was to adapt DBIM-TwIST to the MWI device of POLITO for brain stroke detection, we built the model by adding more information in every simulation. Initially, we conducted some preliminary numerical simulations using our FDTD solver. As the measured data that were used for these reconstructions, were obtained from the FDTD solver, they were not different from the background data which were also calculated with FDTD, therefore an "inverse crime" occurred. We examined two scenarios: First, we surrounded the POLITO model with the average dispersive dielectric properties of 90% glycerol-water (E_r= 16.86, σ = 0.32 S/m), and then we conducted the same simulation by using G35's dielectric properties at 1 GHz (E_r= 18.5, σ = 0.2 S/m). Fig. 4.25 presents the sagittal, axial and coronal planes at y-z, x-z and x-y slices, as reconstructed by the 3-D DBIM-TwIST at 1 GHz, for the case of h-stroke with inverse crime surrounded by the dielectric properties of 90% glycerol-water and G35, respectively. As it was expected and since there was no mismatch between the measured and the forward data, the reconstruction results were very good and no errors were observed. Namely, the estimated values of the real permittivity ϵ' at 1 GHz were $\epsilon' = 48.35$ and $\epsilon' = 47.36$ for the two different immersion

liquids.

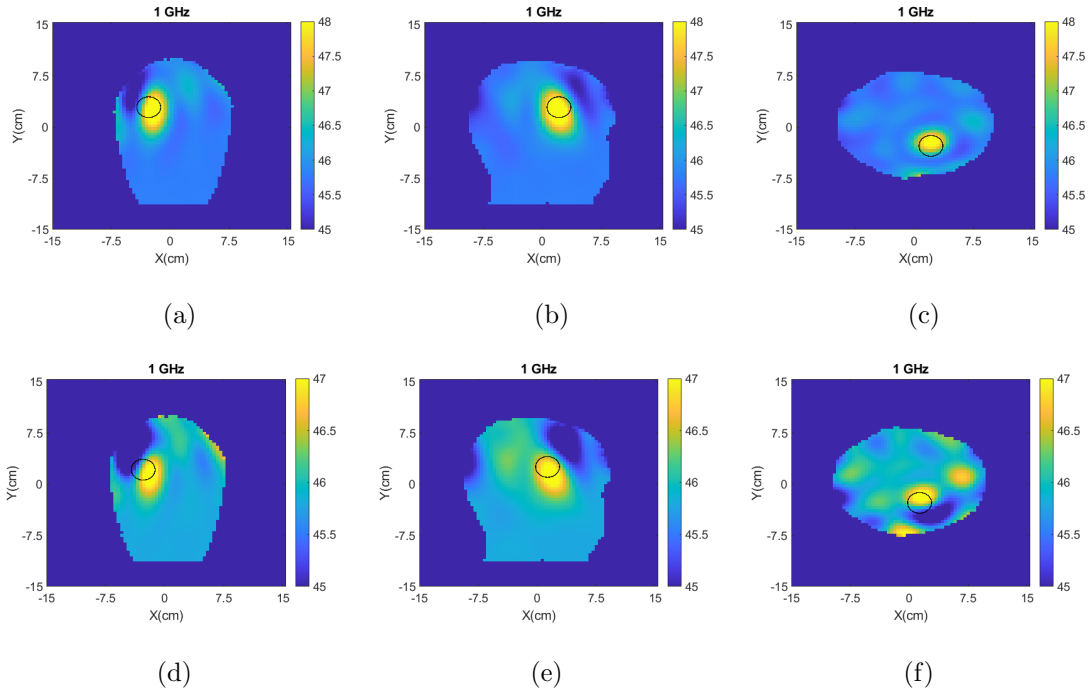

Figure 4.25: Top line: Simulation reconstructed results of the permittivity for h-stroke using 3-D DBIM-TwIST when the POLITO phantom is immersed in 90% glycerol-water mixture; Bottom line: Simulation results of the permittivity for h-stroke using 3-D DBIM-TwIST when the POLITO phantom is immersed in G35 mixture.

Then, we used POLITO's FEM solver to acquire measured data for three scenarios: When the head model and the antennas are immersed in a) 90% glycerol-water mixture; b) G35 immersion liquid and c) when the antennas are placed inside the G35 blocks of Fig. 4.23. Fig. 4.26 shows the sagittal, axial and coronal planes at Y-Z, X-Z and X-Y slices, as reconstructed by the 3-D DBIM-TwIST at 1 GHz, for the examined cases. We observed that h-stroke was successfully located and reconstructed in every scenario but some artifacts and a small offset from the target location were observed for the scenario when antennas were immersed in the G35 blocks. This was expected as the algorithm did not take into account the air between the G35 bricks. The results of Fig. 4.26 estimate the values of permittivity ϵ' at 1 GHz as $\epsilon' = 47.94$, $\epsilon' = 46.73$

and $\epsilon' = 45.95$ for glycerol-water matching medium, G35 mixture without bricks and G35 antenna bricks, respectively. Overall, the obtained results have revealed the good performance of DBIM-TwIST with a different imaging prototype and future research will be focused on further assessing DBIM-TwIST for both h- and i-stroke and different imaging systems.

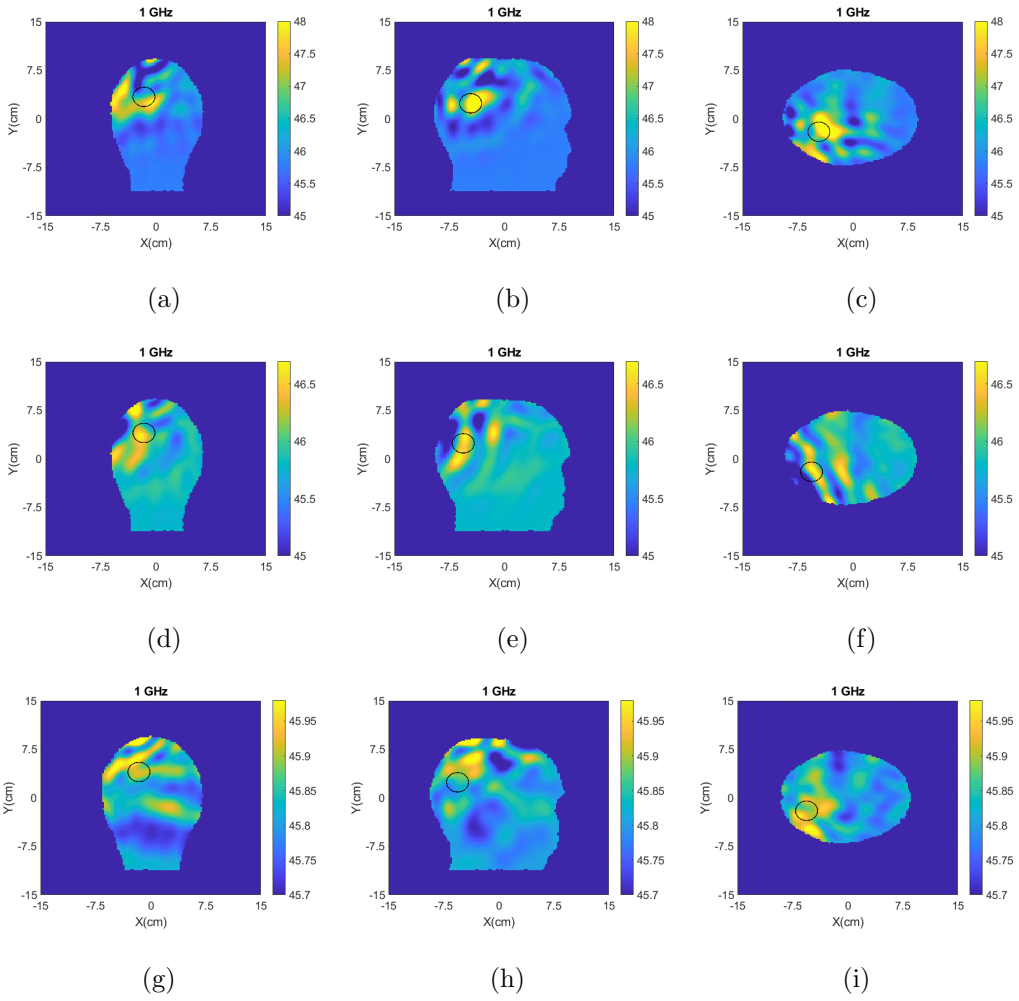

Figure 4.26: Simulation reconstructed results of the permittivity for h-stroke using 3-D DBIM-TwIST when the POLITO phantom is immersed in 90% glycerol-water mixture (top line); when the POLITO phantom is immersed in G35 mixture (middle line); when the POLITO phantom is immersed in G35 mixture (bottom line).

4.7 Conclusion

In this chapter, we have examined the performance of a MWI setup for the problem of brain stroke detection and differentiation, using the 2-D and 3-D DBIM-TwIST algorithm and a novel, anatomically accurate, multi-layer head phantom. We called this a Zubal model, as it extends a slice from the Zubal numerical phantom to create 3-D moulds that can be combined to construct the final phantom. We note that the phantom is an extended 2-D cut of the head surrounded by a 2-D configuration of antennas, which was confined to a ring by our experimental setup. This phantom and antenna configuration allows a 2-D inversion to produce results of comparable accuracy. However, it is still critical to validate the 3-D algorithm for such scenarios by comparing it with 2-D images, and this has been the main objective of this study. Preliminary simplified simulations in which the antenna array contains more than one ring, in Section 4.3, have shown the superior performance of the 3-D algorithm.

The phantom mimics the high dielectric difference in the brain tissues by comprising gelatine-based phantoms that mimic the dielectric permittivity of various head tissues. Importantly, we used a construction process that eliminates the presence of plastic in the phantom, which would distort the signals processed by our algorithm.

We placed the phantom in our experimental prototype as well as in a CST model that simulates the experiment. CST simulation results indicated that we are able to successfully localize and differentiate stroke targets by estimating their dielectric properties. Our measured data reconstructions confirmed that stroke detection and differentiation are more challenging with experimental data. Results for the hemorrhagic-like target were more accurate than for the ischemic-like target as the latter has a lower dielectric contrast with the surrounding brain matter. In accordance with previous work [159], we observed that permittivity estimation is more accurate than conductivity estimation. Importantly, we also observed that the differences in the dielectric estimation of i-stoke and h-stroke targets is higher if reconstructions are performed with the 3-D DBIM-TwIST algorithm.

We also note that our calibration method relies on the signal difference between the experimental and the simulated NT scenarios. Section 4.2 has examined what prior knowledge is needed to successfully differentiate the two types of stroke when using a complex model, and whether an improved forward model could produce better image quality. Our preliminary results indicated that the addition of thin head layers in the forward model is not critical for the successful reconstruction of the target's dielectric properties.

The purpose of this study was to experimentally validate our 2-D and 3-D DBIM-TwIST algorithms for stroke detection and differentiation, but also to further assess experimentally the performance of the 3-D algorithm for the examined application. For some of the studied scenarios, the 2-D DBIM-TwIST can lead to more accurate reconstructions. This is because the 2-D inverse problem approximates well the 3-D problem in these cases, and it is less ill-posed than the 3-D inverse problem as it contains a much smaller number of unknowns. However, as shown by our numerical results with 2 rings of antennas and a smaller target placed between the two rings, the 3-D inverse algorithm can provide more accurate results for problems with significant variation along all three dimensions, as with the case of brain imaging. We also present the initial results acquired during the secondment at POLITO related to the validation of DBIM-TwIST in an alternative imaging prototype. For the alternative imaging prototype, the results showed that DBIM-TwIST performed well with a new imaging prototype, and future work will be concentrated on further evaluating DBIM-TwIST for both h- and i-stroke and other imaging prototypes.

Chapter 5

Conclusions and Future Work

5.1 Summary of Contributions

The main aim of this thesis was to incorporate computationally efficient MWI algorithms into medical diagnostic devices, by incorporating and validating both 2-D and 3-D DBIM-TwIST into the microwave imaging prototype for brain stroke detection developed by King's College London. This goal was a critical objective for the EU project EMERALD, which has motivated this work. In addition, secondary objectives, included the incorporation of DBIM-TwIST into specific diagnostic applications developed by other EMERALD groups.

We constructed two sets of head phantoms, one simplified and one anatomically accurate multi-layered head phantom with the aim to experimentally validate the microwave tomography prototype for brain stroke detection and classification. The main contributions in this thesis are as follows.

- A comprehensive validation study of the 2-D DBIM-TwIST algorithm for brain stroke detection and classification using simulation and experimental data from a MWT prototype and developed gel-based phantoms has been presented. To the best of our knowledge, this was the first study that experimentally differentiated between hemorrhagic and ischemic strokes based on the estimation of their

dielectric properties, in a wide frequency range.

- The performance assessment of DBIM-TwIST, using an anthropomorphic brain phantom has been presented and discussed. We assessed the reconstruction results from measurements on a 3-D-printed anthropomorphic head model, containing a cylindrical target simulating the bleeding during a hemorrhagic stroke. The imaging results showed that the target was detected and localized accurately using a realistic head phantom.

- Our results demonstrated that we are able to detect the stroke target in scenarios where the initial guess of the inverse problem is only an approximation of the true experimental phantom.

- The implementation of the 3-D DBIM-TwIST algorithm has been assessed successfully for a 3-D MWI problem using realistic simulation scenarios mimicking brain stroke.

- We examined the impact of prior information (or "initial guess") for calibrating a microwave tomography system for brain stroke detection and differentiation, using a multi-layered, anatomically complex head phantom. Our results demonstrated that the addition of thin head tissue layers in the forward model is not critical for the successful reconstruction of the target's dielectric properties.

- A novel multi-layer anatomically accurate head phantom has been designed and prepared using gelatine-based tissue mimicking materials. The performance of the 2-D and 3-D implementations of the DBIM-TwIST algorithm has been compared in a systematic manner using CST simulated and experimentally measured data. This is the first validation study of a MWI algorithm that detects and differentiates two types of strokes, using an anatomically accurate multi-layered head phantom in a wide frequency range.

- We developed, presented and discussed a novel semi-flexible and rigid composite material as a matching medium for medical microwave diagnostic systems.
- Finally, we validated the 3-D DBIM-TwIST algorithm for an alternative MWI prototype for 3-D brain stroke imaging during the secondment in POLITO.

5.2 Future Work

5.2.1 Further validation of 3-D DBIM-TwIST

We have assessed the performance of a MWI setup for the problem of brain stroke detection and differentiation using the 2-D and 3-D DBIM-TwIST algorithm and a novel, anatomically accurate, multi-layer head phantom. This configuration led to reconstruction results of a comparable accuracy. As in a clinical scenario we will not be able to know the exact location of the stroke, future work should further validate 3-D DBIM-TwIST, as well as compare its performance to the 2-D version of the algorithm for more realistic scenarios including a 3-D array of antennas and a target which is not aligned with the antennas' heights. Specifically for the 3-D version of the algorithm, various optimisation techniques like optimised initial guess and MWIFH approach, which has demonstrated a distinct improvement of the reconstructed images, can be additionally applied and assessed. Pre-processing methods to discard data which are associated with measurement errors can also improve performance.

5.2.2 Calibration method

Our calibration method relied on the signal difference between the experimental and the simulated NT scenarios. In our work, we have examined the impact of prior information on calibrating a microwave tomography system for brain stroke detection and differentiation. Our preliminary results showed that the addition of head tissue layers such as CSF in the forward model was not vital for the successful reconstruction of

the target's dielectric properties. As expected, however, we achieved more accurate results with the multi-layer initial guess in challenging cases such as detecting an ischemic stroke-like target in the presence of a six-layers Zubal head phantom. This is counter-intuitive, but it may be attributed to the fact that there is a mismatch in the dielectric values between the CST multi-layer model and the Debye models used by our FDTD solver. These results suggest that calibrating with a head phantom that models as many brain tissues as possible may not be preferable for detecting stroke, due to possible mismatches between the true and modeled properties of these tissues. We note, however, that this was only a preliminary study that must also be confirmed experimentally, which is one of our future work objectives.

As an exact NT model is not realistic for clinical scenarios, there is a need to further examine if calibrating with an accurate approximate NT scenario compared to a full NT scenario is feasible. This could be feasible by applying a reference signal measured from a complex, inhomogeneous reference phantom and should be further explored in the future.

5.2.3 Solid and Flexible Matching Medium for MWI Systems

As we noted in the previous chapters, an efficient matching medium minimizes reflection signals and boosts transmitted power to human tissue in a microwave-based medical imaging system, improving the quality of the reconstructed image and, consequently, the diagnostic system's accuracy. A solid and flexible lossless matching medium, like the one presented in Chapter 3, improves the transmission of EM signals, which can increase the precision of diagnostic systems. If we need the medium to be lossy, as in some MWT systems, salt can offer a simple way to achieve this and will be explored into in further research. Additionally, whereas the majority of matching media suggested in the literature are liquid, a matching medium which is semi-solid in its final stages of manufacture can be fabricated to support conformal arrays in applications for MWI. Future work should also be focused on investigating more in-depth the materials used

to prepare the semi-solid mediums. Initially, the performance of the antenna immersed in this material must be assessed, followed by comparing imaging results with those of a system which includes antennas immersed in glycerol-water mixtures.

Bibliography

[1] K. K. Shung, M. B. Smith, and B. M. Tsui, "Principles of medical imaging," 2015.

[2] R. Chandra, H. Zhou, I. Balasingham, and R. M. Narayanan, "On the opportunities and challenges in microwave medical sensing and imaging," *IEEE transactions on biomedical engineering*, vol. 62, no. 7, pp. 1667–1682, 2015.

[3] M. Hopfer, R. Planas, A. Hamidipour, T. Henriksson, and S. Semenov, "Electromagnetic tomography for detection, differentiation, and monitoring of brain stroke: A virtual data and human head phantom study.," *IEEE Antennas and Propagation Magazine*, vol. 59, no. 5, pp. 86–97, 2017.

[4] Y.-H. Shao, K. Tsai, S. Kim, Y.-J. Wu, and K. Demissie, "Exposure to tomographic scans and cancer risks," *JNCI cancer spectrum*, vol. 4, no. 1, p. pkz072, 2020.

[5] R. Benny, T. A. Anjit, and P. Mythili, "An overview of microwave imaging for breast tumor detection," *Progress In Electromagnetics Research B*, vol. 87, pp. 61–91, 2020.

[6] R. C. Heros, "Stroke: early pathophysiology and treatment. summary of the fifth annual decade of the brain symposium.," *Stroke*, vol. 25, no. 9, pp. 1877–1881, 1994.

[7] L. Alon and S. Dehkharghani, "A stroke detection and discrimination framework using broadband microwave scattering on stochastic models with deep learning," *arXiv preprint arXiv:2104.06543*, 2021.

[8] P. M. Meaney, M. W. Fanning, D. Li, S. P. Poplack, and K. D. Paulsen, "A clinical prototype for active microwave imaging of the breast," *IEEE Transactions on Microwave Theory and Techniques*, vol. 48, no. 11, pp. 1841–1853, 2000.

[9] J. A. Tobon Vasquez, R. Scapaticci, G. Turvani, G. Bellizzi, D. O. Rodriguez-Duarte, N. Joachimowicz, B. Duchêne, E. Tedeschi, M. R. Casu, L. Crocco, *et al.*, "A prototype microwave system for 3d brain stroke imaging," *Sensors*, vol. 20, no. 9, p. 2607, 2020.

[10] P. M. Meaney, M. W. Fanning, T. Raynolds, C. J. Fox, Q. Fang, C. A. Kogel, S. P. Poplack, and K. D. Paulsen, "Initial clinical experience with microwave breast imaging in women with normal mammography," *Academic radiology*, vol. 14, no. 2, pp. 207–218, 2007.

[11] J.-C. Bolomey and L. Jofre, "Three decades of active microwave imaging achievements, difficulties and future challenges," in *2010 IEEE International Conference on Wireless Information Technology and Systems*, pp. 1–4, IEEE, 2010.

[12] J. D. Shea, P. Kosmas, S. C. Hagness, and B. D. Van Veen, "Three-dimensional microwave imaging of realistic numerical breast phantoms via a multiple-frequency inverse scattering technique," *Medical physics*, vol. 37, no. 8, pp. 4210–4226, 2010.

[13] P. Meaney, M. Fanning, T. Zhou, A. Golnabi, S. Geimer, and K. Paulsen, "Clinical microwave breast imaging—2d results and the evolution to 3d," in *2009 International Conference on Electromagnetics in Advanced Applications*, pp. 881–884, IEEE, 2009.

[14] D. O. Rodriguez-Duarte, C. Origlia, J. A. T. Vasquez, R. Scapaticci, L. Crocco, and F. Vipiana, "Experimental assessment of real-time brain stroke monitoring via a microwave imaging scanner," *IEEE Open Journal of Antennas and Propagation*, 2022.

[15] N. AlSawaftah, S. El-Abed, S. Dhou, and A. Zakaria, "Microwave imaging for early breast cancer detection: Current state, challenges, and future directions," *Journal of Imaging*, vol. 8, no. 5, p. 123, 2022.

[16] B. M. Moloney, P. F. McAnena, S. M. Abd Elwahab, A. Fasoula, L. Duchesne, J. D. G. Cano, C. Glynn, A. O'Connell, R. Ennis, A. J. Lowery, *et al.*, "Microwave imaging in breast cancer–results from the first-in-human clinical investigation of the wavelia system," *Academic Radiology*, vol. 29, pp. S211–S222, 2022.

[17] J. T. Vasquez, D. Rodriguez-Duarte, C. Origlia, G. Turvani, R. Scapaticci, M. Casu, L. Crocco, and F. Vipiana, "Microwave imaging device prototype for brain stroke 3d monitoring," in *2022 International Workshop on Antenna Technology (iWAT)*, pp. 200–202, IEEE, 2022.

[18] T. Singh, B. Ninkovic, M. Tasic, M. N. Stevanovic, and B. Kolundzija, "Tools and strategies for 3d em modeling and design of microwave imaging systems for medical applications," in *Computational Intelligence and Image Processing in Medical Applications*, pp. 297–314, World Scientific, 2022.

[19] W.-K. Park, "Real-time detection of small anomaly from limited-aperture measurements in real-world microwave imaging," *Mechanical Systems and Signal Processing*, vol. 171, p. 108937, 2022.

[20] C. Dachena, A. Fedeli, A. Fanti, M. B. Lodi, G. Fumera, M. Pastorino, and A. Randazzo, "A microwave imaging technique based on artificial neural networks for neck tumors detection," in *2022 16th European Conference on Antennas and Propagation (EuCAP)*, pp. 1–5, IEEE, 2022.

[21] F. M. Saraskanroud and I. Jeffrey, "Hybrid approaches in microwave imaging using quantitative time-and frequency-domain algorithms," *IEEE Transactions on Computational Imaging*, vol. 8, pp. 121–132, 2022.

[22] B. M. Moloney, D. O'Loughlin, S. Abd Elwahab, and M. J. Kerin, "Breast cancer detection—a synopsis of conventional modalities and the potential role of microwave imaging," *Diagnostics*, vol. 10, no. 2, p. 103, 2020.

[23] B. M. Moloney, P. F. McAnena, S. M. Abd Elwahab, A. Fasoula, L. Duchesne, J. D. G. Cano, C. Glynn, A. O'Connell, R. Ennis, A. J. Lowery, *et al.*, "Microwave imaging in breast cancer–results from the first-in-human clinical investigation of the wavelia system," *Academic Radiology*, vol. 29, pp. S211–S222, 2022.

[24] C. Estatico, A. Fedeli, M. Pastorino, and A. Randazzo, "Microwave imaging by means of lebesgue-space inversion: An overview," *Electronics*, vol. 8, no. 9, p. 945, 2019.

[25] W. Shao and T. McCollough, "Advances in microwave near-field imaging: Prototypes, systems, and applications," *IEEE microwave magazine*, vol. 21, no. 5, pp. 94–119, 2020.

[26] A. T. Mobashsher and A. Abbosh, "On-site rapid diagnosis of intracranial hematoma using portable multi-slice microwave imaging system," *Scientific reports*, vol. 6, no. 1, pp. 1–17, 2016.

[27] L. E. Larsen and J. H. Jacobi, "Medical applications of microwave imaging," tech. rep., INSTITUTE OF ELECTRICAL AND ELECTRONICS ENGINEERS INC NEW YORK, 1985.

[28] J. H. Jacobi and L. E. Larsen, "Microwave interrogation of dielectric targets. part ii: By microwave time delay spectroscopy," *Medical physics*, vol. 5, no. 6, pp. 509–513, 1978.

[29] P. M. Meaney, K. D. Paulsen, A. Hartov, and R. K. Crane, "An active microwave imaging system for reconstruction of 2-d electrical property distributions," *IEEE Transactions on Biomedical Engineering*, vol. 42, no. 10, pp. 1017–1026, 1995.

[30] P. M. Meaney, K. D. Paulsen, and T. P. Ryan, "Two-dimensional hybrid element image reconstruction for tm illumination," *IEEE transactions on antennas and propagation*, vol. 43, no. 3, pp. 239–247, 1995.

[31] P. M. Meaney, K. D. Paulsen, A. Hartov, and R. Crane, "Microwave imaging for tissue assessment: Initial evaluation in multitarget tissue-equivalent phantoms," *IEEE Transactions on Biomedical Engineering*, vol. 43, no. 9, pp. 878–890, 1996.

[32] R. C. Conceição, J. J. Mohr, M. O'Halloran, *et al.*, *An introduction to microwave imaging for breast cancer detection*. Springer, 2016.

[33] D. O'Loughlin, M. O'Halloran, B. M. Moloney, M. Glavin, E. Jones, and M. A. Elahi, "Microwave breast imaging: Clinical advances and remaining challenges," *IEEE Transactions on Biomedical Engineering*, vol. 65, no. 11, pp. 2580–2590, 2018.

[34] S. P. Poplack, T. D. Tosteson, W. A. Wells, B. W. Pogue, P. M. Meaney, A. Hartov, C. A. Kogel, S. K. Soho, J. J. Gibson, and K. D. Paulsen, "Electromagnetic breast imaging: results of a pilot study in women with abnormal mammograms," *Radiology*, vol. 243, no. 2, pp. 350–359, 2007.

[35] C. Yu, M. Yuan, J. Stang, E. Bresslour, R. T. George, G. A. Ybarra, W. T. Joines, and Q. H. Liu, "Active microwave imaging ii: 3-d system prototype and image reconstruction from experimental data," *IEEE Transactions on Microwave Theory and Techniques*, vol. 56, no. 4, pp. 991–1000, 2008.

[36] E. Porter, M. Coates, and M. Popović, "An early clinical study of time-domain microwave radar for breast health monitoring," *IEEE Transactions on Biomedical Engineering*, vol. 63, no. 3, pp. 530–539, 2015.

[37] M. Persson, A. Fhager, H. D. Trefná, Y. Yu, T. McKelvey, G. Pegenius, J.-E. Karlsson, and M. Elam, "Microwave-based stroke diagnosis making global prehospital thrombolytic treatment possible," *IEEE Transactions on Biomedical Engineering*, vol. 61, no. 11, pp. 2806–2817, 2014.

[38] S. Candefjord, J. Winges, A. A. Malik, Y. Yu, T. Rylander, T. McKelvey, A. Fhager, M. Elam, and M. Persson, "Microwave technology for detecting traumatic intracranial bleedings: tests on phantom of subdural hematoma and numerical simulations," *Medical & biological engineering & computing*, vol. 55, no. 8, pp. 1177–1188, 2017.

[39] D. Cook, H. Brown, I. Widanapathirana, D. Shah, J. Walsham, A. Trakic, G. Zhu, A. Zamani, L. Guo, A. Brankovic, *et al.*, "Case report: Preliminary images from an electromagnetic portable brain scanner for diagnosis and monitoring of acute stroke," *Frontiers in neurology*, p. 2016, 2021.

[40] *Medfield*. Available at https://www.medfielddiagnostics.com/en/.

[41] *EMTensor*. Available at https://www.emtensor.com/.

[42] *EMVision*. Available at https://emvision.com.au/.

[43] N. K. Nikolova, *Introduction to microwave imaging*. Cambridge University Press, 2017.

[44] M. Pastorino, *Microwave imaging*, vol. 208. John Wiley & Sons, 2010.

[45] S. S. Ahmed, A. Schiessl, F. Gumbmann, M. Tiebout, S. Methfessel, and L.-P. Schmidt, "Advanced microwave imaging," *IEEE microwave magazine*, vol. 13, no. 6, pp. 26–43, 2012.

[46] J.-C. Bolomey, "Recent european developments in active microwave imaging for industrial, scientific, and medical applications," *IEEE Transactions on microwave theory and techniques*, vol. 37, no. 12, pp. 2109–2117, 1989.

[47] S. C. Hagness, E. C. Fear, and A. Massa, "Guest editorial: Special cluster on microwave medical imaging," *IEEE Antennas and wireless propagation letters*, vol. 11, pp. 1592–1597, 2012.

[48] K. R. Foster, H. P. Schwan, *et al.*, "Dielectric properties of tissues," *CRC handbook of biological effects of electromagnetic fields*, pp. 27–96, 1986.

[49] J. L. Schepps and K. R. Foster, "The uhf and microwave dielectric properties of normal and tumour tissues: variation in dielectric properties with tissue water content," *Physics in Medicine & Biology*, vol. 25, no. 6, p. 1149, 1980.

[50] N. H. Jamali, K. H. Ping, S. Sahrani, and T. Takenaka, "Image reconstruction based on combination of inverse scattering technique and total variation regularization method," *Indonesian Journal of Electrical Engineering and Computer Science*, vol. 5, no. 3, pp. 569–576, 2017.

[51] N. K. Nikolova, "Microwave biomedical imaging," *Wiley Encyclopedia of Electrical and Electronics Engineering*, pp. 1–22, 1999.

[52] R. K. Amineh, M. Ravan, A. Trehan, and N. K. Nikolova, "Near-field microwave imaging based on aperture raster scanning with tem horn antennas," *IEEE Transactions on Antennas and Propagation*, vol. 59, no. 3, pp. 928–940, 2010.

[53] A. Moradpour, O. Karadima, I. Alic, M. Ragulskis, F. Kienberger, and P. Kosmas, "Development of a solid and flexible matching medium for microwave medical diagnostic systems," *Diagnostics*, vol. 11, no. 3, p. 550, 2021.

[54] R. Scapaticci, J. Tobon, G. Bellizzi, F. Vipiana, and L. Crocco, "Design and numerical characterization of a low-complexity microwave device for brain stroke monitoring," *IEEE Transactions on Antennas and Propagation*, vol. 66, no. 12, pp. 7328–7338, 2018.

[55] V. Zhurbenko, "Challenges in the design of microwave imaging systems for breast cancer detection," *Advances in Electrical and Computer Engineering*, vol. 11, no. 1, pp. 91–96, 2011.

[56] R. Scapaticci, L. Di Donato, I. Catapano, and L. Crocco, "A feasibility study on microwave imaging for brain stroke monitoring," *Progress In Electromagnetics Research B*, vol. 40, pp. 305–324, 2012.

[57] A. Abbosh, "Microwave systems for head imaging: Challenges and recent developments," in *2013 IEEE MTT-S International Microwave Workshop Series on RF and Wireless Technologies for Biomedical and Healthcare Applications (IMWS-BIO)*, pp. 1–3, IEEE, 2013.

[58] N. G. McCrum, B. E. Read, and G. Williams, "Anelastic and dielectric effects in polymeric solids," 1967.

[59] J. P. Runt, J. J. Fitzgerald, *et al.*, *Dielectric spectroscopy of polymeric materials*. American Chemical Society, 1997.

[60] F. Kremer, "Dielectric spectroscopy–yesterday, today and tomorrow," *Journal of Non-crystalline solids*, vol. 305, no. 1-3, pp. 1–9, 2002.

[61] A. La Gioia, E. Porter, I. Merunka, A. Shahzad, S. Salahuddin, M. Jones, and M. O'Halloran, "Open-ended coaxial probe technique for dielectric measurement of biological tissues: Challenges and common practices," *Diagnostics*, vol. 8, no. 2, p. 40, 2018.

[62] N. Ištuk, F. Kienberger, E. Porter, M. O'Halloran, A. Santorelli, I. Alić, M. Ragulskis, A. Moradpour, and M. Kasper, "Fast measurements of dielectric properties with small size microwave transceiver," in *2020 14th European Conference on Antennas and Propagation (EuCAP)*, pp. 1–5, 2020.

[63] V. Teppati, A. Ferrero, and M. Sayed, *Modern RF and microwave measurement techniques*. Cambridge University Press, 2013.

[64] C. Gabriel, "Compilation of the dielectric properties of body tissues at rf and microwave frequencies.," 1996.

[65] S. Gabriel, R. Lau, and C. Gabriel, "The dielectric properties of biological tissues: Iii. parametric models for the dielectric spectrum of tissues," *Physics in medicine & biology*, vol. 41, no. 11, p. 2271, 1996.

[66] M. Lazebnik, L. McCartney, D. Popovic, C. B. Watkins, M. J. Lindstrom, J. Harter, S. Sewall, A. Magliocco, J. H. Booske, M. Okoniewski, *et al.*, "A large-scale study of the ultrawideband microwave dielectric properties of normal breast tissue obtained from reduction surgeries," *Physics in medicine & biology*, vol. 52, no. 10, p. 2637, 2007.

[67] T. Sugitani, S.-i. Kubota, S.-i. Kuroki, K. Sogo, K. Arihiro, M. Okada, T. Kadoya, M. Hide, M. Oda, and T. Kikkawa, "Complex permittivities of breast tumor tissues obtained from cancer surgeries," *Applied Physics Letters*, vol. 104, no. 25, p. 253702, 2014.

[68] S. Di Meo, P. Espin-Lopez, A. Martellosio, M. Pasian, M. Bozzi, L. Peregrini, A. Mazzanti, F. Svelto, P. Summers, G. Renne, *et al.*, "Experimental validation of the dielectric permittivity of breast cancer tissues up to 50 ghz," in *2017 IEEE MTT-S International Microwave Workshop Series on Advanced Materials and Processes for RF and THz Applications (IMWS-AMP)*, pp. 1–3, IEEE, 2017.

[69] A. Martellosio, M. Pasian, M. Bozzi, L. Perregrini, A. Mazzanti, F. Svelto, P. E. Summers, G. Renne, L. Preda, and M. Bellomi, "Dielectric properties characterization from 0.5 to 50 ghz of breast cancer tissues," *IEEE Transactions on Microwave Theory and Techniques*, vol. 65, no. 3, pp. 998–1011, 2016.

[70] B. Amin, M. A. Elahi, A. Shahzad, E. Porter, B. McDermott, and M. O'Halloran, "Dielectric properties of bones for the monitoring of osteoporosis," *Medical & biological engineering & computing*, vol. 57, no. 1, pp. 1–13, 2019.

[71] A. P. O'rourke, M. Lazebnik, J. M. Bertram, M. C. Converse, S. C. Hagness, J. G. Webster, and D. M. Mahvi, "Dielectric properties of human normal, malignant and cirrhotic liver tissue: in vivo and ex vivo measurements from 0.5 to 20 ghz using a precision open-ended coaxial probe," *Physics in medicine & biology*, vol. 52, no. 15, p. 4707, 2007.

[72] L. Abdilla, C. Sammut, and L. Z. Mangion, "Dielectric properties of muscle and liver from 500 mhz–40 ghz," *Electromagnetic Biology and Medicine*, vol. 32, no. 2, pp. 244–252, 2013.

[73] L. Farrugia, P. S. Wismayer, L. Z. Mangion, and C. V. Sammut, "Accurate in vivo dielectric properties of liver from 500 mhz to 40 ghz and their correlation to ex vivo measurements," *Electromagnetic biology and medicine*, vol. 35, no. 4, pp. 365–373, 2016.

[74] N. Ištuk, B. McDermott, E. Porter, A. Santorelli, S. Abedi, M. O'Halloran, N. Joachimowicz, and H. Roussel, "Detailed dielectric characterisation of the heart and great vessels," in *2020 14th European Conference on Antennas and Propagation (EuCAP)*, pp. 1–5, IEEE, 2020.

[75] A. Peyman, S. Holden, S. Watts, R. Perrott, and C. Gabriel, "Dielectric properties of porcine cerebrospinal tissues at microwave frequencies: in vivo, in vitro and systematic variation with age," *Physics in Medicine & Biology*, vol. 52, no. 8, p. 2229, 2007.

[76] G. Schmid, G. Neubauer, and P. R. Mazal, "Dielectric properties of human brain tissue measured less than 10 h postmortem at frequencies from 800 to 2450 mhz," *Bioelectromagnetics: Journal of the Bioelectromagnetics Society, The Society for Physical Regulation in Biology and Medicine, The European Bioelectromagnetics Association*, vol. 24, no. 6, pp. 423–430, 2003.

[77] S. Semenov, T. Huynh, T. Williams, B. Nicholson, and A. Vasilenko, "Dielectric

properties of brain tissue at 1 ghz in acute ischemic stroke: Experimental study on swine.," *Bioelectromagnetics*, vol. 38, no. 2, pp. 158–163, 2016.

[78] L. Crocco, I. Karanasiou, M. L. James, and R. C. Conceição, *Emerging Electromagnetic Technologies for Brain Diseases Diagnostics, Monitoring and Therapy*. Springer, 2018.

[79] V. Mariano, J. A. T. Vasquez, R. Scapaticci, L. Crocco, P. Kosmas, and F. Vipiana, "Comparison of reconstruction algorithms for brain stroke microwave imaging," in *2020 IEEE MTT-S International Microwave Biomedical Conference (IMBioC)*, pp. 1–3, IEEE, 2020.

[80] P. M. Van Den Berg and R. E. Kleinman, "A contrast source inversion method," *Inverse problems*, vol. 13, no. 6, p. 1607, 1997.

[81] M. Bertero and P. Boccacci, *Introduction to inverse problems in imaging*. CRC press, 2020.

[82] M. Salucci, A. Polo, and J. Vrba, "Multi-step learning-by-examples strategy for real-time brain stroke microwave scattering data inversion," *Electronics*, vol. 10, no. 1, p. 95, 2021.

[83] A. Fedeli, V. Schenone, A. Randazzo, M. Pastorino, T. Henriksson, and S. Semenov, "Nonlinear s-parameters inversion for stroke imaging," *IEEE Transactions on Microwave Theory and Techniques*, vol. 69, no. 3, pp. 1760–1771, 2020.

[84] Z. Miao and P. Kosmas, "Multiple-frequency dbim-twist algorithm for microwave breast imaging," *IEEE Transactions on Antennas and Propagation*, vol. 65, no. 5, pp. 2507–2516, 2017.

[85] T. M. Grzegorczyk, P. M. Meaney, P. A. Kaufman, K. D. Paulsen, *et al.*, "Fast 3-d tomographic microwave imaging for breast cancer detection," *IEEE transactions on medical imaging*, vol. 31, no. 8, pp. 1584–1592, 2012.

[86] T. J. Colgan, S. C. Hagness, and B. D. Van Veen, "A 3-d level set method for microwave breast imaging," *IEEE Transactions on Biomedical Engineering*, vol. 62, no. 10, pp. 2526–2534, 2015.

[87] Q. Fang, P. M. Meaney, and K. D. Paulsen, "Viable three-dimensional medical microwave tomography: Theory and numerical experiments," *IEEE transactions on antennas and propagation*, vol. 58, no. 2, pp. 449–458, 2009.

[88] D. Ireland and A. Abbosh, "Modeling human head at microwave frequencies using optimized debye models and fdtd method," *IEEE Transactions on Antennas and Propagation*, vol. 61, no. 4, pp. 2352–2355, 2013.

[89] A. M. Qureshi, Z. Mustansar, and A. Maqsood, "Analysis of microwave scattering from a realistic human head model for brain stroke detection using electromagnetic impedance tomography," *Progress In Electromagnetics Research M*, vol. 52, pp. 45–56, 2016.

[90] P. Lu and P. Kosmas, "Three-dimensional microwave head imaging with gpu-based fdtd and the dbim method," *Manuscript submitted for publication at IEEE Transactions on Computational Imaging*, 2021.

[91] A. Mobashsher, K. Bialkowski, A. Abbosh, and S. Crozier, "Design and experimental evaluation of a non-invasive microwave head imaging system for intracranial haemorrhage detection," *Plos one*, vol. 11, no. 4, p. e0152351, 2016.

[92] I. Merunka, A. Massa, D. Vrba, O. Fiser, M. Salucci, and J. Vrba, "Microwave tomography system for methodical testing of human brain stroke detection approaches," *International Journal of Antennas and Propagation*, vol. 2019, 2019.

[93] S. Y. Semenov and D. R. Corfield, "Microwave tomography for brain imaging: Feasibility assessment for stroke detection," *International Journal of Antennas and Propagation*, vol. 2008, 2008.

[94] A. Bruno, N. Shah, A. E. Akinwuntan, B. Close, and J. A. Switzer, "Stroke size correlates with functional outcome on the simplified modified rankin scale questionnaire," *Journal of Stroke and Cerebrovascular Diseases*, vol. 22, no. 6, pp. 781–783, 2013.

[95] X. Li and S. C. Hagness, "A confocal microwave imaging algorithm for breast cancer detection," *IEEE Microwave and wireless components letters*, vol. 11, no. 3, pp. 130–132, 2001.

[96] I. Craddock, M. Klemm, J. Leendertz, A. Preece, and R. Benjamin, "Development and application of a uwb radar system for breast imaging," in *2008 Loughborough Antennas and Propagation Conference*, pp. 24–27, IEEE, 2008.

[97] S. C. Hagness, A. Taflove, and J. E. Bridges, "Two-dimensional fdtd analysis of a pulsed microwave confocal system for breast cancer detection: Fixed-focus and antenna-array sensors," *IEEE transactions on biomedical engineering*, vol. 45, no. 12, pp. 1470–1479, 1998.

[98] R. Nilavalan, J. Leendertz, I. Craddock, A. Preece, and R. Benjamin, "Numerical analysis of microwave detection of breast tumours using synthetic focussing techniques," in *IEEE Antennas and Propagation Society Symposium, 2004.*, vol. 3, pp. 2440–2443, IEEE, 2004.

[99] S. K. Davis, H. Tandradinata, S. C. Hagness, and B. D. Van Veen, "Ultrawideband microwave breast cancer detection: a detection-theoretic approach using the generalized likelihood ratio test," *IEEE transactions on biomedical engineering*, vol. 52, no. 7, pp. 1237–1250, 2005.

[100] D. Byrne, M. O'Halloran, M. Glavin, and E. Jones, "Data independent radar beamforming algorithms for breast cancer detection," *Progress In Electromagnetics Research*, vol. 107, pp. 331–348, 2010.

[101] L. Xu, X. Xiao, and T. Kikkawa, "Improved beamforming algorithm for imaging reconstruction for early breast cancer detection by uwb," *Journal of Circuits, Systems, and Computers*, vol. 22, no. 10, p. 1340027, 2013.

[102] Q. Li, X. Xiao, H. Song, L. Wang, and T. Kikkawa, "Tumor response extraction based on ensemble empirical mode decomposition for early breast cancer detection by uwb," in *2014 IEEE Biomedical Circuits and Systems Conference (BioCAS) Proceedings*, pp. 97–100, IEEE, 2014.

[103] N. Ghavami, G. Tiberi, D. J. Edwards, and A. Monorchio, "Uwb microwave imaging of objects with canonical shape," *IEEE Transactions on Antennas and Propagation*, vol. 60, no. 1, pp. 231–239, 2011.

[104] N. Ghavami, P. P. Smith, G. Tiberi, D. Edwards, and I. Craddock, "Non-iterative beamforming based on huygens principle for multistatic ultrawide band radar: application to breast imaging," *IET Microwaves, Antennas & Propagation*, vol. 9, no. 12, pp. 1233–1240, 2015.

[105] A. Fedeli, C. Estatico, M. Pastorino, and A. Randazzo, "Microwave detection of brain injuries by means of a hybrid imaging method," *IEEE Open Journal of Antennas and Propagation*, vol. 1, pp. 513–523, 2020.

[106] J. Xu, J. Chen, W. Yu, H. Zhang, F. Wang, W. Zhuang, J. Yang, Z. Bai, L. Xu, J. Sun, *et al.*, "Noninvasive and portable stroke type discrimination and progress monitoring based on a multichannel microwave transmitting–receiving system," *Scientific Reports*, vol. 10, no. 1, pp. 1–13, 2020.

[107] F. Wang, H. Zhang, J. Bao, H. Li, W. Peng, J. Xu, J. Yang, W. Zhuang, X. Ning, L. Xu, *et al.*, "Experimental study on differential diagnosis of cerebral hemorrhagic and ischemic stroke based on microwave measurement," *Technology and Health Care*, vol. 28, no. S1, pp. 289–301, 2020.

[108] G. Zhu, A. Bialkowski, L. Guo, B. Mohammed, and A. Abbosh, "Stroke classification in simulated electromagnetic imaging using graph approaches," *IEEE Journal of Electromagnetics, RF and Microwaves in Medicine and Biology*, vol. 5, no. 1, pp. 46–53, 2020.

[109] X. Chen, Z. Wei, M. Li, and P. Rocca, "A review of deep learning approaches for inverse scattering problems (invited review)," *Progress In Electromagnetics Research*, vol. 167, pp. 67–81, 2020.

[110] D. J. Griffiths, "Introduction to electrodynamics," 2005.

[111] A. Taflove, S. C. Hagness, and M. Piket-May, "Computational electromagnetics: the finite-difference time-domain method," *The Electrical Engineering Handbook*, vol. 3, pp. 629–670, 2005.

[112] K. Yee, "Numerical solution of initial boundary value problems involving maxwell's equations in isotropic media," *IEEE Transactions on antennas and propagation*, vol. 14, no. 3, pp. 302–307, 1966.

[113] S. Salon and M. Chari, *Numerical methods in electromagnetism*. Elsevier, 1999.

[114] A. Taflove, A. Oskooi, and S. G. Johnson, *Advances in FDTD computational electrodynamics: photonics and nanotechnology*. Artech house, 2013.

[115] R. Holland and J. W. Williams, "Total-field versus scattered-field finite-difference codes: A comparative assessment," *IEEE Transactions on Nuclear Science*, vol. 30, no. 6, pp. 4583–4588, 1983.

[116] G. Mur, "Absorbing boundary conditions for the finite-difference approximation of the time-domain electromagnetic-field equations," *IEEE transactions on Electromagnetic Compatibility*, no. 4, pp. 377–382, 1981.

[117] Z.-P. Liao and H. Wong, "A transmitting boundary for the numerical simulation of elastic wave propagation," *International Journal of Soil Dynamics and Earthquake Engineering*, vol. 3, no. 4, pp. 174–183, 1984.

[118] J.-P. Berenger, "A perfectly matched layer for the absorption of electromagnetic waves," *Journal of computational physics*, vol. 114, no. 2, pp. 185–200, 1994.

[119] J. A. Roden and S. D. Gedney, "Convolution pml (cpml): An efficient fdtd implementation of the cfs–pml for arbitrary media," *Microwave and optical technology letters*, vol. 27, no. 5, pp. 334–339, 2000.

[120] M. Kuzuoglu and R. Mittra, "Frequency dependence of the constitutive parameters of causal perfectly matched anisotropic absorbers," *IEEE Microwave and Guided wave letters*, vol. 6, no. 12, pp. 447–449, 1996.

[121] S. Cruciani, V. De Santis, M. Feliziani, and F. Maradei, "Cole-cole vs debye models for the assessment of electromagnetic fields inside biological tissues produced by wideband emf sources," in *2012 Asia-Pacific Symposium on Electromagnetic Compatibility*, pp. 685–688, IEEE, 2012.

[122] P. Debye, "Zur theorie der spezifischen wärmen," *Annalen der Physik*, vol. 344, no. 14, pp. 789–839, 1912.

[123] L.-F. Chen, C. Ong, C. Neo, V. Varadan, and V. K. Varadan, *Microwave electronics: measurement and materials characterization*. John Wiley & Sons, 2004.

[124] T. Wuren, T. Takai, M. Fujii, and I. Sakagami, "Effective 2-debye-pole fdtd model of electromagnetic interaction between whole human body and uwb radiation," *IEEE Microwave and Wireless Components Letters*, vol. 17, no. 7, pp. 483–485, 2007.

[125] K. Chadan, D. Colton, L. Päivärinta, and W. Rundell, *An introduction to inverse scattering and inverse spectral problems*. SIAM, 1997.

[126] W. C. Chew, *Waves and fields in inhomogenous media*, vol. 16. Wiley-IEEE Press, 1995.

[127] M. Born and E. Wolf, *Principles of optics: electromagnetic theory of propagation, interference and diffraction of light*. Elsevier, 2013.

[128] W. C. Chew and J. Lin, "A frequency-hopping approach for microwave imaging of large inhomogeneous bodies," *IEEE Microwave and guided wave letters*, vol. 5, no. 12, pp. 439–441, 1995.

[129] Y. Wang and W. C. Chew, "An iterative solution of the two-dimensional electromagnetic inverse scattering problem," *International Journal of Imaging Systems and Technology*, vol. 1, no. 1, pp. 100–108, 1989.

[130] R. Scapaticci, P. Kosmas, and L. Crocco, "Wavelet-based regularization for robust microwave imaging in medical applications," *IEEE Transactions on Biomedical Engineering*, vol. 62, no. 4, pp. 1195–1202, 2014.

[131] Z. Miao, S. Ahsan, P. Kosmas, J. T. Vasquez, F. Vipiana, M. Casu, and M. Vacca, "Application of the dbim-twist algorithm to experimental microwave imaging data," in *2017 11th European Conference on Antennas and Propagation (EUCAP)*, pp. 1611–1614, IEEE, 2017.

[132] E. Razzicchia, P. Lu, W. Guo, O. Karadima, I. Sotiriou, N. Ghavami, E. Kallos, G. Palikaras, and P. Kosmas, "Metasurface-enhanced antennas for microwave brain imaging," *Diagnostics*, vol. 11, no. 3, p. 424, 2021.

[133] O. Karadima, P. Lu, and P. Kosmas, "Comparison of 2-d and 3-d dbim-twist for brain stroke detection and differentiation," in *2021 15th European Conference on Antennas and Propagation (EuCAP)*, pp. 1–4, IEEE, 2021.

[134] P. Kosmas, J. D. Shea, B. D. Van Veen, and S. C. Hagness, "Three-dimensional microwave imaging of realistic breast phantoms via an inexact gauss-newton al-

gorithm," in *2008 IEEE Antennas and Propagation Society International Symposium*, pp. 1–4, IEEE, 2008.

[135] P. Mojabi and J. LoVetri, "Microwave biomedical imaging using the multiplicative regularized gauss–newton inversion," *IEEE Antennas and Wireless Propagation Letters*, vol. 8, pp. 645–648, 2009.

[136] M. R. Hestenes, E. Stiefel, *et al.*, *Methods of conjugate gradients for solving linear systems*, vol. 49. NBS Washington, DC, 1952.

[137] W. C. Chew and Y.-M. Wang, "Reconstruction of two-dimensional permittivity distribution using the distorted born iterative method," *IEEE transactions on medical imaging*, vol. 9, no. 2, pp. 218–225, 1990.

[138] D. W. Winters, J. D. Shea, P. Kosmas, B. D. Van Veen, and S. C. Hagness, "Three-dimensional microwave breast imaging: Dispersive dielectric properties estimation using patient-specific basis functions," *IEEE transactions on medical imaging*, vol. 28, no. 7, pp. 969–981, 2009.

[139] J. Dongarra and F. Sullivan, "Guest editors introduction to the top 10 algorithms," *Computing in Science & Engineering*, vol. 2, no. 01, pp. 22–23, 2000.

[140] P. L. Combettes and V. R. Wajs, "Signal recovery by proximal forward-backward splitting," *Multiscale Modeling & Simulation*, vol. 4, no. 4, pp. 1168–1200, 2005.

[141] M. A. Figueiredo and R. D. Nowak, "An em algorithm for wavelet-based image restoration," *IEEE Transactions on Image Processing*, vol. 12, no. 8, pp. 906–916, 2003.

[142] K. Bredies, D. A. Lorenz, and P. Maass, "A generalized conditional gradient method and its connection to an iterative shrinkage method," *Computational Optimization and Applications*, vol. 42, no. 2, pp. 173–193, 2009.

[143] I. Daubechies, M. Defrise, and C. De Mol, "An iterative thresholding algorithm for linear inverse problems with a sparsity constraint," *Communications on Pure and Applied Mathematics: A Journal Issued by the Courant Institute of Mathematical Sciences*, vol. 57, no. 11, pp. 1413–1457, 2004.

[144] D. M. Young, *Iterative solution of large linear systems*. Elsevier, 2014.

[145] J. M. Bioucas-Dias and M. A. Figueiredo, "Two-step algorithms for linear inverse problems with non-quadratic regularization," in *2007 IEEE International Conference on Image Processing*, vol. 1, pp. I–105, IEEE, 2007.

[146] G. Bindu, L. Anil, T. Vinu, C. Aanandan, and K. Mathew, "Active microwave imaging for breast cancer detection," 2006.

[147] Z. Miao and P. Kosmas, "Microwave breast imaging based on an optimized two-step iterative shrinkage/thresholding method," in *2015 9th European Conference on Antennas and Propagation (EuCAP)*, pp. 1–4, IEEE, 2015.

[148] S. Ahsan, Z. Guo, Z. Miao, I. Sotiriou, M. Koutsoupidou, E. Kallos, G. Palikaras, and P. Kosmas, "Design and experimental validation of a multiple-frequency microwave tomography system employing the dbim-twist algorithm," *Sensors*, vol. 18, no. 10, p. 3491, 2018.

[149] Z. Miao, P. Kosmas, and S. Ahsan, "Impact of information loss on reconstruction quality in microwave tomography for medical imaging," *Diagnostics*, vol. 8, no. 3, p. 52, 2018.

[150] Z. Guo, S. Ahsan, O. Karadima, I. Sotiriou, and P. Kosmas, "Resolution capabilities of the dbim-twist algorithm in microwave imaging," in *2019 13th European Conference on Antennas and Propagation (EuCAP)*, pp. 1–4, IEEE, 2019.

[151] B. McDermott, E. Porter, A. Santorelli, B. Divilly, L. Morris, M. Jones, B. McGinley, and M. O'Halloran, "Anatomically and dielectrically realistic mi-

crowave head phantom with circulation and reconfigurable lesions," *Progress In Electromagnetics Research B*, vol. 78, pp. 47–60, 2017.

[152] N. Joachimowicz, B. Duchêne, C. Conessa, and O. Meyer, "Anthropomorphic breast and head phantoms for microwave imaging," *Diagnostics*, vol. 8, no. 4, p. 85, 2018.

[153] T. Rydholm, A. Fhager, M. Persson, S. D. Geimer, and P. M. Meaney, "Effects of the plastic of the realistic geeps-l2s-breast phantom," *Diagnostics*, vol. 8, no. 3, p. 61, 2018.

[154] M. Lazebnik, E. L. Madsen, G. R. Frank, and S. C. Hagness, "Tissue-mimicking phantom materials for narrowband and ultrawideband microwave applications," *Physics in Medicine & Biology*, vol. 50, no. 18, p. 4245, 2005.

[155] O. Bucci and T. Isernia, "Electromagnetic inverse scattering: Retrievable information and measurement strategies," *Radio Science*, vol. 32, no. 6, pp. 2123–2137, 1997.

[156] D. O. Rodriguez-Duarte, J. A. Tobon Vasquez, R. Scapaticci, G. Turvani, M. Cavagnaro, M. R. Casu, L. Crocco, and F. Vipiana, "Experimental validation of a microwave system for brain stroke 3-d imaging," *Diagnostics*, vol. 11, no. 7, p. 1232, 2021.

[157] W. Guo, S. Ahsan, M. He, M. Koutsoupidou, and P. Kosmas, "Printed monopole antenna designs for a microwave head scanner," in *2018 18th Mediterranean Microwave Symposium (MMS)*, pp. 384–386, IEEE, 2018.

[158] I. G. Zubal, C. R. Harrell, E. O. Smith, Z. Rattner, G. Gindi, and P. B. Hoffer, "Computerized three-dimensional segmented human anatomy," *Medical physics*, vol. 21, no. 2, pp. 299–302, 1994.

[159] O. Karadima, M. Rahman, I. Sotiriou, N. Ghavami, P. Lu, S. Ahsan, and P. Kosmas, "Experimental validation of microwave tomography with the dbim-twist

algorithm for brain stroke detection and classification," *Sensors*, vol. 20, no. 3, p. 840, 2020.

[160] T. Rydholm, A. Fhager, M. Persson, S. D. Geimer, and P. M. Meaney, "Effects of the plastic of the realistic geeps-l2s-breast phantom," *Diagnostics*, vol. 8, no. 3, 2018.

[161] M. Azghani, P. Kosmas, and F. Marvasti, "Microwave medical imaging based on sparsity and an iterative method with adaptive thresholding," *IEEE transactions on medical imaging*, vol. 34, no. 2, pp. 357–365, 2014.

[162] D. O. Rodriguez-Duarte, J. A. T. Vasquez, R. Scapaticci, L. Crocco, and F. Vipiana, "Assessing a microwave imaging system for brain stroke monitoring via high fidelity numerical modelling," *IEEE Journal of Electromagnetics, RF and Microwaves in Medicine and Biology*, vol. 5, no. 3, pp. 238–245, 2021.

[163] D. O. Rodriguez-Duarte, J. A. T. Vasquez, R. Scapaticci, L. Crocco, and F. Vipiana, "Brick-shaped antenna module for microwave brain imaging systems," *IEEE Antennas and Wireless Propagation Letters*, vol. 19, no. 12, pp. 2057–2061, 2020.

[164] R. J. Luebbers and F. Hunsberger, "Fdtd for nth-order dispersive media," *IEEE transactions on Antennas and Propagation*, vol. 40, no. 11, pp. 1297–1301, 1992.

[165] J. H. Beggs, R. J. Luebbers, K. S. Yee, and K. S. Kunz, "Finite-difference time-domain implementation of surface impedance boundary conditions," *IEEE Transactions on Antennas and propagation*, vol. 40, no. 1, pp. 49–56, 1992.

Appendices

Appendix A

Theory of Finite-Difference Time-Domain Method

A.1 2-D Finite-Difference Time-Domain Method

For a two-dimensional transverse electric (TE) wave, the electric field is constant in the z-direction, therefore the derivative of the electric field in the z-direction is zero.

$$\begin{aligned} \varepsilon\frac{\partial E_x}{\partial x} &= \frac{\partial H_z}{\partial y} - \sigma E_x \\ \varepsilon\frac{\partial E_y}{\partial t} &= \frac{\partial H_z}{\partial x} - \sigma E_y \\ \mu\frac{\partial H_z}{\partial t} &= \frac{\partial E_x}{\partial y} - \frac{\partial E_y}{\partial x} - \sigma_m H_z \end{aligned} \tag{A.1}$$

Equations A.1 can be discretized by applying Yee's scheme:

$$\begin{aligned} E_x^{n+1}(i+\frac{1}{2},j) &= C_{exe}(i+\frac{1}{2},j)E_x^n(i+\frac{1}{2},j) \\ +C_{exh}(i+\frac{1}{2},j)&\frac{H_z^{n+\frac{1}{2}}(i+\frac{1}{2},j+\frac{1}{2}) - H_z^{n+\frac{1}{2}}(i+\frac{1}{2},j-\frac{1}{2})}{\Delta_y} \end{aligned} \tag{A.2}$$

$$E_y^{n+1}(i,j+\frac{1}{2}) = C_{eye}(i,j+\frac{1}{2})E_y^n(i,j+\frac{1}{2}) + C_{eyh}(i,j+\frac{1}{2})\frac{H_z^{n+\frac{1}{2}}(i-\frac{1}{2},j+\frac{1}{2}) - H_z^{n+\frac{1}{2}}(i+\frac{1}{2},j+\frac{1}{2})}{\Delta_x} \tag{A.3}$$

$$H_z^{n+\frac{1}{2}}(i+\frac{1}{2},j+\frac{1}{2}) = C_{hzh}(i+\frac{1}{2},j+\frac{1}{2})H_z^{n-\frac{1}{2}}(i+\frac{1}{2},j+\frac{1}{2}) + C_{hze}(i+\frac{1}{2},j+\frac{1}{2})[\frac{E_y^n(i+\frac{1}{2},j+\frac{1}{2}) - E_y^n(i,j+\frac{1}{2})}{\Delta_x} - \frac{E_x^n(i+\frac{1}{2},j+1) - E_x^n(i+\frac{1}{2},j)}{\Delta_y}] \tag{A.4}$$

where

$$C_{exe}(i+\frac{1}{2},j) = \frac{\frac{\epsilon}{\Delta_t} - \frac{\sigma}{2}}{\frac{\epsilon}{\Delta_t} + \frac{\sigma}{2}} = \frac{1 - \frac{\sigma\Delta_t}{2\epsilon}}{1 + \frac{\sigma\Delta_t}{2\epsilon}}\bigg|_{(i+\frac{1}{2})\Delta_x, j\Delta_y} \tag{A.5}$$

$$C_{exh}(i+\frac{1}{2},j) = \frac{1}{\frac{\epsilon}{\Delta_t} + \frac{\sigma}{2}} = \frac{\frac{\Delta_t}{\epsilon}}{1 + \frac{\sigma\Delta_t}{2\epsilon}}\bigg|_{(i+\frac{1}{2})\Delta_x, j\Delta_y} \tag{A.6}$$

$$C_{eye}(i,j+\frac{1}{2}) = \frac{\frac{\epsilon}{\Delta_t} - \frac{\sigma}{2}}{\frac{\epsilon}{\Delta_t} + \frac{\sigma}{2}} = \frac{1 - \frac{\sigma\Delta_t}{2\epsilon}}{1 + \frac{\sigma\Delta_t}{2\epsilon}}\bigg|_{i\Delta_x, (j+\frac{1}{2})\Delta_y} \tag{A.7}$$

$$C_{eyh}(i,j+\frac{1}{2}) = \frac{1}{\frac{\epsilon}{\Delta_t} + \frac{\sigma}{2}} = \frac{\frac{\Delta_t}{\epsilon}}{1 + \frac{\sigma\Delta_t}{2\epsilon}}\bigg|_{i\Delta_x, (j+\frac{1}{2})\Delta_y} \tag{A.8}$$

$$C_{hzeh}(i+\frac{1}{2},j+\frac{1}{2}) = \frac{\frac{\mu}{\Delta_t} - \frac{\sigma}{2}}{\frac{\epsilon}{\Delta_t} + \frac{\sigma}{2}} = \frac{1 - \frac{\sigma\Delta_t}{2\mu}}{1 + \frac{\sigma\Delta_t}{2\mu}}\bigg|_{(i+\frac{1}{2})\Delta_x, (j+\frac{1}{2})\Delta_y} \tag{A.9}$$

$$C_{hze}(i+\frac{1}{2},j+\frac{1}{2}) = \frac{1}{\frac{\mu}{\Delta_t} + \frac{\sigma}{2}} = \frac{\frac{\Delta_t}{\mu}}{1 + \frac{\sigma\Delta_t}{2\mu}}\bigg|_{(i+\frac{1}{2})\Delta_x, (j+\frac{1}{2})\Delta_y} \tag{A.10}$$

Equivalently for the 2-D transverse magnetic wave, the derivative of the magnetic field in the z-direction is considered as zero. Therefore, the discretized equations in the x- and y- directions can be calculated in a similar way. Following the leapfrog technique, the electric and magnetic fields are calculated at half timesteps. At every computation step the magnetic field components are updated from the electric field components from the previous step and then the electric field components are updated from the magnetic field components [111], [114].

A.2 3-D Finite-Difference Time-Domain Method

This section overviews the derivations for the equations for the 3-D finite difference time domain method, for timestep n and for the points (i, j, k) of the grid. In a similar way with 2-D FDTD, the system of the differential equations is dicretized as follows:

$$\begin{aligned} E_x^{n+1}(i+\frac{1}{2},j,k) &= C_{exe}(i+\frac{1}{2},j,k)E_x^n(i+\frac{1}{2},j,k) \\ +C_{eyh}(i+\frac{1}{2},j,k)[&\frac{H_z^{n+\frac{1}{2}}(i+\frac{1}{2},j+\frac{1}{2},k)-H_z^{n+\frac{1}{2}}(i+\frac{1}{2},j-\frac{1}{2},k)}{\Delta_y} \\ -&\frac{H_y^{n+\frac{1}{2}}(i+\frac{1}{2},j,k+\frac{1}{2})-H_y^{n+\frac{1}{2}}(i+\frac{1}{2},j,k-\frac{1}{2})}{\Delta_z}] \end{aligned} \tag{A.11}$$

$$\begin{aligned} E_y^{n+1}(i,j+\frac{1}{2},k) &= C_{eye}(i,j+\frac{1}{2},k)E_y^n(i,j+\frac{1}{2},k) \\ +C_{eyh}(i,j+\frac{1}{2},k)[&\frac{H_x^{n+\frac{1}{2}}(i,j+\frac{1}{2},k+\frac{1}{2})-H_x^{n+\frac{1}{2}}(i,j+\frac{1}{2},k-\frac{1}{2})}{\Delta_z} \\ -&\frac{H_z^{n+\frac{1}{2}}(i+\frac{1}{2},j+\frac{1}{2},k)-H_z^{n+\frac{1}{2}}(i-\frac{1}{2},j+\frac{1}{2},k)}{\Delta_x}] \end{aligned} \tag{A.12}$$

$$\begin{aligned} E_z^{n+1}(i,j,k+\frac{1}{2}) &= C_{exe}(i,j,k+\frac{1}{2})E_z^n(i,j,k+\frac{1}{2}) \\ +C_{exh}(i,j,k+\frac{1}{2})[&\frac{H_y^{n+\frac{1}{2}}(i+\frac{1}{2},j,k+\frac{1}{2})-H_y^{n+\frac{1}{2}}(i-\frac{1}{2},j,k+\frac{1}{2})}{\Delta_x} \\ -&\frac{H_x^{n+\frac{1}{2}}(i,j+\frac{1}{2},k+\frac{1}{2})-H_x^{n+\frac{1}{2}}(i,j-\frac{1}{2},k+\frac{1}{2})}{\Delta_y}] \end{aligned} \tag{A.13}$$

where

$$C_{exe}(i+\frac{1}{2},j,k)=\left.\frac{1-\frac{\sigma\Delta_t}{2\epsilon}}{1+\frac{\sigma_m\Delta_t}{2\epsilon}}\right|_{(i+\frac{1}{2})\Delta_x,j\Delta_y,k\Delta_z} \tag{A.14}$$

$$C_{eye}(i,j+\frac{1}{2},k)=\left.\frac{1-\frac{\sigma\Delta_t}{2\epsilon}}{1+\frac{\sigma_m\Delta_t}{2\epsilon}}\right|_{i\Delta_x,(j+\frac{1}{2})\Delta_y,k\Delta_z} \tag{A.15}$$

$$C_{eze}(i,j,k+\frac{1}{2})=\left.\frac{1-\frac{\sigma\Delta_t}{2\epsilon}}{1+\frac{\sigma_m\Delta_t}{2\epsilon}}\right|_{i\Delta_x,j\Delta_y,(k+\frac{1}{2})\Delta_z} \tag{A.16}$$

$$C_{exh}(i+\frac{1}{2},j,k)=\left.\frac{\frac{\Delta_t}{\epsilon}}{1+\frac{\sigma\Delta_t}{2\epsilon}}\right|_{(i+\frac{1}{2})\Delta_x,j\Delta_y,\Delta_z} \tag{A.17}$$

$$C_{eyh}(i,j+\frac{1}{2},k)=\left.\frac{\frac{\Delta_t}{\epsilon}}{1+\frac{\sigma\Delta_t}{2\epsilon}}\right|_{i\Delta_x,(j+\frac{1}{2})\Delta_y,\Delta_z} \tag{A.18}$$

$$C_{ezh}(i,j,k+\frac{1}{2})=\left.\frac{\frac{\Delta_t}{\epsilon}}{1+\frac{\sigma\Delta_t}{2\epsilon}}\right|_{i\Delta_x,j\Delta_y,(k+\frac{1}{2})\Delta_z} \tag{A.19}$$

$$\begin{aligned}H_x^{n+\frac{1}{2}}(i,j+\frac{1}{2},k+\frac{1}{2})&=C_{hxh}(i,j+\frac{1}{2},k+\frac{1}{2})H_x^{n-\frac{1}{2}}(i,j+\frac{1}{2},k+\frac{1}{2})\\&-C_{hxe}(i,j+\frac{1}{2},k+\frac{1}{2})[\frac{E_z^n(i,j+1,k+\frac{1}{2})-E_z^n(i,j,k+\frac{1}{2})}{\Delta_y}\\&-\frac{E_y^n(i,j+\frac{1}{2},k+1)-E_y^n(i,j+\frac{1}{2},k)}{\Delta_z}]\end{aligned} \tag{A.20}$$

$$\begin{aligned}H_y^{n+\frac{1}{2}}(i+\frac{1}{2},j,k+\frac{1}{2})&=C_{hyh}(i+\frac{1}{2},j,k+\frac{1}{2})H_y^{n-\frac{1}{2}}(i+\frac{1}{2},j,k+\frac{1}{2})\\&-C_{hye}(i+\frac{1}{2},j,k+\frac{1}{2})[\frac{E_x^n(i+\frac{1}{2},j,k+\frac{1}{2})-E_x^n(i+\frac{1}{2},j,k)}{\Delta_z}\\&-\frac{E_z^n(i+1,j,k+\frac{1}{2})-E_z^n(i,j,k+\frac{1}{2})}{\Delta_x}]\end{aligned} \tag{A.21}$$

$$H_z^{n+\frac{1}{2}}(i+\frac{1}{2},j+\frac{1}{2},k) = C_{hzh}(i+\frac{1}{2},j+\frac{1}{2},k)H_z^{n-\frac{1}{2}}(i+\frac{1}{2},j+\frac{1}{2},k) - C_{hze}(i+\frac{1}{2},j+\frac{1}{2},k)[\frac{E_y^n(i+1,j+\frac{1}{2},k)-E_y^n(i,j+\frac{1}{2},k)}{\Delta_x} - \frac{E_x^n(i+\frac{1}{2},j+1,k)-E_x^n(i+\frac{1}{2},j,k)}{\Delta_y}] \tag{A.22}$$

where

$$C_{hxh}(i,j+\frac{1}{2},k+\frac{1}{2}) = \frac{1-\frac{\sigma_m\Delta_t}{2\mu}}{1+\frac{\sigma_m\Delta_t}{2\mu}}\Big|_{i\Delta_x,(j+\frac{1}{2})\Delta_y,(k+\frac{1}{2})\Delta_z} \tag{A.23}$$

$$C_{hyh}(i+\frac{1}{2},j,k+\frac{1}{2}) = \frac{1-\frac{\sigma_m\Delta_t}{2\mu}}{1+\frac{\sigma_m\Delta_t}{2\mu}}\Big|_{(i+\frac{1}{2})\Delta_x,j\Delta_y,(k+\frac{1}{2})\Delta_z} \tag{A.24}$$

$$C_{hzh}(i,j+\frac{1}{2},k+\frac{1}{2}) = \frac{1-\frac{\sigma_m\Delta_t}{2\mu}}{1+\frac{\sigma_m\Delta_t}{2\mu}}\Big|_{(i+\frac{1}{2})\Delta_x,(j+\frac{1}{2})\Delta_y,k\Delta_z} \tag{A.25}$$

$$C_{hxe}(i,j+\frac{1}{2},k+\frac{1}{2}) = \frac{\frac{\Delta_t}{\delta\mu}}{1+\frac{\sigma_m\Delta_t}{2\mu}}\Big|_{i\Delta_x,(j+\frac{1}{2})\Delta_y,(k+\frac{1}{2})\Delta_z} \tag{A.26}$$

$$C_{hye}(i+\frac{1}{2},j,k+\frac{1}{2}) = \frac{\frac{\Delta_t}{\delta\mu}}{1+\frac{\sigma_m\Delta_t}{2\mu}}\Big|_{(i+\frac{1}{2})\Delta_x,j\Delta_y,(k+\frac{1}{2})\Delta_z} \tag{A.27}$$

$$C_{hxe}(i+\frac{1}{2},j+\frac{1}{2},k) = \frac{\frac{\Delta_t}{\delta\mu}}{1+\frac{\sigma_m\Delta_t}{2\mu}}\Big|_{(i+\frac{1}{2})\Delta_x,(j+\frac{1}{2})\Delta_y,k\Delta_z} \tag{A.28}$$

Following the same approach with 2-D FDTD, at every time step the discretized equations of the magnetic field are updated from electric field components from the previous step and then the discretized equations of the electric field are updated from the magnetic field equations [114]. The process is displayed in Fig. A.1.

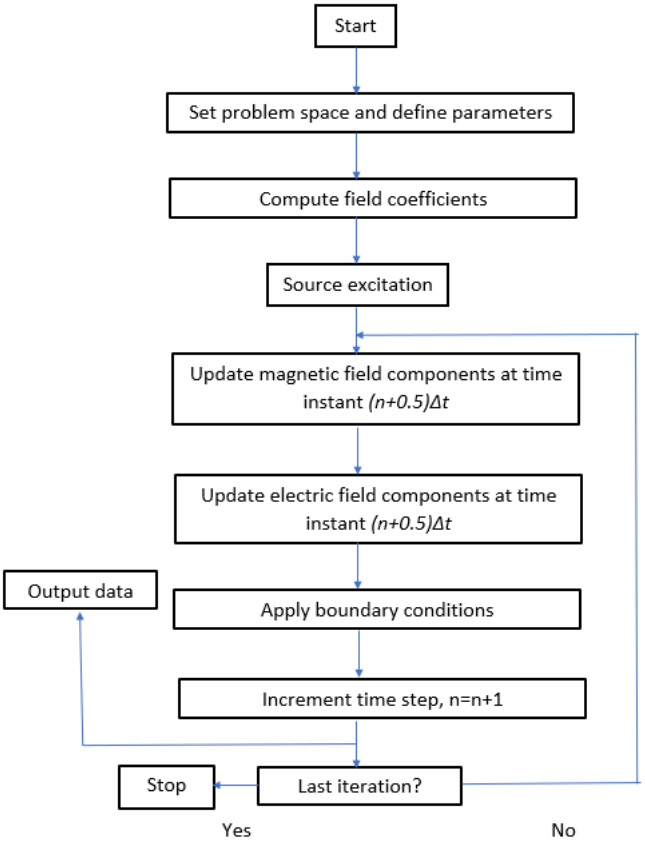

Figure A.1: Schematic of the 3-D FDTD algorithm.

Appendix B

Convolutional Perfectly Matched Layer Formulation

Employing the outcomes of [119], the CPML formulation is performed accordingly:

$$\epsilon_r\epsilon_o\frac{E_{x_{i+\frac{1}{2},j,k}}^{n+1}-E_{x_{i+\frac{1}{2},j,k}}^{n}}{\Delta_t}+\sigma\frac{E_{x_{i+\frac{1}{2},j,k}}^{n+1}+E_{x_{i+\frac{1}{2},j,k}}^{n}}{\Delta_t}= \frac{H_{z_{i+\frac{1}{2},j+\frac{1}{2},k}}^{n+\frac{1}{2}}-H_{z_{i+\frac{1}{2},j-\frac{1}{2},k}}^{n+\frac{1}{2}}}{\kappa_y\Delta_y}-\frac{H_{y_{i+\frac{1}{2},j,k+\frac{1}{2}}}^{n+\frac{1}{2}}-H_{y_{i+\frac{1}{2},j,k-\frac{1}{2}}}^{n+\frac{1}{2}}}{\kappa_z\Delta_z}+ \sum_{m=0}^{N-1}Z_{0y}(m)\frac{H_{z_{i+\frac{1}{2},j+\frac{1}{2},k}}^{n-m+\frac{1}{2}}-H_{z_{i+\frac{1}{2},j-\frac{1}{2},k}}^{n-m+\frac{1}{2}}}{\Delta_y}+\sum_{m=0}^{N-1}Z_{0y}(m)\frac{H_{z_{i+\frac{1}{2},j,k+\frac{1}{2}}}^{n-m+\frac{1}{2}}-H_{z_{i+\frac{1}{2},j,k-\frac{1}{2}}}^{n-m+\frac{1}{2}}}{\Delta_z} \tag{B.1}$$

$Z_{0i}(m)$ can be generated recursively using the recursive convolution method [164], [165]. The set of auxiliary expressions ψ_i is launched, therefore Equation B.1 can be rewritten as:

$$\epsilon_r\epsilon_o\frac{E_{x_{i+\frac{1}{2},j,k}}^{n+1}-E_{x_{i+\frac{1}{2},j,k}}^{n}}{\Delta_t}+\sigma\frac{E_{x_{i+\frac{1}{2},j,k}}^{n+1}+E_{x_{i+\frac{1}{2},j,k}}^{n}}{\Delta_t}= \frac{H_{z_{i+\frac{1}{2},j+\frac{1}{2},k}}^{n+\frac{1}{2}}-H_{z_{i+\frac{1}{2},j-\frac{1}{2},k}}^{n+\frac{1}{2}}}{\kappa_y\Delta_y}-\frac{H_{y_{i+\frac{1}{2},j,k+\frac{1}{2}}}^{n+\frac{1}{2}}-H_{y_{i+\frac{1}{2},j,k-\frac{1}{2}}}^{n+\frac{1}{2}}}{\kappa_z\Delta_z}+ \psi_{e_{xy}}^{n+\frac{1}{2}}{}_{i+\frac{1}{2},j,k}+\psi_{e_{xz}}^{n+\frac{1}{2}}{}_{i+\frac{1}{2},j,k} \tag{B.2}$$

where

$$\psi^{n+\frac{1}{2}}_{e_{xy}{}_{i+\frac{1}{2},j,k}} = b_y \psi^{n-\frac{1}{2}}_{e_{xy}{}_{i+\frac{1}{2},j,k}} + a_y (H_{z\,i+\frac{1}{2},j+\frac{1}{2},k} - H_{z\,i+\frac{1}{2},j-\frac{1}{2},k})/\Delta_y \tag{B.3}$$

$$\psi^{n+\frac{1}{2}}_{e_{xz}{}_{i+\frac{1}{2},j,k}} = b_z \psi^{n-\frac{1}{2}}_{e_{xz}{}_{i+\frac{1}{2},j,k}} + a_z (H_{y\,i+\frac{1}{2},j+\frac{1}{2},k} - H_{y\,i+\frac{1}{2},j-\frac{1}{2},k})/\Delta_z \tag{B.4}$$

$$b_i = e^{-((\sigma_i)/\kappa_i)+a_i)(\Delta_t/\epsilon_0)}, \qquad \text{i = x, y or z} \tag{B.5}$$

and

$$a_i = \frac{\sigma_i}{\sigma_k \kappa_i^2 \alpha_i} (e^{-((\sigma_i)/\kappa_i)+a_i)(\Delta_t/\epsilon_0)} - 1.0) \tag{B.6}$$

Appendix C

Differentiation of Brain Stroke Type by Using Microwave-Based Machine Learning Classification

The third secondment was planned to take place in the University of Lisbon but due to Covid-19 travel restrictions, it was conducted virtually. The initial objective of the secondment was to study the problem of lymph nodes detection and adapt DBIM-TwIST to their in-house experimental prototype for lymph nodes detection. As it was impossible to travel to Portugal and perform any experimental measurements, the objectives of the secondment were altered and focused on the differentiation of brain stroke type by using microwave-based machine learning classification.

To this end, we investigated the potential of classifying the type of the stroke by using microwave-based signals, building upon work of other researchers, such as [37]. To evaluate the potential of this classification, we collected data produced by simulation models of our in-house prototype for brain stroke detection [159], using CST Microwave Studio. Fig. C.1 shows the simulated prototype that is composed by a tank filled with 90% glycerol-water mixture. Within the tank, we placed an ellipsoid brain phantom to which we assigned the dielectric properties of the average brain. The

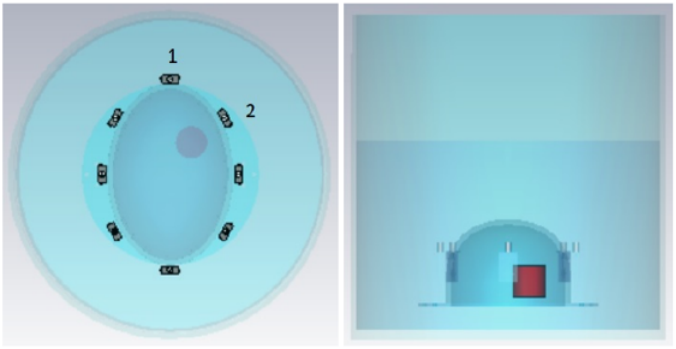

Figure C.1: CST imaging prototype of the tank, the head phantom and the target for h-stroke at location 1.

phantom is surrounded by eight monopole antennas in an elliptical arrangement [148]. Then, we inserted a cylindrical target inside the brain phantom which mimics either the hemorrhagic or the ischemic stroke. The target was located in 3 different positions within the brain, one at the top right, one at the bottom left and one in the center of the brain phantom, respectively. Moreover, we varied the size of the stroke with a diameter ranging from 10 to 40 mm, with a step of 5 mm. Consequently, our database included a total of 42 simulations. For each case, we measured the S-parameters for all antennas, totaling 2688 scattering recordings which were used in our classification endeavors.

We implemented a cascade-classifier, in which we first classified the location of the stroke ahead of its type: ischemic or hemorrhagic. Our rationale was that if we classified strokes that had been identified in the same location, we could better classify their type. We compared two machine learning algorithms by using Matlab Machine Learning toolbox – decision trees and the K-Nearest Neighbors (KNNs) – with a k-fold cross validation methodology.

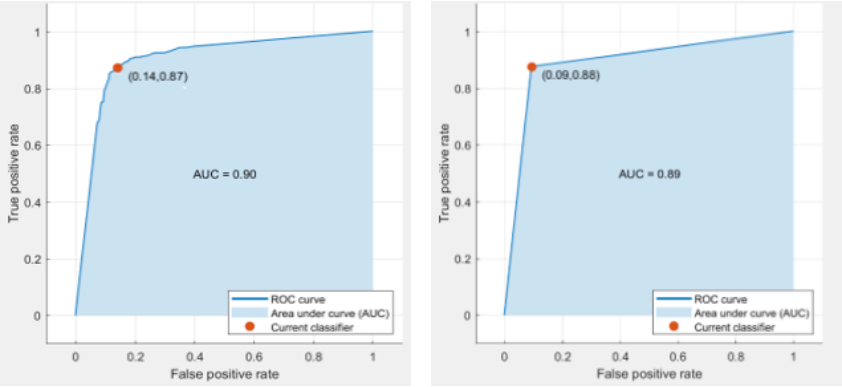

(a) (b)

Figure C.2: True positive rate for stroke type classifier when considering the magnitude of the signals in all locations: Left: Fine Tree classifier; Right: K-Nearest Neighbours classifier.

Fig. C.2 presents the classification accuracy obtained when classifying the accuracy type of stroke, when all locations are considered. Figs. C.3-C.5 show classification accuracies for the three different positions of the stroke. With the proposed cascade-classifier we achieve slightly better classification accuracies for the first and the second position than 89% (KNN) and 90% (Decision Tree), which are the metrics obtained when classifying the accuracy type of stroke, when all locations are considered. However, we note that in all the examined cases the differences were minimum and no significant variations were observed.

Although the achieved results from the cascade-classifier did not significantly vary from the results obtained when all the stroke locations were considered, they are still valid as this initial classification is the first step to build, test and validate a cascade of location-then-type of stroke classifier. The classifier could be further improved by incorporating the information provided by the machine learning algorithms into DBIM-TwIST algorithm and will be further examined in future work.

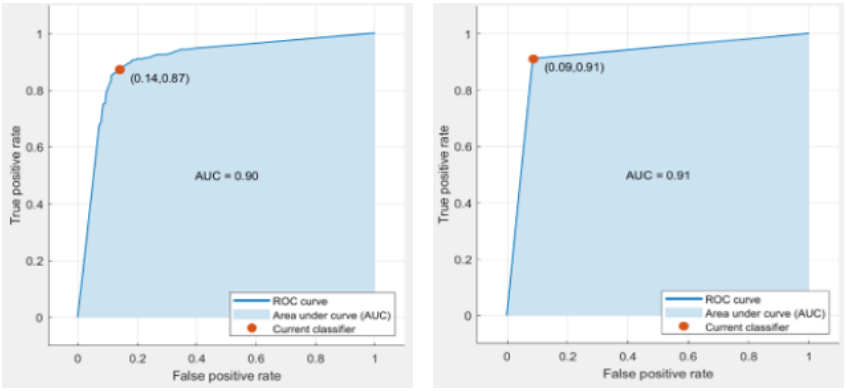

(a) (b)

Figure C.3: True positive rate for stroke type classifier when considering the magnitude of the signals in the top right position: Left: Fine Tree classifier; Right: K-Nearest Neighbours classifier.

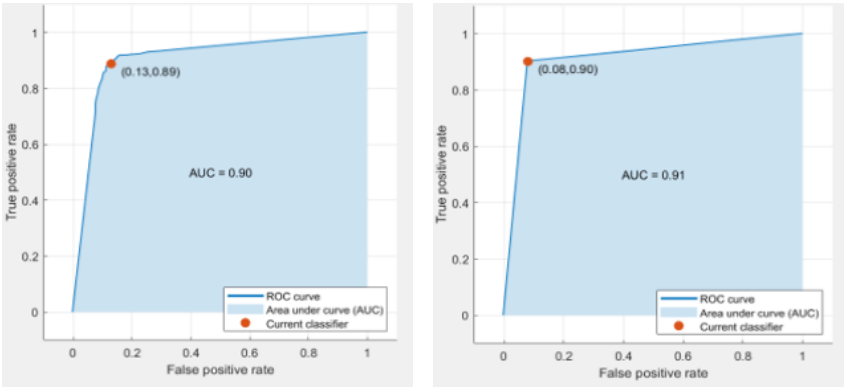

(a) (b)

Figure C.4: True positive rate for stroke type classifier when considering the magnitude of the signals in the bottom left position: Left: Fine Tree classifier; Right: K-Nearest Neighbours classifier.

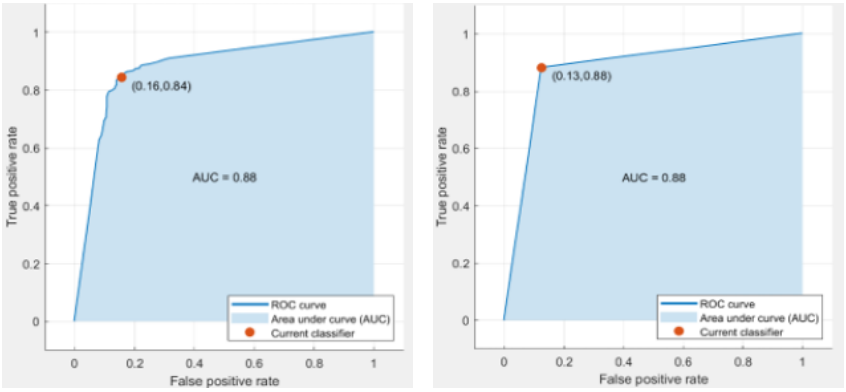

(a) (b)

Figure C.5: True positive rate for stroke type classifier when considering the magnitude of the signals in the middle position: Left: Fine Tree classifier; Right: K-Nearest Neighbours classifier.